TECHNISCHE UNIVERSITÄT MÜNCHEN

TUM School of Natural Sciences

Particle-in-Cell Simulations of Plasma Density Variations in a Proton-Driven Wakefield Accelerator

Pablo Israel Morales Guzman

Vollständiger Abdruck der von der TUM School of Natural Sciences
der Technischen Universität München zur Erlangung des akademischen Grades eines

Doktors der Naturwissenschaften (Dr. rer. nat.)

genehmigten Dissertation.

Vorsitz: Prof. Dr. Laura Fabbietti

Prüfer*innen der Dissertation: 1. Hon.-Prof. Dr. Allen Caldwell

2. Hon.-Prof. Dr. Frank Jenko

Die Dissertation wurde am 05.07.2023 bei der Technischen Universität München
eingereicht und durch die TUM School of Natural Sciences am
19.09.2023 angenommen

Particle-in-Cell Simulations of Plasma Density Variations in a Proton-Driven Wakefield Accelerator

Advanced Wakefield Acceleration Experiment

by

Pablo Israel Morales Guzmán

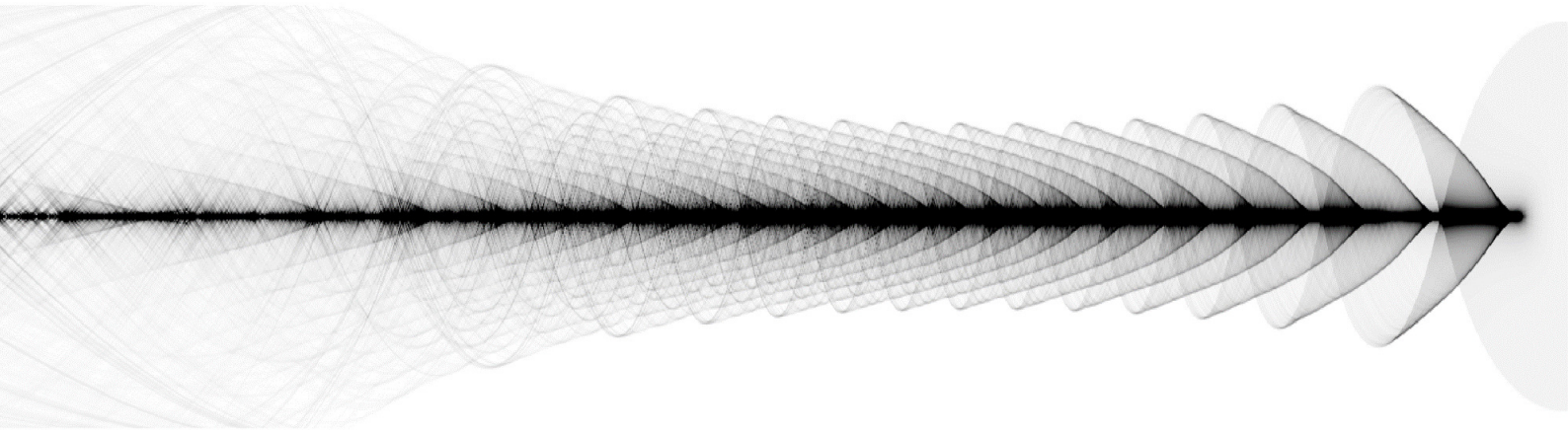

PhD in Physics

at

Technische Universität München

Max-Planck-Institut für Physik

Abstract

Plasma Wakefield Accelerators use relativistic particle bunches to drive high-amplitude (GV/m) wakefields to accelerate other particle bunches. The high energy of relativistic proton bunches much longer than the plasma wavelength can be harnessed to drive high-amplitude wakefields through the scheme of self-modulation. During self-modulation, the long bunch is transformed into a microbunch train, with microbunches spaced approximately by the plasma wavelength, that resonantly drives wakefields.

The most energetic proton bunches are available at CERN, where the Advanced Wakefield Experiment (AWAKE) investigates self-modulation and plasma wakefield acceleration using 400 GeV bunches from the Super Proton Synchrotron. The final goal of AWAKE is to produce wakefields with a 1 GV/m amplitude to accelerate electron bunches, while controlling their emittance and energy spread, to be used for particle physics applications. In order to reach that goal, we must understand and control self-modulation, as well as analyze the processes that could negatively impact the properties of the accelerated electron bunch. The research I do in this thesis is relevant for both topics, self-modulation and acceleration.

I investigate the relation between plasma density and proton bunch density distribution and how they mutually affect each other. I also study various effects of the plasma on an injected electron bunch when propagating within the proton bunch. For my investigation, I use particle-in-cell simulations and make comparisons with experimental results whenever possible. Simulations and experimental results are in good agreement.

In particular, I measure the change in local plasma oscillation frequency, and thus wakefields frequency, when considering the charge distribution of the unmodulated proton bunch, an effect that is not included in linear wakefield theory. Simulations show that the local plasma frequency changes both transversally and longitudinally and is higher where the proton density is also higher, with a difference from the expected plasma frequency on the percent-level for parameters based on those of AWAKE. This initial wakefield frequency sets the initial modulation frequency, which must be considered when studying the modulation frequency evolution along the plasma. The transverse dependence of the frequency also leads to a decrease in the amplitude of the wakefields along the bunch. This is especially relevant when doing experimental measurements at the plasma start, e.g., plasma light and shadowgraphy.

I use linear plasma density gradients to study the slow-down of the phase velocity of the wakefields that is predicted by theory. Positive gradients partially compensate for this slow-down, while negative ones enhance it. I do this by measuring the asymmetry between using positive and negative gradients in the final microbunch train profile, phase evolution of the wakefields, frequency evolution of the wakefields and bunch modulation, amplitude of the wakefields, and energy gain

of accelerated test electrons. A slightly positive gradient leads to the highest energy gain, relevant for the goal of AWAKE.

To study the effect of a self-modulating bunch front on a self-modulated bunch rear, which might occur in the future configuration of AWAKE, I create two seeds at different positions. Besides the usual cut in the density profile of the proton bunch, I place a seed electron bunch inside of the proton bunch. I show that, considering a fixed position for the density cut, an electron bunch with low charge does not seed the modulation, while a bunch with high charge does. At the transition between following the density cut or the electron bunch as seed, the modulation in the rear has a faster growth and reaches saturation earlier. Therefore, when the wakefields from the front are out of phase with the wakefields from the rear, the microbunches from the rear are expelled from the wakefields.

The previous setup with two seeds cannot be currently measured experimentally because there is a plasma density ramp leading to the long plasma. I investigate this plasma ramp in a study that involves both the interaction between bunch and plasma and negative effects on injected electron bunches. One meter before the plasma entrance, the plasma density in the ramp is five orders of magnitude lower than in the long plasma and three orders of magnitude lower than that of the bunch. The non-linear response of the plasma to the proton bunch (both modulated and unmodulated) is to create a high-density electron filament on the bunch propagation axis. I show that the fields sustained by the filament are detrimental for the acceleration of an electron or positron bunch injected on axis through the ramp. I further show that seeding from within the proton bunch is not possible since the seed electron bunch is expelled from the wakefields before reaching the plasma entrance. Therefore, proton-driven plasma wakefield accelerators should avoid a plasma ramp at the plasma entrance. AWAKE avoids the ramp in the accelerator plasma by creating the plasma with a counter-propagating laser pulse that meets the electron bunch at the plasma entrance.

Contents

List of Figures

It's dangerous to go alone! Read this. ⚔

I Introduction

"A writer is a person for whom writing is more difficult than it is for other people" - Thomas Mann

"Hey, you, you're finally **awake**" - Ralof

Figure 1.1: Bird view of the LHC in the CERN accelerator complex at the French-Swiss border close to Geneva. The Geneva Lake and the Alps are in the background. Image from [1].

Since ancient times, humanity has been curious to understand the world in which it lives [2]. A fundamental piece to achieve that goal is to know what the building blocks of the matter around us are. As we as humanity broke objects into smaller and smaller pieces, we surpassed the limit of our own senses. We relied, then, on technology, such as microscopes, to overcome this limitation. As we explore even smaller sizes, light waves are not small enough to resolve those building blocks. The appropriate technology to continue this task is high-energy particle colliders. In them, particle bunches crash into each other at almost the speed of light and, by studying the aftermath, the basic constituents of matter are inferred. As will be explained in the next sections, particle

colliders built with current technology have reached very large sizes and their construction is very expensive [3]. The current largest accelerator, the Large Hadron Collider (LHC) [1] at the Conseil Européen pour la Recherche Nucléaire (CERN) [4] based in Geneva, Switzerland, has a circumference of 27 km [5].

Particle accelerators are not only useful to study the composition of matter. The synchrotron radiation emitted when particles are following a path in circular accelerators creates X-rays [6]. Free-electron lasers [7] using accelerated electron bunches also enable the exploration of matter at the molecular level with high brilliance and high temporal (zeptosecond [8]) resolution. Furthermore, accelerated protons are used in the medical field to treat cancer with radiation therapy [9].

The introduction of plasma-based accelerators as a new technology to accelerate particles significantly reduces the size and cost of these devices. A plasma can sustain very large electric fields that are used to accelerate particles and, thus, the same energy can be reached in a shorter distance. Plasma is used as a medium to transfer the energy of a driver, which can be either a laser pulse or a relativistic particle bunch, to an accelerated bunch. The fields driven are called **wakefields**, and this process is called plasma wakefield acceleration.

I study in this thesis the physics behind a proton-driven plasma wakefield accelerator (PWFA) [10] relying on self-modulation (SM) [11] to accelerate electron bunches. Currently, the only experiment in the world using this concept is the Advanced Wakefield Experiment (AWAKE) [12], located at CERN. The plasma density is a crucial parameter that determines the behavior of the system in a PWFA. I study the effect that different variations of the plasma density have on SM and electron bunch acceleration. My main approach to understand the physics behind it is to use numerical simulations to get an approximation of the phenomena occurring in the real world. A widely-used method to simulate the interaction among the different components of a PWFA is particle-in-cell (PIC) simulations, in which the plasma and bunch particles are represented by ensembles called macroparticles, and they interact through the electric and magnetic fields on a grid.

In this chapter, I introduce in more detail the journey to measure and understand the smallest parts of the universe, the advantages brought by using plasma for this task, and the physics that comes with it. I also give a short introduction to AWAKE and a short introduction to PIC codes. In chapter 2, I show how the frequency and amplitude of the initial (or seed) wakefields are affected by the density of the proton bunch, an effect that is not considered in linear theory. In chapter 3, I delve into the physics of SM by studying the effect of adding a plasma density gradient on the amplitude and phase of the wakefields, and on the frequency of the wakefields and of the modulated proton bunch. The experimental and simulation results show very good agreement, and confirm the theoretical prediction that, during SM growth, the phase velocity of the wakefields is slower than that of the proton bunch [13, 14]. In chapter 4, I study the self-modulation

developing from two seeds, the relativistic ionization front and an electron bunch. This is especially relevant for the future configuration of AWAKE, where it is possible that an unmodulated bunch front propagates in plasma and modulates in front of the microbunch train, partially destroying the microbunches. Then I show in chapter 5 why the effects reported in chapter 4 cannot be measured experimentally with the current setup, which includes a plasma ramp at the plasma entrance. I explore with simulations the non-linear response of the low-density plasma ramp to the proton bunch in the region leading to the plasma entrance. This non-linear response has negative effects on an injected electron bunch, i.e., charge loss and emittance increase.

1.1 Particle accelerators to understand the universe

1.1.1 The search for the smallest structures

The ancient Greeks have been attributed with the start of the quest to know what the smallest unit of matter is, from which everything is built. Around 430 B.C., Democritus of Abdera (depicted in Fig. 1.2), disciple of Leucippus of Miletus, coined the term *atomos*, meaning indivisible, to these building blocks [2].

Thousands of years later, in the 19th century, by studying the proportions in which elements combine to form compounds, several scientists contributed to the understanding of atoms. To name a few, the foundation of atomic chemistry was built by Dalton, Gay-Lussac, and Avogadro. Mendeleyev created the periodic table in 1869 [16], although atoms were thought to be homogeneous and their internal structure was not yet known.

In 1897 the cathode ray tube allowed for the discovery of the electron by Thomson [17]. The discovery of the proton is attributed to Rutherford in 1917, when he observed that alpha particles, when reacting with N, combined to form O and a H ion. Since then, further developments, where particle collisions are largely involved, led to the Standard Model of particle physics [18] in 1967. The Standard Model is a very successful description of the composition of the matter in the universe, including three of the four fundamental forces: electromagnetism, the weak force, and the strong force. However, there are still topics to be resolved that require particle collisions with higher energies than the ones available currently, such as how gravity fits with the rest of the forces; the existence of dark matter [19] and dark energy [20], which make up most of the energy in the universe [21]; and the possibility of observing new particles.

1.1.2 Particle acceleration

The reason why higher energies are required to observe smaller structures comes from the fact that the probe has to be smaller than the object being observed. An example of a common probe

Figure 1.2: Artisitic representation of Democritus (left) presumably thinking how to divide matter in smaller pieces. Image from [15].

are electromagnetic waves. With light, which has a wavelength between 400 to 700 nm, we can observe the cellular structure. X-rays, with a wavelength between 0.3 and 3 nm, can be used to observe sub-atomic structures. Relativistic articles also have an associated wavelength λ_{dB} that is inversely proportional to its energy E, according to de Broglie, given by

$$\lambda_{dB} = \frac{h}{p} \approx \frac{hc}{E}, \tag{1.1}$$

where h is the Planck constant, c is the speed of light, and p is the particle momentum. Equation 1.1 shows that the resolution of a particle used as probe increases with its energy. To resolve sub-atomic structures, e.g., the charge radius of a proton (10^{-15} m), particles (with charge equal to the electron charge) need an energy of 10 GeV, i.e., they should have been subject to an electric potential of 10 GV. Particle accelerators provide an electric field for the particles to reach this energy.

The resolution of the atom composition is not the only pursuit of particle colliders. Following Einstein's relation of rest mass m_0 and energy E_0 in the rest frame $E_0 = m_0c^2$ [22] to force the

creation of particles with higher masses than the ones we interact with normally (protons, neutrons, and electrons), we must collide particles with higher energies. The heaviest particle known currently is the top quark with a mass of 173 GeV/c^2 [23]. To overcome this limit, particles with energies in the order of hundreds of GeVs must be provided.

In an electric field, particles are accelerated by the Lorentz Force **F** [24, 25]

$$\mathbf{F} = q(\mathbf{E} + \mathbf{v} \times \mathbf{B}), \tag{1.2}$$

where q is the charge of the particle, **E** is the electric field, **v** is the particle velocity, and **B** is the magnetic field. Since **B** cannot perform work given that $\mathbf{v} \times \mathbf{B}$ is always perpendicular to **v**, the acceleration is due to $E_\parallel$, the longitudinal component of **E**.

The energy gain is the result of the total distance over which the particle is subject to $E_\parallel$

$$\text{Energy} = q \int_{s_{\text{start}}}^{s_{\text{end}}} E_\parallel ds = qU, \tag{1.3}$$

where s_{start} and s_{end} are the start and end of the path, and U is the total electric potential. This means that, to achieve a certain amount of energy there are three options: the particle must propagate in...

- ... an electric field with high amplitude for a short distance,
- ... an electric field with low amplitude for a long distance, or
- ... the same electric field multiple times in a circular manner.

1.1.3 The challenge of current accelerators

There is a fundamental upper limit to the accelerating gradient in accelerators built with current technology, and that is the material breakdown at electric fields of approximately 100 MV/m. The most recently built accelerators are not close to this limit, e.g., European X-FEL at 23.6 MV/m [26].

To avoid building excessively long linear accelerators, a circular device can be used, in which particles propagate through the accelerating cavities several times. There are two limiting factors for the energy gain of an accelerated particle in a circular accelerator. One of them is the value of the magnetic fields to maintain particles in the circular orbit. Higher energies require higher magnetic fields. The other one is the energy lost through synchrotron radiation [27], which scales with γ^4/R, where $\gamma \approx E/m_0c^2$ is the Lorentz factor of the relativistic particle and R is the radius of the accelerator. For this reason, the acceleration of electrons and positrons, which are the lightest charged elementary particles, becomes ineffective for energies above 100 GeV. More massive particles have a lower γ for the same energy. Protons, for example, can be accelerated up to TeV

of energy [28] (which makes them a convenient choice as drivers in a PWFA, as discussed in Subsec. 1.2.4).

To accelerate positrons and electrons we must turn back to linear colliders. Here, the limiting factors are the amplitude of the electric field for acceleration and the length of the accelerator. Since the material already gives an upper limit, the only way of increasing the particle energy using the current technology is to increase the accelerator length. CERN developed a plan to build a new linear electron-positron collider measuring initially 11 km, the Compact Linear Collider (CLIC), to perform precision measurement of the Higgs Boson and top quark [29]. The final stage would extend the accelerator to 50 km and produce electrons and positrons that would have a collision energy of 3 TeV. Japan is a possible host for the construction for the 20 km-long International Linear Collider (ILC), which aims to explore what dark matter and dark energy is, and whether supersymmetry exists [30]. Both projects have not yet initiated construction, primarily due to their large costs.

By changing the current technology upon which particle accelerator rely, higher accelerating gradients are possible. This in turn reduces the distance needed for acceleration and therefore their cost. One possibility is to find ways of increasing the material breakdown limit. Cavities made from copper can sustain an electric field of 250 MV/m [31], whereas a copper-silver alloy can sustain an electric field slightly larger than 300 MV/m [32]. A more radical approach is to completely change the accelerating medium. Plasma, in which the electrons and ions are already separated and, therefore, one could say that the material is already "broken-down", is a viable candidate. Accelerating gradients of 100 GeV/m have already been reported [33].

1.2 Plasma Wakefield Acceleration

In this section, I introduce the basic principles governing plasmas, how they are used to accelerate charged particles bunches, and the physics following the linear approximation of a particle bunch propagating in plasma. Thereupon, I introduce the principle of self-modulation [34] that allows a long proton bunch to drive high-amplitude wakefields, and the density step, a mechanism that leads to maintaining a high amplitude of the wakefields after the saturation of SM. Finally, I mention details about the injection of charged particle bunches for acceleration.

1.2.1 Plasma basics

Plasma can be considered as the fourth state of matter. By increasing the temperature in the system where there is a solid object, it eventually transforms into a liquid. A further increase in temperature turns it into a gas. Finally, increasing the temperature even more will overcome the binding energy of the electrons to the ions, and the object will be a plasma, in which the electrons and ions

move freely. The electrons are thousands of times lighter than the ions, so it is normally assumed that the movement of ions is not significant over time scales of interest and they remain stationary. The temperature of the plasma is low enough that thermal fluctuations do not inhibit the charge shielding by plasma electrons. This is called the cold plasma approximation. Both assumptions apply to the plasmas treated in this work.

There are three properties that a collection of free electrons and ions should have to be considered an ideal plasma [35]:

1. The number of electrons inside a sphere with radius equal to the Debye length [36] should be much larger than 1. The Deby length is defined as

$$\lambda_D = \sqrt{\frac{\varepsilon_0 k_B T_e}{n_{pe} e^2}}, \tag{1.4}$$

   where ε_0 is the permittivity of free space, k_B is the Boltzmann constant, T_e is the temperature of the electrons, n_{pe} is the plasma density, and e is the charge of the electron.

2. To allow for a collective response, λ_D is much smaller than the size of the plasma.

3. The plasma oscillation angular frequency

$$\omega_{pe} = \sqrt{\frac{n_{pe} e^2}{m_e \varepsilon_0}}, \tag{1.5}$$

   where m_e is the electron mass, is higher than the electron-neutral collision frequency, so that the plasma can be considered collisionless.

The plasma angular frequency ω_{pe}, mentioned in the last point, was first described by Langmuir and Tonks [37]. One way to calculate it, is to consider a one-dimensional case in which a slab of charge is displaced by an infinitesimal amount δx from its neutral position. The charge density left without neutralization is $\sigma = e\, n_{pe}\, \delta x$. Following Gauss' Law[1], the electric field E sustained by this charge is $E = -\sigma / \varepsilon_0 = -e\, n_{pe}\, \delta x / \varepsilon_0$, pointing to the normal vector of the slab surface, where σ is the charge density in the slab. Following Newton's Law, the restoring force for the electron layer is

$$m_e \frac{d^2 \delta x}{dt^2} = -eE = \frac{e^2 n_{pe} \delta x}{\varepsilon_0}, \tag{1.6}$$

[1] Gauss' Law indicates that the electric flux Ω_E going through a closed surface is equal to the charge Q enclosed by the surface normalized by ε_0, $\Omega_E = \oiint_S \mathbf{E} \cdot d\mathbf{A} = Q/\varepsilon_0$.

where t is time. It can be rewritten as

$$\frac{d^2\delta x}{dt^2} + \omega_{pe}^2 \delta x = 0. \tag{1.7}$$

Solving the differential equation will give a sinusoidal function with angular frequency ω_{pe} as defined in Eq. 1.5.

1.2.2 Acceleration with plasma

The first groups to suggest the use of the fields sustained in a plasma to accelerate particles were the ones led by Veksler [38] and Budker [39] in 1956. Years later, the first plasma-based accelerator was proposed by Tajima and Dawson, described in the highly-cited publication [40] in 1979. There, the ponderomotive force of a laser pulse is used to the separate the electrons from the ions and the $E_\parallel$ reached amplitudes of 100 GV/m. It was until 1982 when the first experimental results regarding plasma-based accelerators were published by Joshi et al. [41].

An estimate of the field amplitude attainable in a plasma is given by the wave-breaking limit $E_{WB} = m_e c\omega_{pe}/e \approx 100[\mathrm{V/m}]\sqrt{n_{pe}}$. For typical n_{pe} values used in experiments, 10^{14} to $10^{18}\,\mathrm{cm}^{-3}$, the $E_\parallel$ = 1 to 100 GV/m, which are much higher than the $E_\parallel$ used today in conventional accelerators, $E_\parallel$ < 100 MV/m.

Besides laser pulses, relativistic charged particle bunches can also excite a plasma response. This was suggested by Chen et al. [42] in 1985, and experimentally confirmed in 1988 by Rosenzweig et al. [43]. The fields sustained by the plasma excitation due to a particle bunch or laser pulse are called **wakefields**. When a laser pulse is used, the device is called a laser wakefield accelerator (LWFA), and when a bunch is used, the device is called a plasma wakefield accelerator (PWFA). This thesis is concerned only with the latter.

1.2.3 Linear wakefield theory

When the plasma electrons have a small displacement compared to λ_D due to the relativistic charged particle bunch propagating in it, the perturbation in the plasma density is small compared to the plasma density itself $\delta n << n_{pe}$. In this case, the plasma response and the wakefields driven can be calculated using the linear approximation. It is convenient to separate the particle bunch density distribution n_b in its longitudinal and transverse components, such as

$$n_b(\xi, r) = n_{b0} n_\parallel(\xi) n_\perp(r), \tag{1.8}$$

where n_{b0} is the maximum bunch density, $n_\parallel$ and $n_\perp$ are the longitudinal and transverse components of n_b, respectively, which are normalized to 1, ξ is the coordinate along the bunch, and r

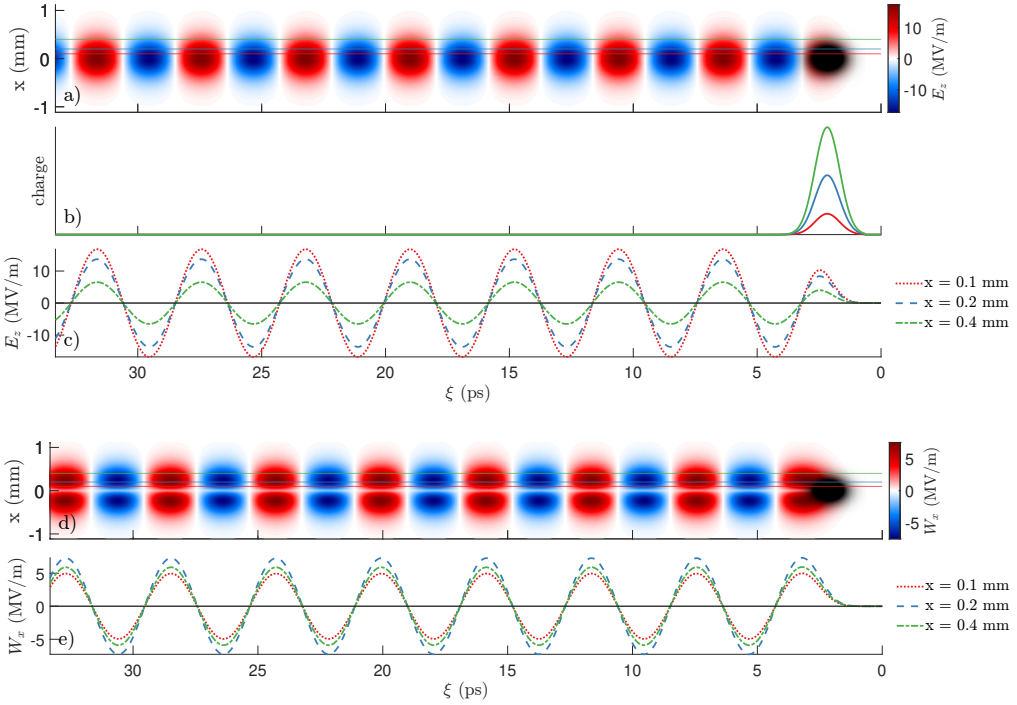

Figure 1.3: Numerical integration of Eqs. 1.9 and 1.11 for (a)(c) longitudinal wakefields and 1.10 and 1.11 for (d)(e) transverse wakefields (negative fields attract positively charged particles to the axis). (a)(d) Wakefields together with the density of a short electron bunch, propagating to the right, mirrored about the axis (2D axisymmetric geometry). (c)(e) Lineout of the wakefields at various transverse distances. (b) Lineouts of the bunch charge, by integrating the density within the transverse limits indicated in the legend, with continuous lines with the same color as the lineout of the wakefields.

is the coordinate across the bunch. The small displacements and, thus, the small density perturbations, occur when $n_{b0} << n_{pe}$. Following [44], the longitudinal field is described by

$$W_z(\xi,r) = -\frac{n_{b0}e}{\varepsilon_0}\int_{-\infty}^{\xi} n_{\parallel}(\xi')\cos(k_{pe}(\xi-\xi'))d\xi' R(r) \tag{1.9}$$

and the transverse field is described by

$$W_r(\xi,r) = -\frac{n_{b0}e}{\varepsilon_0 k_{pe}}\int_{-\infty}^{\xi} n_{\parallel}(\xi')\sin(k_{pe}(\xi-\xi'))d\xi' \frac{dR(r)}{dr} \tag{1.10}$$

where $k_{pe} = \omega_{pe}/c$ is the plasma wave number, and $R(r)$ which appears in both equations is

$$R(r) = k_{pe}^2 K_0(k_{pe}r)\int_0^r r' n_{\perp}(r') I_0(k_{pe}r')dr' + k_{pe}^2 I_0(k_{pe}r)\int_r^{\infty} r' n_{\perp}(r') K_0(k_{pe}r)dr' \tag{1.11}$$

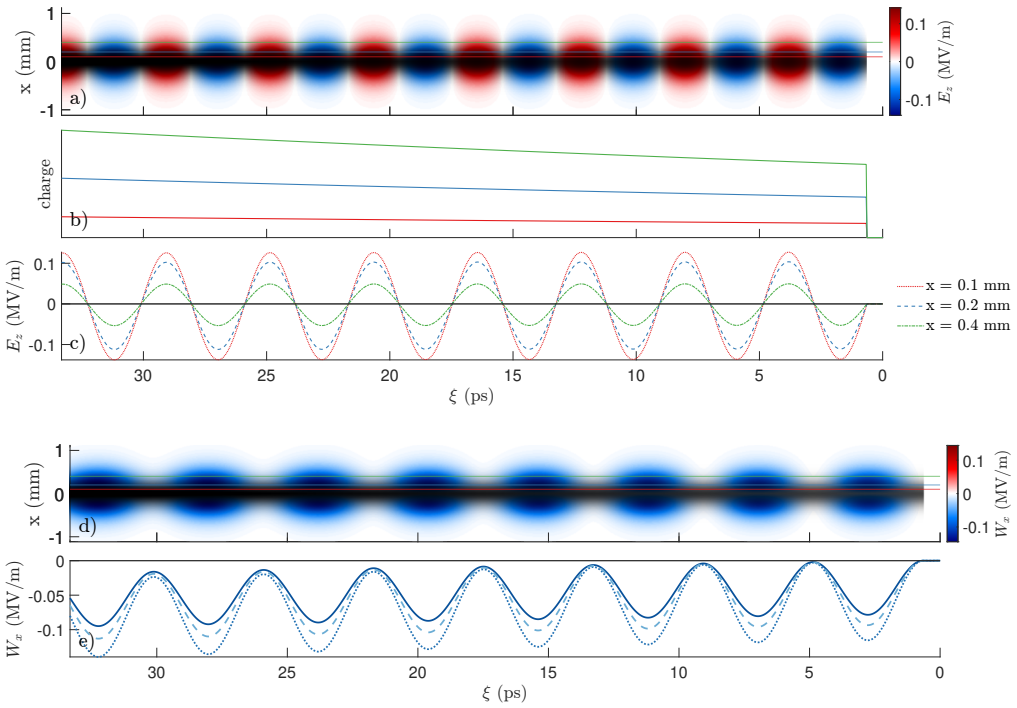

Figure 1.4: Numerical integration of Eqs. 1.9 and 1.11 for a (a)-(c) longitudinal wakefields and 1.10 and 1.11 for (d)(e) transverse wakefields (negative fields attract positively charged particles to the axis). (a)(d) Wakefields together with the density of a long proton bunch, propagating to the right, mirrored about the axis (2D axisymmetric geometry). (c)(e) Lineout of the wakefields at various transverse distances. (b) Lineouts of the bunch charge, by integrating the density within the transverse limits indicated in the legend, with continuous lines with the same color as the lineout of the wakefields.

where I_0 and K_0 are the zeroth order modified Bessel functions of the first and second kind, respectively. It must be noted that these equations do not consider the charge neutralization of the drive bunch by the plasma electrons. This effect becomes relevant in the case of a proton bunch much longer than the plasma wavelength $\lambda_{pe} = 2\pi c/\omega_{pe}$, where the effective plasma density increases locally. An increase in n_{pe} leads to an increase in ω_{pe}, as discussed in chapter 2.

The proton bunches treated in this thesis satisfy $n_{b0} << n_{pe}$. Usually, n_{b0} is in the range of 0.5 to 4 % of $n_{pe} = 1$ to $7\times10^{14}\,\mathrm{cm}^{-3}$, so the equations obtained by applying the linear approximation are valid for the initial wakefields driven in plasma (except for charge neutralization).

Figure 1.3 shows the longitudinal and transverse wakefields calculated by numerically integrating Eqs. 1.9, 1.10, and 1.11 considering a short electron bunch with a Gaussian longitudinal and transverse profiles, propagating in plasma with $n_{pe} = 7\times10^{14}\,\mathrm{cm}^{-3}$. The root mean square (rms) length is $\sigma_z = 0.15\,\mathrm{mm} < \lambda_{pe}$ and the rms width $\sigma_r = c/\omega_{pe}$. When the wakefields are measured

at some position z in the plasma behind the electron bunch, their amplitude oscillates with the frequency given by $\omega_{pe}/2\pi$.

Figure 1.4 shows the longitudinal and transverse wakefields in a segment of a long proton bunch, similar to the one used in AWAKE. It has a Gaussian longitudinal and transverse profile, with sizes $\sigma_z = 7.5\,\text{cm} >> \lambda_{pe}$ and $\sigma_r = c/\omega_{pe}$, and a cut in the bunch density distribution placed at $3\,\sigma_z$ ahead of the bunch center. The adiabatic response of the plasma to the bunch is to neutralize the bunch charge and can be seen with the transverse wakefields being focusing for protons, i.e., negative, all along this segment of the bunch. The amplitude of the wakefields also depends on the position along the bunch of the cut in its density profile, as it is proportional to the proton bunch density value at the position of the cut. As explained in the next section 1.2.4, these wakefields start an instability that allows their amplitude to grow.

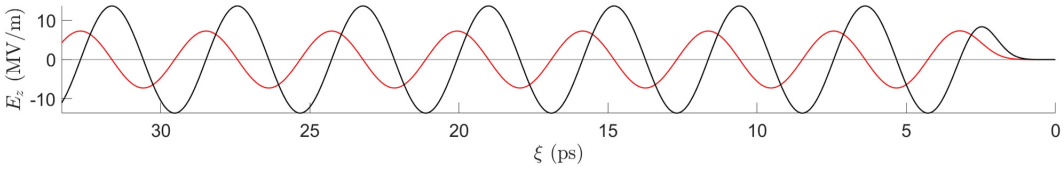

Figure 1.5: Lineout of the longitudinal wakefields (black) at $r = 0\,\text{mm}$ and transverse wakefields (red) at $r = 0.2\,\text{mm}$ from Fig. 1.3. They are shifted in phase by $\pi/2$.

As seen in Figs. 1.3(a)(c), the longitudinal wakefields alternate from accelerating to decelerating and in Figs. 1.3(d)(e) transverse wakefields from focusing to defocusing. Charged particles placed in the accelerating region of the wakefields extract energy from them and charged particles placed in the decelerating region of the wakefields give energy to them. Wakefields with more energy U_E have a larger amplitude following the relation $U_E \propto |\mathbf{E}|^2$. Charged particles placed in the focusing region of the wakefields are attracted to the axis, while charged particles placed in the defocusing region of the wakefields are repelled from the axis. The phase difference between longitudinal and transverse wakefields, according to linear theory, is $\pi/2$, as seen in Fig. 1.5. To drive wakefields effectively, particle bunches should be placed in the focusing and decelerating region of the wakefields. To be accelerated effectively, particle bunches should be placed in the focusing and accelerating region of the wakefields.

1.2.4 Plasma response to a long proton bunch

Considering a linear plasma response, drive bunches shorter than $\lambda_{pe}/2$ are subject only to decelerating wakefields and give energy to the plasma. When the bunch is longer than $\lambda_{pe}/2$, some part of it will be in the accelerating region of the wakefields, extracting energy from them and therefore decreasing their amplitude. This phenomenon is depicted in Fig. 1.6, which was produced with particle-in-cell simulations (see Sec. 1.4) and displays the wakefields driven either by a short or a

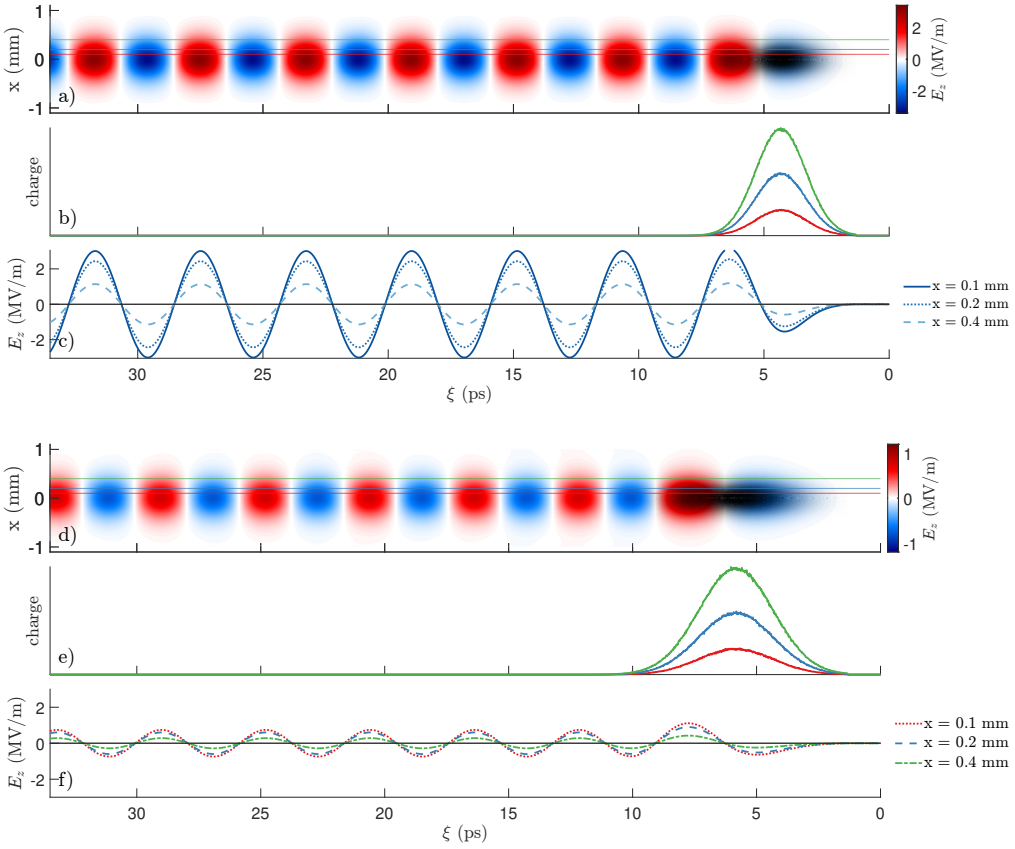

Figure 1.6: From numerical simulations, longitudinal wakefields together with the density of a (a) short and (d) long proton bunch propagating to the right and mirrored about the axis (2D axisymmetric geometry). Both bunches have the same charge. Charge profile of the (a) short and (d) long bunch integrated in the transverse regions indicated in the legend. (c) and (f) Lineout of the wakefields driven by the (a) short and (d) long proton bunch at the transverse positions indicated in the legend. The amplitude of the wakefields is smaller for the longer bunch.

long bunch, both with the same charge. The wakefields driven by the long bunch have a lower amplitude and are less effective in accelerating electron bunches, therefore, drive bunches should ideally be shorter than $\lambda_{pe}/2$.

Nevertheless, short electron bunches available have energies of ≈ 100 J [45]. This means that the use of a short drive bunch to accelerate particles bunches to TeV of energy per particle and kJ of energy per bunch would require staging of several plasmas [45]. Proton bunches, on the other hand, which are accelerated in synchrotrons, can reach much higher energies. The proton bunch accelerated in the Super Proton Synchrotron (SPS) in CERN, has an energy of 400 GeV per proton, amounting to 19 kJ per bunch (3×10^{11} protons/bunch). The LHC produces protons with an energy of 6.5 TeV, which translates to 104 kJ per bunch (1×10^{11} protons/bunch). The

longitudinal and transverse profiles of these bunches can be approximated by a Gaussian with a σ_z = 6 to 12 cm and, in AWAKE, focused to a $\sigma_r \approx 200\,\mu$m.

The condition to avoid filamentation [46] of the proton bunch is $\sigma_r < c/\omega_{pe}$. Given that σ_r = 200 μm, the largest n_{pe} that leads to the ω_{pe} that satisfies $\sigma_r < c/\omega_{pe}$ is $7{\times}10^{14}$ cm^{-3}. Therefore, λ_{pe} = 1.26 mm<< σ_z. The wakefields in such a situation are not driven effectively and have a much lower amplitude compared to a proton bunch with the same charge and with $\sigma_z = \lambda_{pe}/2$. Nevertheless, an instability in the plasma can be exploited to increase the amplitude of the wakefields: the self-modulation instability (SMI) [34].

The wakefields driven by the long bunch exist all along and within the bunch, as seen in Fig. 1.4. The bunch is subject to transverse and longitudinal wakefields with a periodically changing amplitude. The protons do not change their longitudinal positions along the bunch since they are relativistic, but can be moved away from or towards the axis. The transverse wakefields are either all focusing, with regions of higher and lower amplitudes, or alternate between focusing and defocusing. In either configuration of the transverse fields, the proton bunch density will start radially modulating as some protons move towards the propagation axis faster than others, and some may even move away from it, as seen in the diagram in Fig. 1.7. This modulation, with a periodicity of approximately λ_{pe}, enhances the plasma electron oscillations, increasing their oscillation amplitude and therefore the amplitude of the wakefields. Given a long enough plasma, the modulation saturates and the long proton bunch is transformed into a microbunch train, where the microbunches have a spacing of approximately λ_{pe} and resonantly drive wakefields (Fig. 1.8).

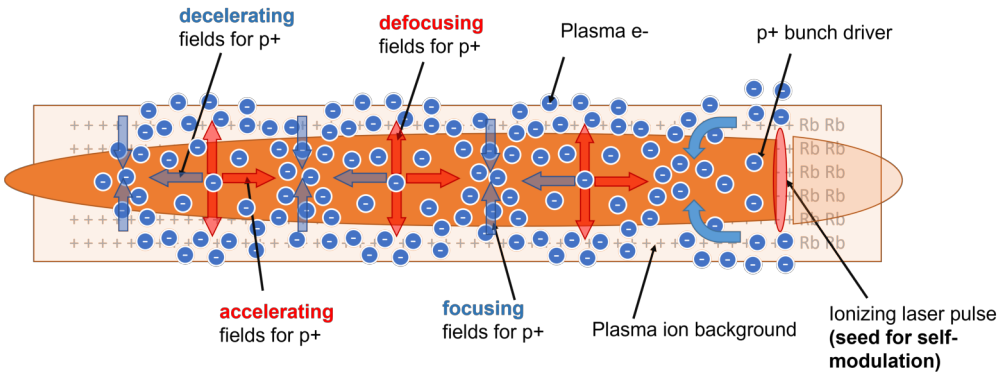

Figure 1.7: Diagram of the relativistic long proton bunch propagating to the right in the plasma together with the laser pulse that creates the RIF (see Sec. 1.3.1). Accelerating, decelerating, focusing, and defocusing wakefields appear periodically within the proton bunch.

As the microbunch train propagates in plasma, the first microbunch attracts the plasma electrons to the axis, creating there a higher concentration of plasma electrons. Their space charge eventually repels them, creating a partial depletion of plasma electrons where there is no mi-

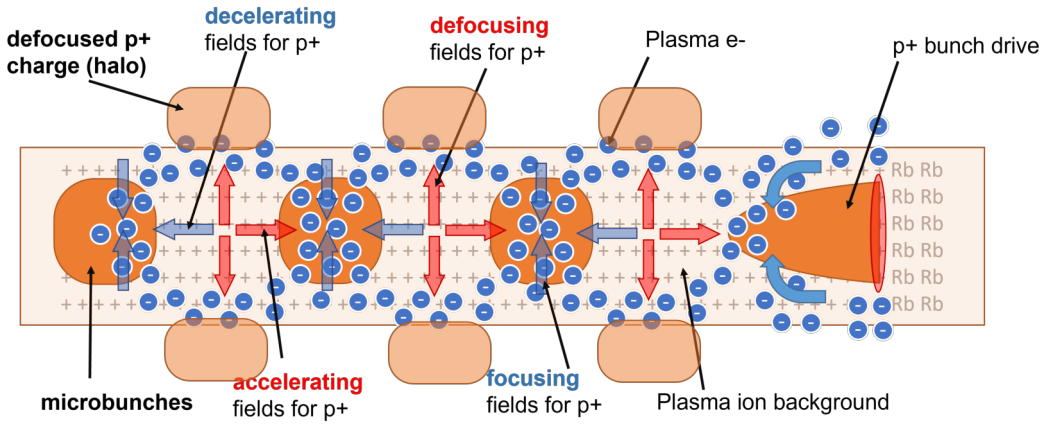

Figure 1.8: Diagram of a microbunch train propagating to the right, result of the transverse modulation of the proton bunch after propagation in plasma. The microbunches are spaced by approximately the periodicity of the wakefields.

crobunch. As a reminder, the movement of heavy ions[2] can be neglected on the time scales of SM. The ion background together with the next microbunch attracts the plasma electrons back to axis, increasing their transverse momentum. This causes an even higher concentration of plasma electrons on axis, which makes them bounce back with more momentum. This leads to a higher oscillation amplitude than after the first microbunch, which means a larger depletion of plasma electrons. This process repeats after each microbunch, increasing the transverse momentum and the concentration and depletion of plasma electrons, which sustain higher wakefield amplitudes.

The amplitude of the transverse wakefields is given by

$$W_\perp(n_{b0}, z, \xi) = W_{\perp 0}(n_{b0}) e^{\Gamma(n_{b0}, z, \xi) z}, \tag{1.12}$$

where $W_{\perp 0}$ is the initial amplitude of the wakefields and the growth rate $\Gamma(n_{b0}, z, \xi)$ is [13]

$$\Gamma(n_{b0}, z, \xi) = \frac{3\sqrt{3}}{4} \omega_{pe} \left(\frac{n_{b0} m_e \xi}{2 n_{pe}} m_p \gamma_p z \right), \tag{1.13}$$

where m_p and γ_p are the mass and relativistic factor of the protons, respectively.

Figure 1.9(d), produced using LCODE [47] (see Sec. 1.4) with the parameters in Table 5.3, shows how the amplitude of the wakefields increases from the front to the back of the microbunch train. The amplitude saturates when the microbunch train ends or when the phase of the plasma electron oscillations is such that a larger fraction of each microbunch is subject to decelerating wakefields. This can occur, e.g., when the plasma electrons become relativistic as their transverse

[2] In the case of AWAKE, the heavy ions are those of Rb.

velocity increases[3]. Furthermore, as the amplitude of the wakefields increases, its behavior deviates from the description given by linear theory (Eqs. 1.9, 1.10, and 1.11). This is one reason to use PIC codes (see Sec. 1.4) to simulate and study the evolution of the system.

Another source of position shift between the wakefields and microbunches is the decrease in the phase velocity of the wakefields v_{ph} during SM growth. It was derived in [13] for a bunch of constant density and it grows along the bunch and along the plasma as

$$v_{ph} = v_b\left(1 - \frac{1}{2}\left(\frac{\xi}{z}\right)^{1/3}\left(\frac{n_{b0}m_e}{2n_e m_p \gamma}\right)^{1/3}\right), \tag{1.14}$$

where $v_b \approx c$ is the velocity of the bunch. This is valid only during self-modulation growth. After saturation, $v_{ph} \approx v_b$, although it will be slightly different when the microbunch train is still evolving. The AWAKE Collaboration explored experimentally the validity of Eq. 1.14 by observing the effect of applying a density gradient to the long plasma [48]. The effect of the density gradient is to increase or decrease ω_{pe} along the plasma, given that $\omega_{pe}(z) \propto \sqrt{n_{pe}(z)}$. The plasma electron oscillations, and thus the wakefields, start at the same seeding position along the bunch. Furthermore, the relative phase of the wakefields $\phi = \omega_{pe}\xi/c$, so a point with a fixed phase moves closer to or away from the seeding position, with positive or negative gradients, respectively. Therefore, an increase or decrease in ω_{pe} is also an increase or decrease of v_{ph}. I explore, with PIC simulations (see Sec. 1.4), the intricate dependency among the phase, amplitude, frequency of the wakefields, periodicity, and charge of the microbunch train in [49], and revisit it in chapter 3. The effect of the gradient on the focused and defocused parts of the first microbunches has been discussed in [50].

The density profile of the proton bunch in the experiment has random features, labelled as noise, from which the SMI grows. The phase of the initial wakefields is then tied to these random features. For injection and acceleration of electron bunches, the phase of the wakefields must be known beforehand. In order to predict the phase of the wakefields consistently event after event, the SM must be seeded. In AWAKE, there are two seeding mechanisms available. One of them is referred as relativistic ionization front (RIF) seeding [51], in which a laser pulse that ionizes gas to transform it into plasma is placed within the proton bunch, so that there is a sharp onset of the plasma inside of the proton bunch from which the SM grows. This is replaced in simulations by using a proton bunch with a cut in the density profile at the same position as that of the RIF [52]. The other mechanism is placing a short electron bunch ahead of the proton bunch [50, 53]. The wakefields driven by the electron bunch kickstart the modulation of the proton bunch, setting its phase.

[3] The transverse displacement of the plasma electrons increases, but the time in which they return to axis remains approximately the same.

1.2.5 Saturation of self-modulation and density step

In a constant-density plasma, due to the dephasing of the wakefields and, consequently, microbunches being in the defocusing phase of the wakefields, the microbunch train starts losing charge after saturation. The microbunches in the rear of the microbunch train are more affected than the ones in the front and the microbunch train becomes shorter. The shortening of the train and the general charge loss lead to a decrease in the amplitude of the wakefields.

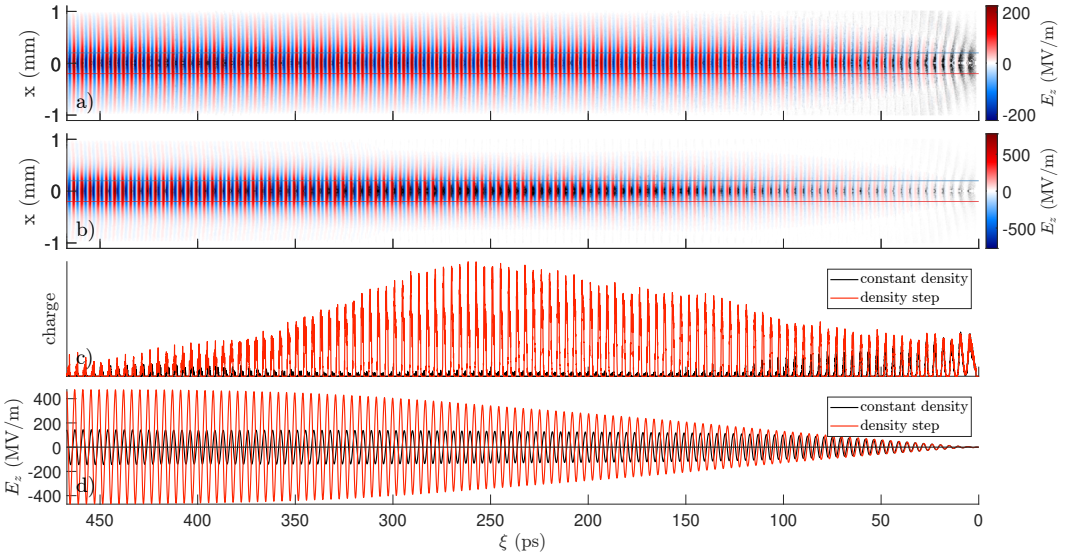

Figure 1.9: Comparison of wakefields and microbunch trains between propagation in plasma with constant density and with a density step. Longitudinal wakefields and density distribution of the microbunch train for the case of a plasma with (a) constant density and (b) density step, both mirrored about the axis (2D axisymmetric geometry). (c) Charge profile of the microbunch train by integrating the density in (a) and (b) in $|x| < 0.2\,\mathrm{mm}$. (d) Lineout of the longitudinal wakefields on axis.

One way to avoid the amplitude decrease is to include a small density step along the plasma [54]. The optimal parameters of the step (initial position, length, and increase in density) depend on n_{pe} and the parameters of the bunch (σ_z, σ_r, charge, γ, and seeding position). The effect of the density step is to produce a longer microbunch train that evolves less and drives wakefields with larger amplitude (Fig. 1.9) and a constant phase after saturation. Figure 1.10, produced using LCODE [47] (see Sec. 1.4) with the parameters in Table 5.3, shows the difference in the evolution of the maximum amplitude of the wakefields between a constant-density plasma and one with a density step optimized for maximum amplitude of the accelerating wakefields. Including a density step leads to higher amplitude wakefields that have a constant amplitude after $z \approx 6\,\mathrm{m}$.

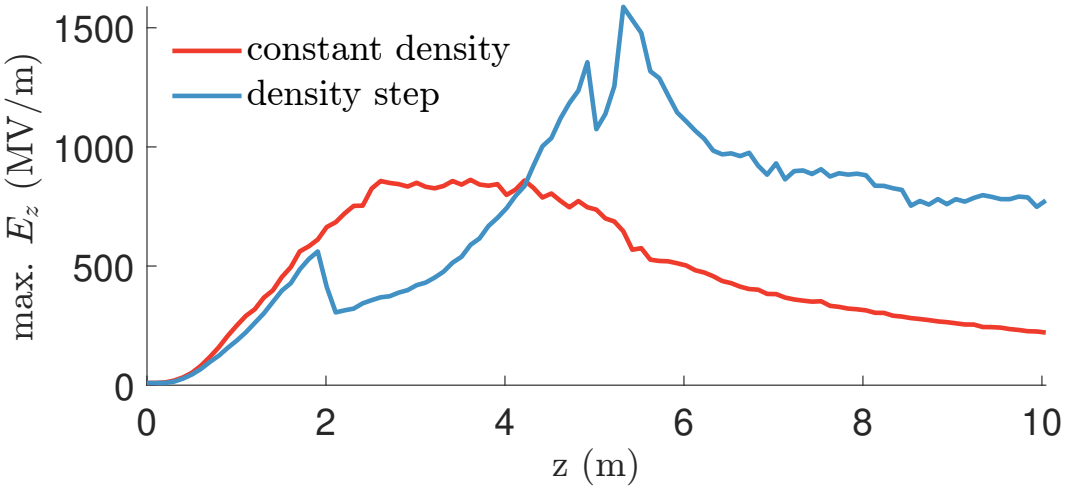

Figure 1.10: Maximum amplitude of the longitudinal wakefields along the constant-density plasma (red) and the plasma with a density step (blue). The peak of the wakefields is around $z \approx 4\,\mathrm{m}$ with the constant-density plasma, after which it continuously decays.

1.2.6 Injection of a particle bunch in the wakefields

To build an accelerator, having a large amplitude and a constant phase of the wakefields is only the first step. The second step is to optimally place a second bunch so that it extracts the energy of the drive bunch through the plasma. There are two methods to do this. One of them is by internal injection, in which plasma electrons are trapped in the wakefields. The other method is external injection, in which the injected bunch is externally accelerated, e.g., by radio-frequency cavities. The latter is the only method considered in this work.

The injected bunch must be shorter than $\lambda_{pe}/4$, since it must fit both in the focusing and accelerating phase of the wakefields, which, according to linear theory, are shifted by a phase of $\pi/2$, as seen in Fig. 1.5. To avoid filamentation [46], the rms width σ_{re} of the electron bunch must satisfy $\sigma_{re} < c/\omega_{pe}$. Furthermore, the bunch must have a density $n_{be} >> n_{pe}$ to create a blow-out of plasma electrons, which is a non-linear response of the plasma, in which all plasma electrons are expelled from the region around the axis, leaving only the ions behind. Here, it is important to note that the microbunch train does not drive a blow-out, since it operates in the quasi-linear regime, an intermediate state between the linear and non-linear regimes. The blow-out is needed to have focusing wakefields which increase linearly with the distance from the axis and therefore match the beam to the wakefields as described in the following.

Beam matching

As the injected bunch creates the blow-out in the plasma, it is focused by the transverse wakefields and simultaneously accelerated by the longitudinal wakefields from the microbunch train. The accelerated bunch typically has a Gaussian transverse profile and its envelope evolution is described by a Hill equation

$$\frac{d^2\sigma_{re}}{dz^2} + \left(\frac{\omega_{pe}^2}{2c^2\gamma} - \frac{\epsilon^2}{\sigma_{re}^4}\right)\sigma_{re} = 0, \tag{1.15}$$

where ϵ is the geometric emittance of the injected bunch. Considering the size of the bunch σ_{re0} at the plasma entrance $z = 0$ m, a constant envelope size $\sigma_{re}(z) = \sigma_{re0}$ along the plasma is maintained when $\frac{d\sigma_{re}}{dz} = 0$. Considering that $\beta = \sigma_{re}^2/\epsilon$, the matching condition dictates

$$\beta_m = \sqrt{2\gamma}\frac{c}{\omega_{pe}}, \tag{1.16}$$

where β_m is the β at which the bunch is matched to the focusing force in the plasma.

The previous discussion refers to the case when the electron bunch is fully inside of a blow-out of plasma electrons, created by another drive bunch. For a dense and short electron bunch injected in the wakefields driven by a microbunch train, the blow-out will start within it, behind its front [55] shown in Fig. 5.18 in chapter 5.

Beam loading

The injected bunch also affects the longitudinal wakefields that accelerate it. The effect of the accelerated bunch on the wakefields must be considered to calculate the effective fields that ultimately accelerate the bunch. This process is called beam loading. The most efficient energy transfer occurs when the superposition of the fields from the drive bunch and the accelerated bunch leave an amplitude of zero behind the accelerated bunch. In this way, all of the energy in the wakefields is transferred to the accelerated bunch. This creates a quick drop of the amplitude of the wakefields. However, to achieve a low-energy spread, the field must be constant along the accelerated bunch. For experimental conditions, i.e., Gaussian bunches, microbunch trains, and quasi-linear wakefields, simulations must be used to optimize beam loading.

1.3 Advanced Wakefield Experiment (AWAKE)

The AWAKE Experiment [12] aims to accelerate electron bunches in the wakefields driven by a relativistic long proton bunch. By using SM to transform the long proton bunch intro a microbunch train, the goal is to drive wakefields with an amplitude of 1 GV/m. These wakefields should ac-

celerate an electron bunch while controlling its emittance and maintaining its energy spread low. The experiment is a part of the CERN accelerator complex. The AWAKE Experiment already proved SM of a long proton bunch [11], seeding of SM [53, 56], acceleration of test electrons from 19 MeV to 2 GeV [57], a detailed understanding of SM physics [48, 49], and complexities of injection dynamics, among many others contributions to wakefields physics. Reference [58] contains a comprehensive overview of the achievements of AWAKE.

Figure 1.11 shows the location of AWAKE as part of the CERN accelerator complex. AWAKE receives the proton bunch from the SPS. Each proton in the bunch has an energy of 400 GeV, with a variable proton population from 1×10^{11} to 3×10^{11}. The bunch profile is approximated by a Gaussian in both longitudinal and transverse directions, with a σ_z measuring 6 to 12 cm and a baseline $\sigma_{r0} = 200\,\mu\text{m}$ at its waist, located at the plasma entrance. The normalized emittance is 3.6 mm mrad and the energy spread is 0.035 %.

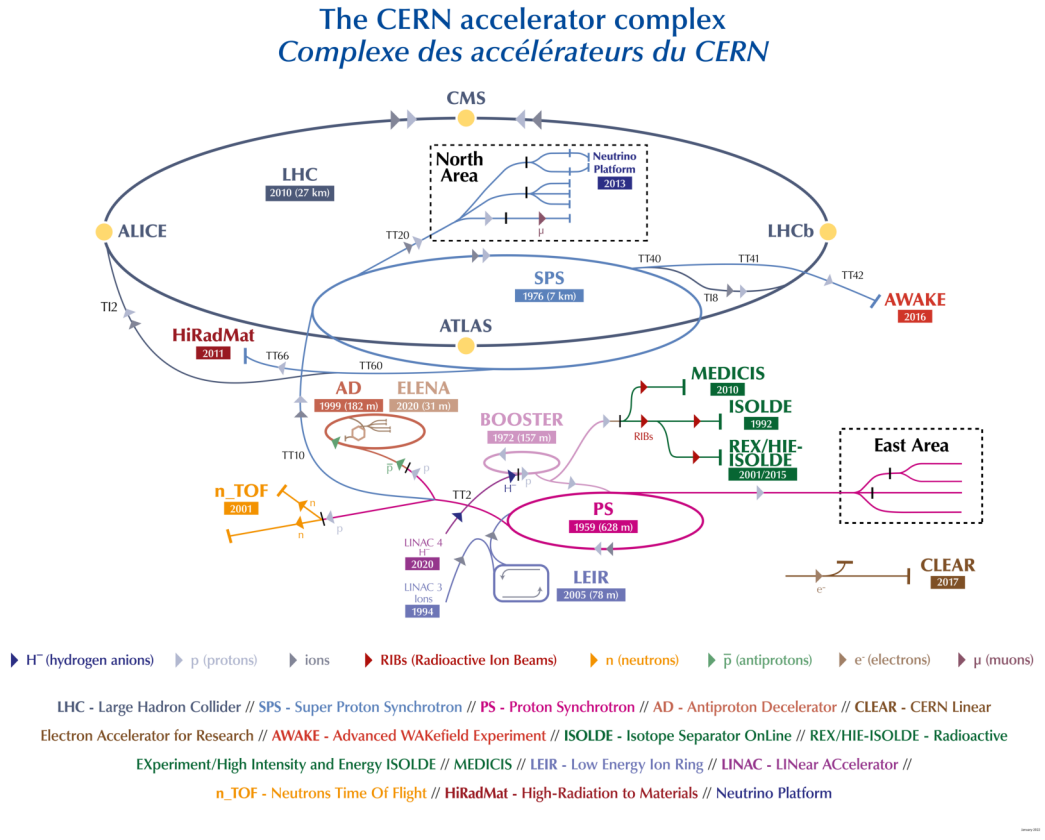

Figure 1.11: Schematic of the CERN accelerator complex as it was in 2022. Image from [59].

The protons are obtained by stripping off the electrons of H atoms using an electric discharge. The acceleration of the protons starts at the LINAC 4, the only linear accelerator in the process,

where they end with an energy of 50 MeV. The protons are transferred next to the Proton Synchrotron Booster where they reach an energy of 1.4 GeV, and then to the Proton Synchrotron for 25 GeV. The final step before reaching AWAKE is the acceleration in the SPS, where they could reach an energy of 450 GeV. A path other than to AWAKE takes them to the LHC, where they reach an energy of 6.5 TeV. A possible future plan for the successor of AWAKE is to use the proton bunches from the LHC, from which more energy can be extracted for acceleration since the acceleration distance would be longer.

1.3.1 AWAKE experimental setup

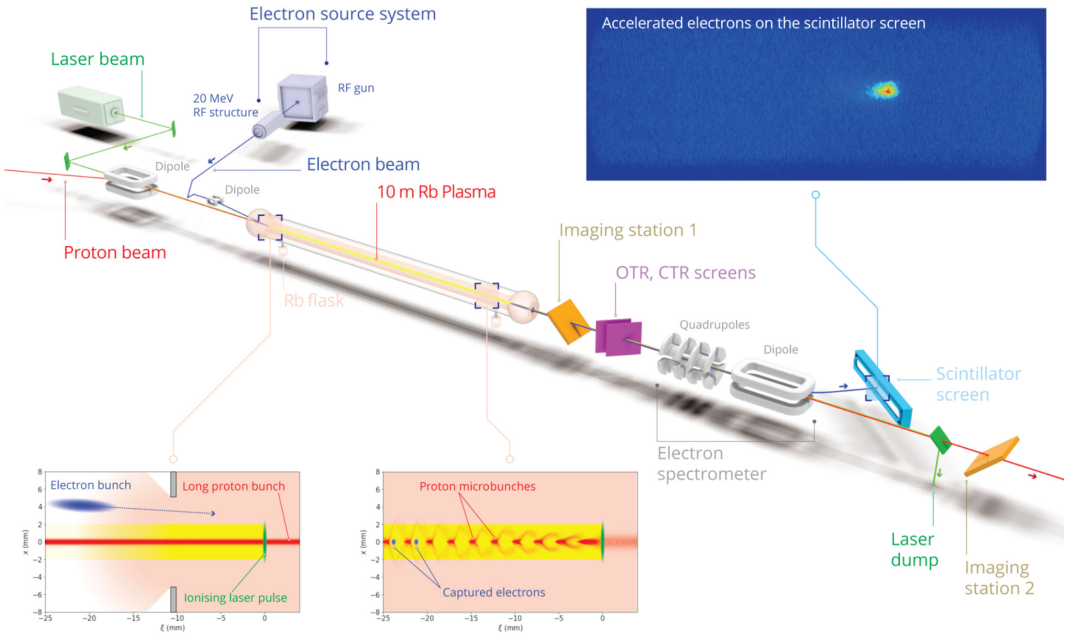

Figure 1.12: Schematic of the AWAKE Experiment layout in run 1 (2018). The left bottom image shows the long proton bunch entering the plasma, together with the electron bunch that is undergoing side injection. The bottom middle image shows the bunch after modulation, now transformed into a microbunch train that resonantly drives wakefields, and a fraction of captured and accelerated electrons. Image from [57].

Figure 1.12 shows the experimental setup of AWAKE during run 1 that finished in 2018. Data from run 1 is used in chapter 3. The proton bunch coming from the SPS enters a 10 m long plasma (left of the image in Fig. 1.12). The plasma is created by ionizing the outermost electron of each Rb atom in a gas coming from reservoirs, that evaporate Rb into the vapor source, located at at the start and end of the source.

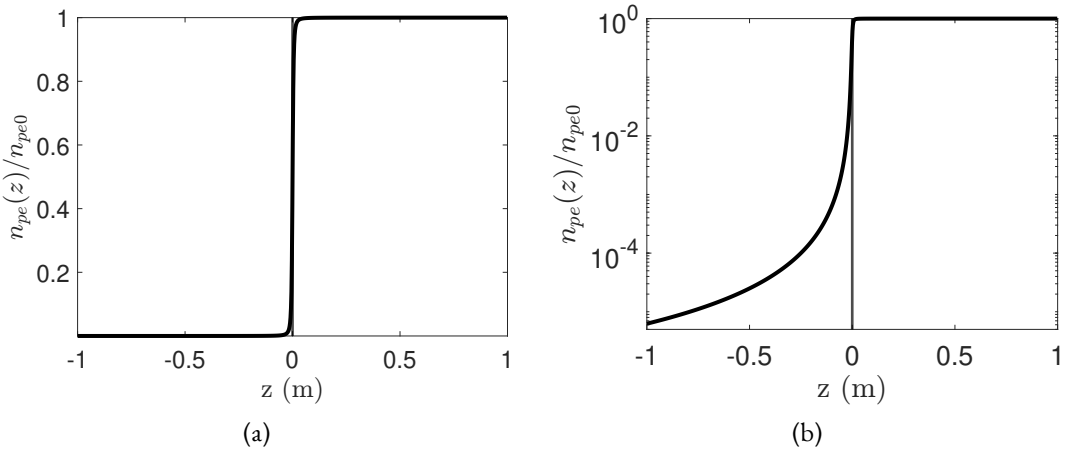

Figure 1.13: Density profile of the plasma ramp leading to the long plasma in (a) linear scale and (b) logarithmic scale. The vertical line at $z = 0$ m indicates the position of the plasma entrance, in which $n_{pe}(z) = \frac{1}{2} n_{pe0}$. A long, low-density ramp before the plasma entrance can be observed.

The vapor flows from both ends of the plasma to expansion volumes. Its density drops quickly as it exits the vapor source, as shown in Fig. 1.13, is described by [60, 61]

$$\frac{n_{pe}(z)}{n_{pe0}} = \frac{1}{2} + \frac{z/2r_o}{2\sqrt{0.25 + \left(\frac{z}{2r_o}\right)^2}}, \tag{1.17}$$

where r_o is the radius of the orifice connecting the vapor source with the expansion volume and n_{pe0} is the density in the constant-density plasma. When the density in the ramp before the plasma entrance is also ionized, a plasma density ramp is created. The response of the plasma in the ramp to the proton bunch is discussed in chapter 5.

To measure the density of Rb vapor, white light interferometry is used and it has an uncertainty of 0.5% [62]. The plasma density is not measured directly, but it agrees with the Rb density [63]. Therefore, throughout this work, I mention the plasma density, although the Rb density was measured. The plasma has a radius of approximately 1 mm, and a uniform density that varies by less than 0.5 % over 10 m [64]. The temperature of the reservoirs can be controlled so that a linear density gradient along the plasma is created [60, 65].

The ionization process is performed by a laser pulse with a duration of 120 fs ($<< \lambda_{pe}/c$), a maximum energy of 450 mJ, and a central wavelength of 780 nm [66]. The laser pulse co-propagates with and within the proton bunch, making a relativistic ionization front (RIF) [51] that creates the plasma inside of the proton bunch. This sudden onset of the full plasma density within the proton bunch is equivalent to a sudden onset of the proton bunch inside of a preformed plasma [67]. The RIF is used to seed the SMI to make it seeded self-modulation (SSM). Seeding is possible be-

cause the sudden onset of proton bunch drives wakefields from which the instability can grow. When seeded, the phase of the wakefields and the bunch modulation with respect to the RIF are reproducible, from event to event, within a small fraction of a modulation period [56].

Together with the proton bunch and laser pulse, a 10 to 20 MeV electron bunch can also be injected either to seed the SM or to be accelerated. It has a $\sigma_{ze} \approx \lambda_{pe}$ and a maximum charge of 600 pC. The electron bunch is created on a photo cathode using a small fraction of the laser pulse used for the RIF. In this way, the relative timing of the bunch and pulse can be precisely controlled.

After leaving the plasma, the proton bunch propagates 3.5 m in vacuum towards a metallic screen. When entering it, optical transition radiation (OTR) is produced and is imaged onto the entrance slit of a streak camera [63, 68]. Since approximately 74 μm around the bunch propagation axis is imaged onto the camera [48, 49], it produces time-resolved images of the bunch density distribution. The electron bunch is focused and bent by quadrupole and dipole magnets onto a scintillator screen, where its energy can be measured from the horizontal position on the screen.

1.3.2 Future experimental setup

The future plan for AWAKE is designed to achieve the goal of providing high-energy electron bunches with properties that are sufficient for high-energy or particle physics applications. One major change for future experiments is the separation of the plasma into two 10 m-long sections, as seen in Fig. 1.14: the first one where SM occurs and the second one for electron bunch acceleration [69]. This is done because the dephasing of the wakefields during SM growth leads to the electron bunch being in defocusing and decelerating wakefields, thus, making the acceleration process ineffective. The two plasma are separated by a 1 m vacuum gap to place the injection devices.

The first plasma includes a density step that is suggested by simulations [54] to stop the microbunch train evolution and the decay of the amplitude of the wakefields (Fig. 1.10). The density step in the experiment will be created by controlling the temperature of the Rb vapor along the plasma source. This will be the first time the effect of a density step on SM will be studied in reality. Some experimental results that will be analyzed are the off-axis charge of the microbunch train, the plasma light, and the energy gain of a probe electron bunch.

The second plasma will have a constant density and will also be created with laser ionization, with the important difference that the laser pulse will be counter-propagating. The laser pulse will enter from the end of the plasma and travel upstream, where it will meet the electron bunch for acceleration at the entrance to the second plasma. This avoids the plasma ramp discussed in the previous section (Sec. 1.3.1). Two other plasma creation mechanisms are considered for the accelerator plasma, which can be extended to hundreds of meters: direct current electrical discharge in noble gases [71] and helicon argon plasma [72] (Fig. 1.15).

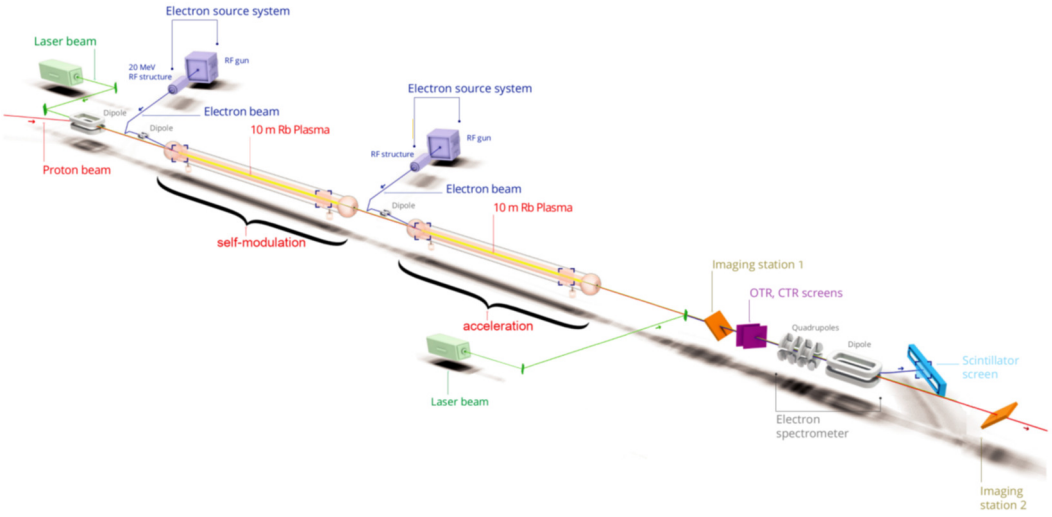

Figure 1.14: Schematic of the AWAKE Experiment layout in run 2c (starting with first protons after LS3 in 2028 [58]). The schematic shows the self-modulator and accelerator plasma, together with the electron source system and measuring screens. The second plasma is ionized by a counter-propagating laser pulse. Image from [58].

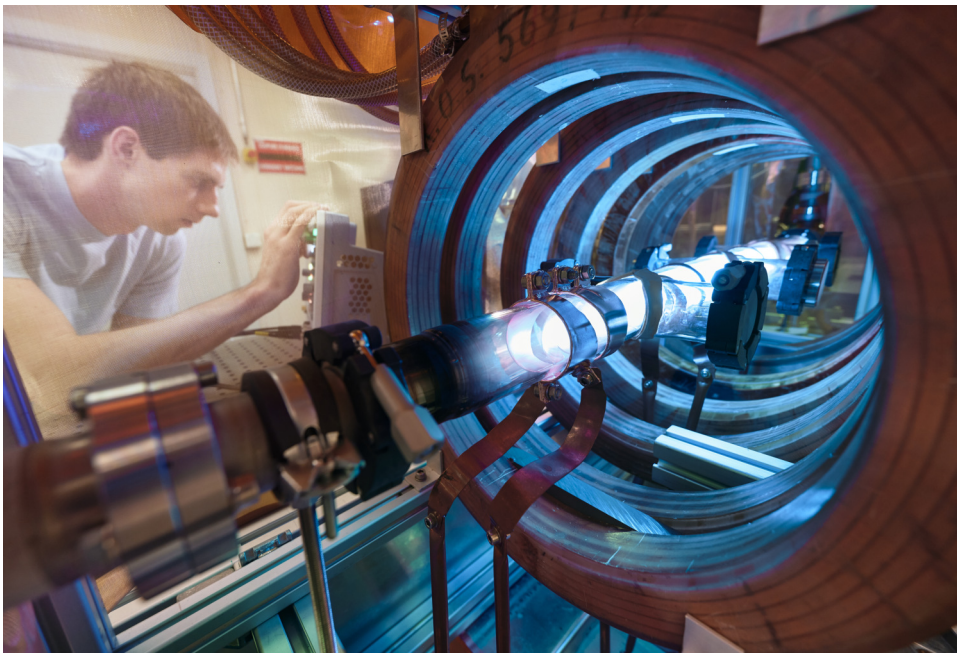

Figure 1.15: Helicon plasma cell in development for AWAKE. Image from [70].

The electron bunch that will be used for acceleration in the second plasma will be delivered by a new source. Its properties are in table 5.1.

1.3.3 Physics applications of AWAKE

With the proton bunch from the SPS, the maximum energy electrons can have is 200 GeV [73]. Considering the proton bunch from the LHC, electrons can be accelerated up to 6 TeV [54]. Since proton drivers have a limitation in their repetition rate, the applications considered involve collisions that do not require a high luminosity. They usually involve fixed targets, protons, ions, positrons, or laser pulses. An overview of the applications is found in [58], and includes, e.g., the investigation of dark photons, non-linear quantum electrodynamics, and physics beyond the standard model such as leptoquarks and quark substructure.

1.4 Particle-in-cell simulations

Numerical simulations are needed when analytical models are not sufficient to completely describe the physics of a problem. In the case of plasma wakefield acceleration relying on SM, there is no theory for the non-linear response of the plasma, and some effects are not included in linear theory, e.g., the charge neutralization of the particle bunch in plasma (see chapter 2). When there is good agreement between the experimental and simulation results, simulations can give an insight into the evolution of a system when it cannot be measured in the experiment. Simulations can also predict results, inspire new research paths, and aid in the design of experiments.

The usual tool to simulate the interaction of the bunch and the plasma in wakefield physics is the particle-in-cell (PIC) method. For the equations used in the PIC algorithm, a unique normalization is applied for two reasons. First, to avoid repeated multiplication by constants that reduces the performance of the algorithm and second, to obtain general results, not bounded by a specific choice of units. The usual normalization, which is also valid in the PIC codes used in this thesis, is based on ω_{pe}, m_e, e, and c. The main quantities are then normalized as follows:

$$n' = n/n_{pe}, \tag{1.18}$$

$$t' = \omega_{pe} t, \tag{1.19}$$

$$\mathbf{x}' = \frac{\omega_{pe}}{c}\mathbf{x}, \tag{1.20}$$

$$\mathbf{E}' = e\frac{c/\omega_{pe}}{m_e c^2}\mathbf{E}, \tag{1.21}$$

$$\mathbf{B}' = e\frac{c/\omega_{pe}}{m_e c}\mathbf{B}, \tag{1.22}$$

$$\tag{1.23}$$

where n is density (e.g., density of the particle species or local plasma density), t is time, $\mathbf{x}$ is position vector, $\mathbf{E}$ is electric field, and $\mathbf{B}$ is magnetic field.

The continuity equation

$$\frac{\partial \rho'}{\partial t} + \nabla \cdot \mathbf{j}' = 0, \tag{1.24}$$

where ρ is the charge density and $\mathbf{j}' = \rho' \mathbf{v}'$ is the current vector, together with the Maxwell equations in normalized units,

$$\nabla \cdot \mathbf{B}' = 0, \tag{1.25}$$

$$\nabla \cdot \mathbf{E}' = \rho', \tag{1.26}$$

$$\nabla \times \mathbf{B}' = \mathbf{j}' + \frac{\partial \mathbf{E}'}{\partial t'}, \tag{1.27}$$

$$\nabla \times \mathbf{E}' = -\frac{\partial \mathbf{B}'}{\partial t'}, \tag{1.28}$$

and the particle equations of motion given by the Lorentz' force $\mathbf{F}$ (Eq. 1.2, in normalized units) are used to describe the physics of the system. This is done by applying the finite-difference method, where the electric and magnetic fields are discretized onto a grid. The particles are placed inside of the "cells" created by this grid, hence "particle-in-cell". Current limitations with the memory of supercomputers allow for a maximum number of particles in the order of 10^8 [74], thus, the particles in PIC simulations, which receive the name of macroparticles, represent an ensembles of real particles. As an example, the proton bunch in AWAKE contains as much as $3{\times}10^{11}$ protons and in this thesis is simulated with 10^6 to 10^7 macroparticles.

The typical loop followed by the PIC method is shown in Fig. 1.16. The charge and current from the macroparticles is deposited on the grid by calculating Eq. 1.24. With this information, the fields are calculated by integrating the field equations. Then, the values of the fields are interpolated to the macroparticle positions. Once the value of the fields is known at the macroparticle positions, the "particle pusher" moves the particles and gives them their new momentum with Eq. 1.2. Usually this is done with the Boris Method [75].

Full electromagnetic PIC codes calculate the fields and move the particles at each time step. One example of such code is OSIRIS [76], which I use to study plasma density gradients in chapter 3 using 2D axisymmetric geometry. The Courant condition [77] establishes that in an explicit time-marching solution for partial differential equations, the distance that information travels in each time step (e.g., electric fields) must be smaller than the spatial step. The Courant condition in OSIRIS is given by

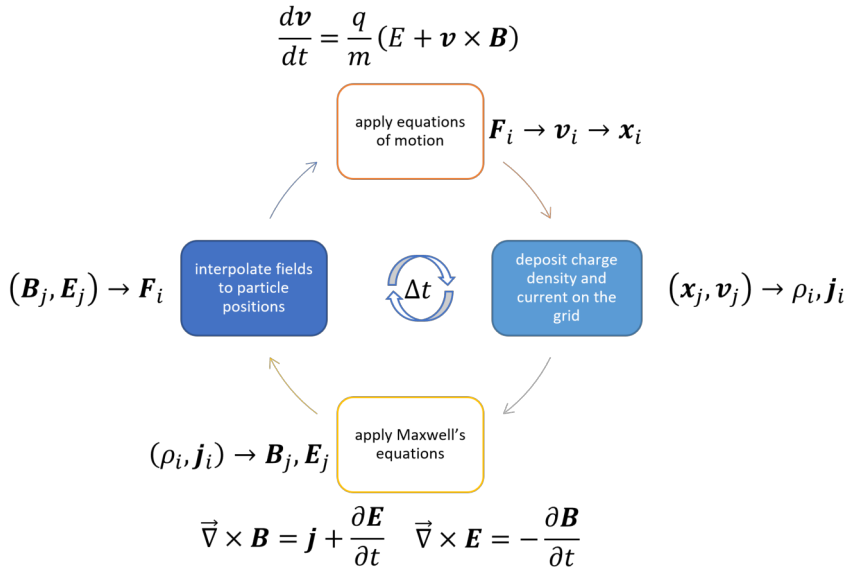

Figure 1.16: Main steps in the PIC cyclic algorithm in normalized units.

$$dt \leq \frac{1}{c} \frac{1}{\sqrt{\left(\frac{1}{dx}\right)^2 + \left(\frac{1}{dy}\right)^2 + \left(\frac{1}{dz}\right)^2}}, \tag{1.29}$$

where dt is the time step, and dx, dy, and dz are the spatial steps. When the system size is large compared to λ_{pe}, the simulation becomes very expensive in computational resources. A small grid size, and therefore small time step, is needed to resolve the plasma waves, but a large simulation window is needed to include the whole system. This is the case in the AWAKE experiment, as the a full proton bunch, taken as $6\,\sigma_z$, can be as long as 72 cm, and λ_{pe} as short as 1.26 mm.

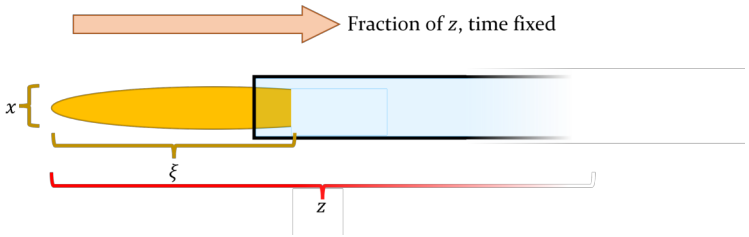

Figure 1.17: Schematic of the coordinates in full electromagnetic PIC codes with a long proton bunch entering the plasma. Each image is taken in a range in z (in SM it is usually a small fraction of the long plasma, e.g., 10 cm compared to 10 m of plasma), while the time stays constant.

In full electromagnetic PIC codes, the data of the system is saved at a fixed time in a range in z the size of the simulation window, as shown in Fig. 1.17. When I mention a position in z when using full electromagnetic PIC codes, I am referring to the middle position of the simulation window.

Nevertheless, bunch macroparticles can be pushed to a certain z-position when propagating in vacuum, e.g., to have a more direct comparison with experimental data which is also measured at a fixed z-position (as is done in chapter 3).

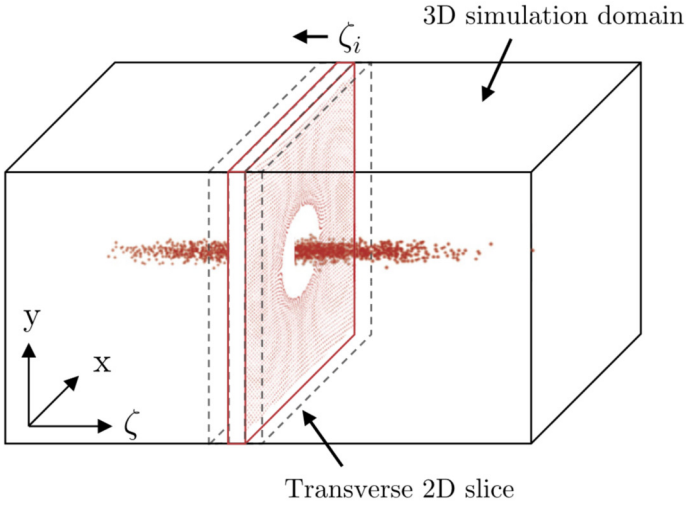

Figure 1.18: Schematic of quasi-static PIC codes in 3D. The plasma response to the beam is calculated slice by slice as a "blanket" going from the front to the back of the bunch. After the "blanket" has gone through some slice of the bunch, those bunch macroparticles can be advanced by a large time step. Figure from [78].

Quasi-static [79] codes exploit the fact that the particles in relativistic bunches evolve much more slowly than the plasma electrons, e.g., an electron bunch in the blow-out regime has betatron oscillations given by $\omega_\beta = \omega_{pe}/\sqrt{2\gamma}$. Quasi-static codes make a clear distinction between the slow movement of the relativistic particles of the bunch and the quick movement of the plasma electrons in the reference frame of the simulation window that is moving at c. All derivatives with respect to the slow time are set to 0.

The algorithm is divided into two main steps. In simplified terms, first, the plasma response to the relativistic bunches is computed slice by slice from the front of the simulation box to the back, as depicted in Fig. 1.18. From the new plasma distribution, the fields acting on the bunch macroparticles can be calculated. Second, the Lorentz' force can be calculated from the fields and particles from the relativistic bunches can then be pushed using a larger Δt than the one needed to comply with the Courant condition, as long as the betatron oscillations of the bunch are well resolved, thereby saving on computation time. Due to causality, the evolution of any given slice only depends on the slices ahead of it. Therefore, after the macroparticles from a slice have been propagated, the plasma response at the next Δt can be calculated, even though the slices behind

are still at the previous Δt. I use the quasi-static code LCODE [47], which uses 2D axisymmetric geometry, for chapters 2, 4, and 5.

In quasi-static PIC codes, the data of the system is saved at a fixed z (one slice of plasma) letting the system evolve in time until the whole simulation window has propagated through that z, as shown in Fig. 1.19. The ξ coordinate here is $\xi = 0$ when the rightmost part of the simulation window is at the fixed z. Then ξ increases as the system advances in time. If the length of the simulation window is ℓ, then $\xi = \ell$ when the leftmost part of the simulation window has propagated through the fixed z. Figures showing this are in chapters 2, 4, and 5. It must be noted that since the particles in the simulations I use are relativistic (e.g., protons have $\gamma = 426$) and they move slowly within the length of the simulation window, there is little difference when comparing the system at a fixed time while scanning the position (full electromagnetic) to the system at a fixed position while scanning the time (quasi-static), and they can be considered equivalent.

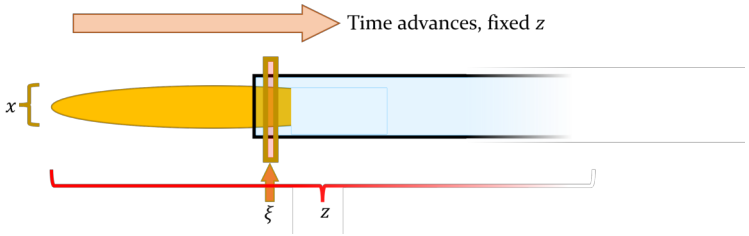

Figure 1.19: Schematic of the coordinates in quasi-static PIC codes with a long proton bunch entering the plasma. Each image is taken at a fixed z, while the time is advancing.

To ensure that the simulation results are independent of the simulation paremeters, convergence tests need to be performed. Since the parameters for the simulations I perform were based on previous simulations and published work [80], a resolution test in space and time and macroparticle number is enough to confirm the validity of the results. I double and half the longitudinal and transverse resolution, as well as the plasma electron macroparticle number and bunches (all bunches present in the same simulation) macroparticle number. Then I check that the features I refer to in this thesis are reproduced with sufficient precision. These are found in Appendix A.

2 Frequency and Amplitude of the Seed Wakefields

"Important thing in science is not so much to obtain new facts as to discover new ways of thinking about them" - Sir William Bragg.

2.1 Introduction

Plasma wakefield accelerators (PWFA) [10] that use a relativistic particle bunch much longer than the plasma wavelength

$$\lambda_{pe} = \sqrt{\frac{\pi}{n_{pe} r_e}}, \tag{2.1}$$

where r_e is the classical electron radius, and n_{pe} is the plasma density, must rely on self-modulation (SM) [34] to drive high-amplitude wakefields for acceleration. The value of this amplitude depends on the length of the microbunch train, the relative position of the microbunches with respect to the wakefields, and the charge in each microbunch. The microbunches must be placed in the decelerating regions of the wakefields to cede their energy and increase the amplitude of the wakefields.

During the propagation of a long proton bunch ($p+$) in a constant-density plasma, the amplitude of the wakefields grows, reaches a maximum value, and then decreases due to the evolution of the microbunch train after saturation of the SM [81]. One of the reasons for this evolution is the continuous phase shift of the wakefields, while the microbunches remain in place. In order to prepare a setup where a large amplitude over distances interesting for acceleration[1] is maintained, the SM process of a long bunch and the consequent evolution of the microbunch train must be well understood. One aspect not considered in the linear theory of the wakefields is the effect of charge neutralization by plasma electrons of the continuous charge of the proton bunch on the plasma oscillation frequency.

The wakefields are sustained by the distribution of the plasma electron density, where, according to linear theory [82], the plasma electrons oscillate with the frequency

[1] In the case of AWAKE, hundreds of meters.

$$f_{pe} = \frac{\omega_{pe}}{2\pi} = \frac{1}{2\pi}\sqrt{\frac{n_{pe}e^2}{m_e\varepsilon_0}}, \tag{2.2}$$

where e is the electron charge, m_e is the electron mass, and ε_0 is the vacuum permittivity. The oscillation frequency of plasma electrons is perturbed when considering a relativistic, long, charged particle bunch propagating through the plasma. I specify this perturbed frequency as $f_{pe,osc}$, to indicate it may differ from the expected frequency in a constant-density plasma without a charged particle bunch, which is f_{pe}. In a plasma, electrons flow towards or move away from axis to neutralize the charge of an injected bunch, as shown in Fig. 2.1 for the case of a long proton bunch just as it enters the plasma at $z = 0\,\mathrm{m}$, where z is the distance along the plasma. The neutralization of the charge of a positively charged bunch locally increases the plasma electron density. The neutralization of a negatively charged bunch has the opposite effect. This setup is equivalent to having a plasma with a density that varies transversely and longitudinally. Figure 2.2 shows that the amplitude of the plasma electron oscillations is small compared to the width of the bunch, so that the electrons oscillate in a perturbed plasma density.

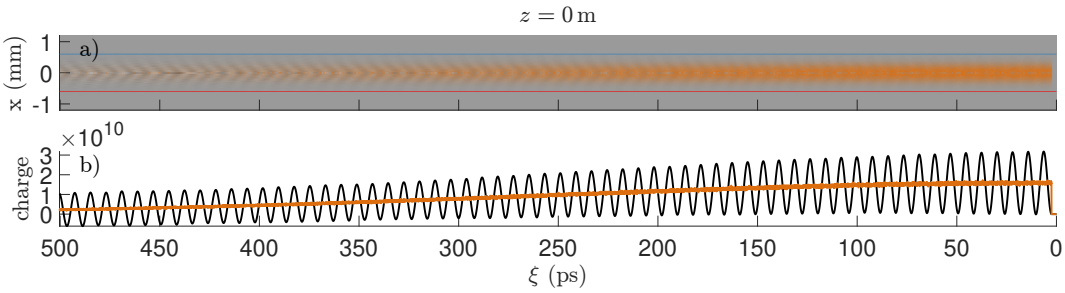

Figure 2.1: (a) Plasma electron (gray) and proton bunch (orange) density distributions, mirrored about the axis (2D axisymmetric geometry). The proton bunch is propagating to the right. (b) Charge profile of the plasma electron distribution (black) and proton bunch distribution (orange) obtained by integrating their respective density distribution in the region $|x| < c/\omega_{pe} = 0.376\,\mathrm{mm}$. For the plasma electron distribution, n_{pe} was subtracted prior to integrating to observe only the perturbation. The value of the plasma electron charge profile oscillates around the proton bunch charge.

A simple approach to calculate the perturbed plasma electron oscillation frequency is to include the initial particle bunch density distribution n_b along ξ and across x the bunch in ω_{pe}, so that the new frequency has the form [83]

$$f_{pe,osc}(n_{pe}, n_b(\xi,x)) = \frac{1}{2\pi}\omega_{pe}(n_{pe}, n_b(\xi,x)) = \frac{1}{2\pi}\sqrt{\frac{(n_{pe} \pm n_b(\xi,x))e^2}{m_e\varepsilon_0}}, \tag{2.3}$$

where n_b is the density distribution of the bunch.

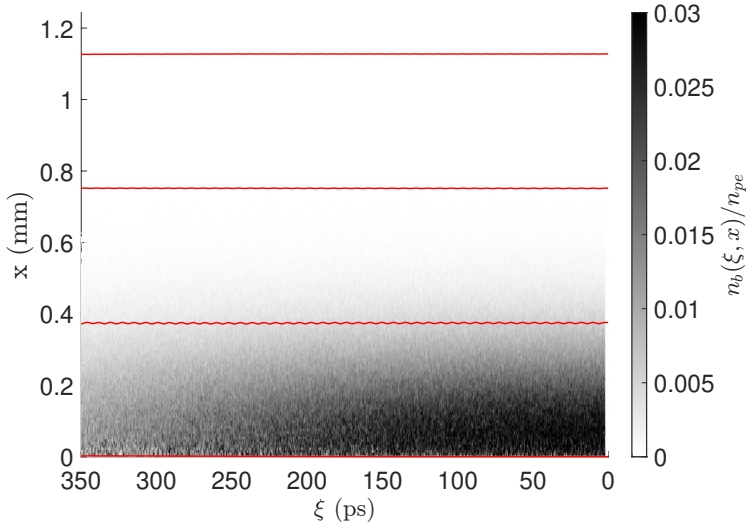

Figure 2.2: Density of the proton bunch (gray) propagating to the right with tracks (red lines) of individual oscillating plasma electrons spaced transversely by $c/\omega_{pe} = 0.376\,\mathrm{mm}$.

The magnitude of the perturbation in the frequency depends on the ratio of n_b to n_{pe}. For a radially and longitudinally Gaussian bunch, where n_b reaches several percents of n_{pe}, as is the case for current PWFA relying on SM [12], $f_{pe,osc}(n_{pe}, n_b(\xi,x))$ has a radial and longitudinal dependency. As the plasma electrons oscillate, they create regions of concentration and depletion of plasma electrons, which sustain the wakefields. Since the plasma electrons start their oscillation at the same seed position along the bunch, when they oscillate at different frequencies, their relative phase will also be different and this difference increases with ξ. This dephasing leads to less concentration and less depletion of plasma electrons, which means that the wakefields they sustain have a lower amplitude.

The transverse wakefields, which have the same frequency as the plasma electron oscillations, modulate the proton bunch density. Therefore, $f_{pe,osc}$ establishes the initial modulation frequency f_{mod} of the bunch. This frequency perturbation is an important parameter to consider when designing plasma density profiles for higher amplitude wakefields for long distances, i.e., plasma density gradients [48, 49] (and discussed in chapter 3) and plasma density step [54].

2.2 Simulation results and comparison with model

2.2.1 Simulation parameters

I use particle-in-cell simulations to measure the dependency of the frequency of the seed wakefields on n_b, which has a maximum value n_{b0}.

Table 2.1: Simulation parameters based on the baseline for AWAKE.

Plasma and window param.	**Value**	**Bunch param.**	**Value**
Plasma density (n_{pe})	$2\times10^{14}\mathrm{cm}^{-3}$	RMS radius (σ_r)	200 µm
Plasma radius	2.63 mm	RMS length (σ_z)	7.5 cm
Simulation window duration	1067 ps	Norm. emit. (ϵ_N)	3.6 mm mrad
Simulation window width	2.67 mm	Relativistic factor (γ)	426.4
Longitudinal resolution	0.025 ps	Relative energy spread	0.035%
Transverse resolution	7.5 µm	Charge (whole bunch)	changing
Macroparticles per cell	10	Macroparticles	1.2×10^{7}

Simulations were performed using LCODE [47] with 2D-axisymmetric geometry, with simulation parameters selected after appropriate convergence tests (Appendix A) and displayed in Table 2.1. The setup is based on the AWAKE baseline[2] using various bunch charges. I use a proton and an antiproton ($p-$) bunch with a Gaussian density distribution, both radially and longitudinally. The relativistic ionization front [51, 56, 63] which enables the seed wakefields in the experiment is replaced by a Heavyside step function $H(\xi \approx 0\,\mathrm{mm})$ at the position of n_{b0}, to have the maximum ratio n_b/n_{pe}. The frequency of the wakefields is obtained by performing a discrete Fourier transform (DFT) on lineouts of the wakefields at various ξ- and x-positions. The DFT is performed with 0.3 GHz spacing. This frequency step corresponds to the accuracy of the plasma density measurement in the experiment [84]. I select the peak of the DFT power spectrum as the frequency of the wakefields. The frequency obtained by this method will be denominated f_s.

2.2.2 Wakefields frequency in simulations vs simplified model

Frequency as a function of bunch density

Figure 2.3 shows the behavior of f_s of both transverse and longitudinal wakefields and for both charge signs of the bunch (protons in black and antiprotons in red) as a function of n_{b0}. For all n_{b0}, given that $|1-\frac{f_s}{f_{pe,osc}}|<1\%$, the model and the simulation results are in agreement. For $n_{b0}=10^{-4}n_{pe}$, $f_s=f_{pe,osc}(n_{pe},n_{b0})=f_{pe}$ within the frequency bin. Positively charged bunches increase f_s, while negatively charged ones decrease it, with the magnitude of the change increasing while n_{b0} increases. The model is a simplification that does not consider the radial dependency of the oscillation frequency of plasma electron in a cylindrical geometry following Dawson's model for cylindrical non-linear plasma waves [44] nor the fact that, in the movement required for one period, the plasma electron follows a path that goes through a varying bunch density, and therefore a varying plasma electron density. For the cases treated here, $n_{b0}<n_{pe}$ always, so a non-linear response of the plasma is not expected, nor plasma electrons becoming relativistic. Nevertheless,

[2] Except for the plasma radius, which is larger than the baseline to avoid noise at the simulation box edges when using low-density bunches ($n_{b0}=10^{-4}n_{pe}$).

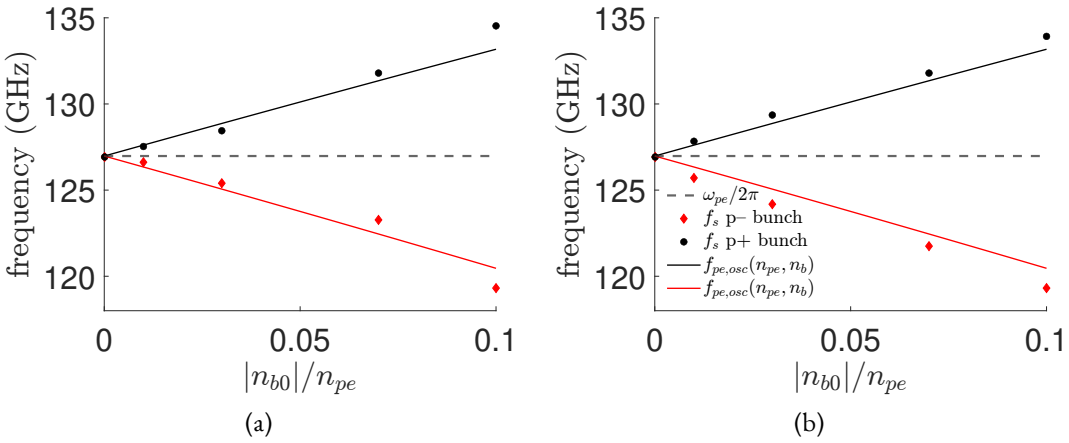

Figure 2.3: Frequency of the initial wakefields f_s (peak of the power spectrum) considering a lineout in the range $\xi = 0$ to 250 ps for various proton (black) and antiproton (red) bunch densities n_{b0}. (a) Longitudinal wakefields. Lineout on axis. (b) Transverse wakefields. Lineout at $x = 0.1$ mm. The continuous lines correspond to $f_{pe,osc}(n_{pe}, n_{b0})$.

I note here that these two effects are not included in the model either. Despite the simplifications, the trends and values of the model and simulations agree, since their relative difference is at the percent level, and they follow the same trend.

Frequency as a function of transverse distance from the axis and its effect on amplitude

Figure 2.4 shows the dependency of f_s on the transverse position. I measured f_s of lineouts within $\xi = 0$ to 250 ps from longitudinal wakefields at various transverse distances from the axis and compared them to $f_{pe,osc}(n_{pe}, n_b(x))$, calculated considering the local transverse bunch density in the center of the bunch (the position where $n_b = n_{b0}$). I mirror the values about the axis for a better visibility of the results.

With $n_b = 10^{-4} n_{pe}$, the code reproduces the expected frequency from linear theory as $f_s = f_{pe}$ [Fig. 2.4(a)] within the value of the frequency bin. With $n_b \approx 0.03 n_{pe}$ both positively [Fig. 2.4(b)] and negatively [Fig. 2.4(c)] charged bunches have the same behavior considering a change of sign of the bunch charge. The value of f_s follows the trend given by $f_{pe,osc}(n_{pe}, n_b(x))$: f_s on axis shows the largest difference to f_{pe} and f_s approaches f_{pe} as the distance from the axis increases. Furthermore, in $|x| \geq c/\omega_{pe}$, $f_s(p+)$ is larger than $f_{pe,osc}(n_{pe}, n_b(x))$ and $f_s(p-)$ is smaller.

Figure 2.5 shows that the different frequencies at different transverse distances lead to a banana shape of the wakefields and to a decrease of the wakefields amplitude along ξ as the electrons oscillate less resonantly, clearly visible, e.g., around $\xi = 240$ ps. Since the frequency of the wakefields comes from the plasma electron oscillation frequency, this means that the crests and throughs of

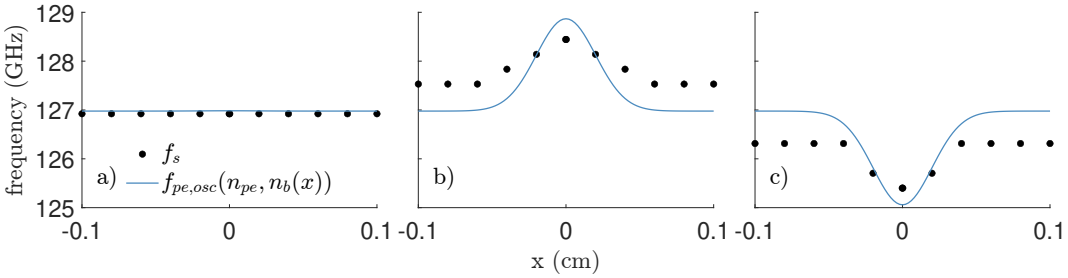

Figure 2.4: Frequency of the longitudinal wakefields f_s (dots) considering lineouts at various transverse distances from the axis and $f_{pe,osc}$ (continuous line) for (a) $n_{b0} = 10^{-4} n_{pe}$, (b) $n_{b0} = 0.03 n_{pe}$, and (c) $n_{b0} = -0.03 n_{pe}$.

the plasma electron oscillations are not aligned transversely, and this misalignment increases with ξ. This leads to regions with less depletion or concentration of plasma electrons as ξ increases, and therefore a decrease in amplitude of the wakefields with ξ, which can also be seen in Fig. 2.5.

The plasma electron oscillation amplitude varies with transverse distance, as seen in Fig. 2.2. Due to the differences in oscillation amplitude and frequency, particle trajectory crossing occurs [83]. This takes energy away from the wakefields and further decreases their amplitude, as the plasma electrons carrying kinetic energy escape the wakefields.

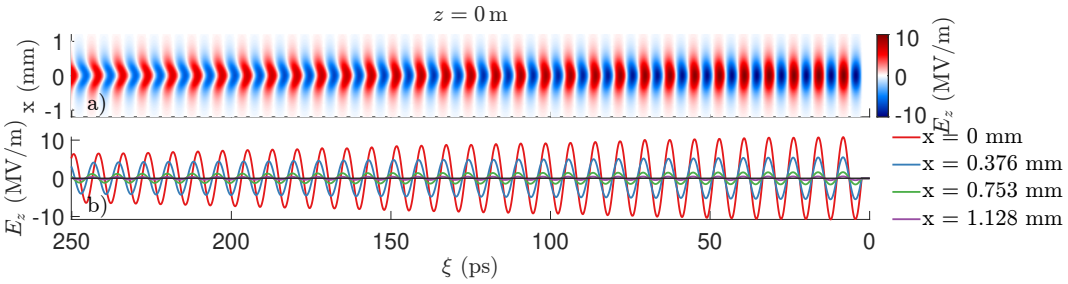

Figure 2.5: (a) Longitudinal wakefields driven by a proton bunch propagating to the right with $n_{b0} \approx 0.03 n_{pe}$. Banana-shaped wakefields most clearly seen around $\xi = 240$ ps. (b) Lineout of the longitudinal wakefields at various transverse distances from the axis. Phase difference due to oscillation frequency difference clearly observed at $\xi = 240$ ps.

Frequency as a function of time delay from the seed

I measured f_s from on-axis lineouts of longitudinal wakefields in longitudinal segments of 157.4 ps, which corresponds to ~20 plasma electron oscillations considering f_{pe}. Figure 2.6(a) shows that for $n_{b0} = 10^{-4} n_{pe}$, $f_s = f(n_{pe}, n_b(x)) \approx f_{pe}$ all along ξ.

For $n_b \approx 0.03 n_{pe}$ in Fig. 2.6(b), and its negatively charged counterpart in Fig. 2.6(c), f_s is in agreement with $f(n_{pe}, n_b(\xi))$ with a maximum relative difference < 0.3%. With ξ closest to 0 ps, which is the point where n_b is maximum, f_s is most different to f_{pe}. As ξ increases and therefore

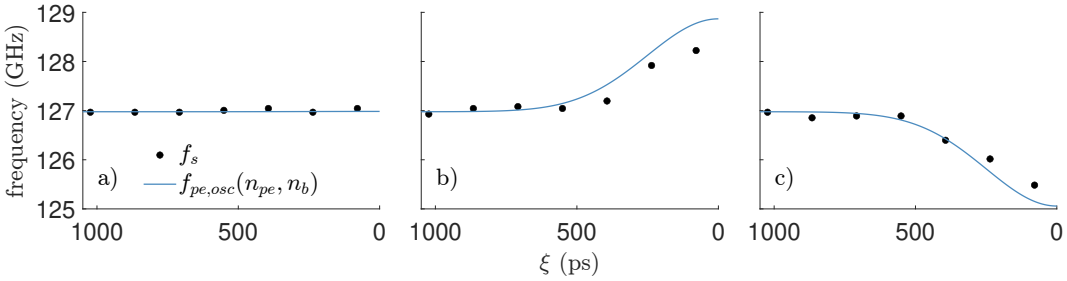

Figure 2.6: Frequency of the longitudinal wakefields f_s (dots) considering lineouts on axis in segments along ξ and $f_{pe,osc}$ (continuous line) for (a) $n_{b0} = 10^{-4} n_{pe}$, (b) $n_{b0} = 0.03 n_{pe}$, and (c) $n_{b0} = -0.03 n_{pe}$. The frequency value is placed at the middle of each segment used for the DFT calculations. The bunch front is at $\xi = 0$ ps.

the $n_b(\xi)$ decreases, f_s tends to f_{pe}. At $\xi > 600$ ps, f_s reaches f_{pe}, and has values slightly below and above it in both cases. In the experiment, $n_b(\xi) = 0$ at some point behind the bunch center, so it is expected that $f_{pe,osc} = f_{pe}$ after the bunch.

2.3 Implications for particle acceleration in plasma using a long microbunch train

Considering two microbunch trains in which all microbunches have the same charge and assuming all microbunches are positioned in the decelerating phase of the wakefields, a longer microbunch train will drive higher amplitude wakefields. Therefore, forming and maintaining a long microbunch train is beneficial for acceleration.

The initial (or seed) wakefields imprint their frequency on the bunch density distribution, so that the initial f_{mod} is different from f_{pe}. I reported before, using simulations, that the initial f_{mod} of a long proton bunch is a few percent higher than f_{pe} [49], in agreement with this chapter. During propagation in a constant-density plasma, the frequency of the wakefields decreases along z during SM growth due to the phase slippage of the wakefields [13, 14, 48, 49] (and discussed in chapter 3) and continues to slip after saturation due to the evolution of the microbunch train. In chapter 3, I show with simulations that f_{mod} is also continually decreasing along z and it does at a slower pace than f_s, due to the slower movement of relativistic protons compared to plasma electrons. In general, f_{mod} changes due to the focusing and defocusing of protons by the transverse wakefields. I also show with simulations that in order for f_{mod} to be equal to f_s, the majority of the microbunches are expelled, since the decreasing f_s means that the microbunches that were in focusing wakefields earlier along the plasma, are in defocusing ones as z increases. Only the microbunches at the front remain.

When the periodicity of microbunches of a fully modulated bunch is different from that of wakefields, considering they have the same starting time (or position), dephasing between microbunches and wakefields occurs. This difference in the time delay between the focusing regions of the wakefields and microbunches leads to loss of charge, as protons are subject to defocusing wakefields that push them outside of the wakefields, where they cannot be focused back to the axis by focusing wakefields. This difference also increases with ξ, so that microbunches in the bunch rear are affected earlier during propagation than those in the front.

A density step [54] has been proposed to create a microbunch train that drives wakefields with a large amplitude and that evolves more slowly and, therefore, drives wakefields with a constant phase, after SM saturation over distances interesting for acceleration. A good understanding of the relation between the seed wakefields frequency, initial f_{mod}, and f_{pe} is necessary to explain the role of the density step in the SM growth and saturation. Furthermore, the decrease in wakefields amplitude along ξ, not described by linear theory, is relevant to understand the results of measurements performed at or near the plasma entrance, e.g., plasma light or shadowgraphy.

2.4 Conclusions

I show with simulations that, as expected, the frequency of the wakefields is affected by a long charged particle bunch propagating through plasma due to charge neutralization. This effect is clearly visible at the plasma entrance, where the bunch charge distribution is not yet modulated. The distribution of the plasma electrons follows that of the bunch. Therefore, the situation is equivalent to having a plasma density that varies with longitudinal and transverse position.

I propose a simplified model to describe the perturbed plasma electron oscillation frequency and therefore the frequency of the wakefields they sustain. I show that the model and the simulations have a good agreement, especially close to the bunch propagation axis. Finally, I show that the difference in plasma electrons oscillation frequencies at different transverse distances leads to a banana shape of the wakefields and a decrease of the wakefield amplitude along the bunch from front to back.

These effects are relevant to understand the evolution of the bunch along the plasma and the techniques to stop its evolution, such as the density step. They are also relevant to understand measurements regarding the amplitude of the wakefields or plasma electron oscillations at the plasma entrance, such as plasma light and shadowgraphy.

3 Self-Modulation in Plasma with Density Gradients

"Any intelligent fool can make things bigger, more complex, and more violent. It takes a touch of genius – and a lot of courage – to move in the opposite direction" - Ernst Friedrich Schumacher

"It is impossible to travel faster than the speed of light, and certainly not desirable, as one's hat keeps blowing off" - Woody Allen

3.1 Introduction

A relativistic proton bunch much longer than the plasma wavelength

$$\lambda_{pe} = \sqrt{\frac{\pi}{n_{pe} r_e}}, \tag{3.1}$$

where r_e is the classical electron radius, and n_{pe} is the plasma density, drives high-amplitude wakefields only after undergoing self-modulation (SM), in which it transforms into a microbunch train. The microbunches have a spacing given by $\approx \lambda_{pe}$ and resonantly drive wakefields, which reach amplitudes approaching the wave-breaking field [85] $E_{WB} = m_e c \omega_{pe}/e$, where m_e is the rest electron mass, e its charge, c the speed of light, and $\omega_{pe} = 2\pi c/\lambda_{pe}$. Theory [13, 14] suggests that during SM growth, the phase velocity of the wakefields v_{ph} is slower than the bunch v_b, both along the bunch ξ and the plasma z. The difference in velocities, considering a constant-density bunch, is given by [13]

$$|\Delta v| \approx \frac{1}{2}\left(\frac{\xi}{z}\right)^{1/3}\left(\frac{n_{b0} m_e}{n_{pe} m_p \gamma}\right)^{1/3} v_b, \tag{3.2}$$

where m_p is the proton rest mass, γ is the relativistic factor of the bunch, and n_{b0} is the bunch density. After SM saturation, the continuous evolution of the microbunch train also leads to dephasing.

The microbunches must be in the focusing and decelerating regions of the wakefields to drive high-amplitude wakefields over long distances[1]. When there is a shift between microbunches and phase of the wakefields, microbunches that were previously in the focusing and decelerating regions will be partially or completely in the defocusing and accelerating ones. By being in the accelerating regions, the microbunches take energy from the wakefields and make the amplitude of the wakefields decrease. Microbunches in defocusing regions will be eventually expelled from the wakefields, which will prevent an increase in wakefield amplitude further along ξ.

A positive plasma density gradient g, in which the plasma density increases linearly with z, has been proposed as a method to partially compensate for the detrimental effects of the dephasing due to SM by introducing an increase in v_{ph} [13, 14]. It has even been demonstrated with simulations that positive plasma gradients with a limited extent have the same effect as a density step [86]. While n_{pe} increases, $\lambda_{pe} \propto n_{pe}^{-1/2}$ decreases, making any constant phase point move closer to the SM seeding position along the bunch. Positive gradients can be used to reduce Δv (Eq. 3.2), which leads to longer trains [48] that can drive higher-amplitude wakefields [87]. On the contrary, a negative density gradient increases λ_{pe} and enhances the dephasing already occurring from SM. Assuming that the modulation frequency of the bunch f_{mod} is similar to the plasma frequency $f_{pe} = \omega_{pe}/2\pi = c/\lambda_{pe}$, where c is the speed of light, positive gradients increase f_{mod} and negative ones decrease it. Considering Eq. 3.2 and that the phase velocity difference $|\Delta v_g|$ due to the gradients is [48]

$$|\Delta v_g| = \frac{\xi}{2} \frac{g/100}{\sqrt{1+gz/100}} v_b, \tag{3.3}$$

where g is given in percentage, it is important to note that the contributions from both effects are only equal at most at one position in ξ for each position z. Nevertheless, the general effect is to reduce the difference between v_{ph} and v_b with $g > 0$.

In a constant-density plasma, the dephasing negatively affects electron bunch acceleration within the proton bunch. The electron bunch is subject to decelerating fields, decreasing the energy gain, and to defocusing fields, which could expel it from the wakefields.

We published experimental results showing the effects of plasma gradients on the charge and frequency of the microbunch train [48]. These effects were measured after 10 m of plasma propagation and 3.5 m of vacuum propagation. The experimental results show that $g > 0$ leads to longer microbunch trains with more charge when compared to $g < 0$. Furthermore, they show that indeed $g > 0$ increases f_{mod} while $g < 0$ decreases f_{mod}.

In the experiment, neither the characteristics of the wakefields nor those of the proton bunch inside the plasma could be measured. To understand the bunch and wakefield evolution along the

[1] In the case of AWAKE [12], hundreds of meters.

plasma, we use numerical simulations. In simulations we have access to the characteristics of the bunch, the wakefields, and the plasma for the entirety of the propagation distance. I use OSIRIS 4.4.4 [76], a particle-in-cell code, in 2D axisymmetric geometry, to perform the simulations, with parameters based on [48].

I previously published in [49] some results that are included in this chapter. There, we established the good agreement between simulation and experimental results. This was done by comparing the density profile of, the charge in, and f_{mod} of the microbunch trains for the different g values.

Here, I compare the density profiles of the microbunch trains obtained in simulations and experiment for all g values measured in the experiment, from which a subset is already shown in my previous publication [49]. I show that the length of the trains has a dependence on g. I show the phase of the transverse wakefields W_r for different ξ_0 positions along the bunch, together with the positions of microbunches, which explains the train lengths and charges observed after the plasma end. I show the frequency of the wakefields together with f_{mod} along the plasma, as well as their dependence on g, where we already discussed f_{mod} along the plasma in [49]. Finally, I show that a slight positive gradient produces longer microbunch trains that drive wakefields with higher amplitude than using no gradient. These wakefields accelerate test witness electrons to higher energies, as was also measured in the experiment [57, 88].

3.2 Experimental setup and simulation parameters

In these experiments, the proton bunch comes from the SPS in CERN and has a population of $(2.98\pm0.16)\times10^{11}$ protons, with an energy of 400 GeV per proton. Its rms duration is $\sigma_t = 230$ ps, which corresponds to a rms length $\sigma_z = 6.9$ cm. As in [48, 49], we assume the bunch transverse size $\sigma_{r0} = 0.2$ mm at the plasma entrance. The normalized emittance is $\epsilon_N = 3.6$ mm-mrad.

The seeding of SM is obtained through a relativistic ionization front (RIF) [51, 56, 63] created by a 120 fs-long laser pulse with an energy of ≈ 110 mJ co-propagating with the proton bunch in Rb vapor. The laser pulse ionizes the outermost electron of each atom of Rb to create the plasma. At the position of the RIF, the plasma-bunch interaction starts suddenly enough so as to generate the seed wakefields from which the SM can grow [56, 63]. Seeding of the SM is important to reproduce the phase of the wakefields event after event, and, therefore, to know where to inject an electron bunch for acceleration in the experiment.

The plasma density is inferred from the Rb vapor density measurement [63] using white-light interferometry, which gives an uncertainty on the value of 0.5 % [84]. The Rb density is in agreement with the plasma density [63]. Even though the measurements mentioned hereafter correspond to Rb density, I will treat them as plasma density. The density gradient is created by con-

trolling the temperature of the Rb reservoirs, which are located at the entrance and exit of the plasma [60, 65]. The value of the density gradient is obtained by

$$g = \left(n_{pe,\text{start}} - n_{pe,\text{end}}\right) / \left(n_{pe,\text{start}} L\right) \cdot 100\%, \tag{3.4}$$

where $L = 10\,\text{m}$ is the plasma length, and $n_{pe,\text{start}} = 1.81 \times 10^{14}\,\text{cm}^{-3}$ in all cases.

After propagating in plasma, the bunch further propagates 3.5 m in vacuum to a metallic screen. The interaction of the bunch with the screen produces optical transition radiation (OTR) [63, 68], that is imaged onto the entrance slit of a streak camera. With this, we obtain time-resolved images of the bunch density distribution of a 0.074 mm-wide slice centered on its axis. The slice is small compared to the width of the bunch at the screen $\sigma_{r,\text{screen}} = 0.536\,\text{mm}$ when propagating without plasma. The experimental images were obtained by stacking and stitching together multiple, 209 ps, single images [89]. Because the SM is seeded and the phase of the bunch modulation is reproducible, the images form microbunch trains, as opposed to a blur [56], Figs. 3.1(a)(c)(e)(g) and 3.2(a)(c)(e)(g).

Table 3.1: Simulation parameters based on AWAKE [48].

Plasma and window param.	**Physical value**
Initial plasma density (n_{pe})	$1.81 \times 10^{14}\text{cm}^{-3}$
Plasma radius	1.5 mm
Plasma length (L)	10.2 m
Simulation window length	21 cm
Simulation window width	1.58 mm
Longitudinal resolution	5.9 μm
Transverse resolution	4 μm
Time step	9.2 fs
Particles per cell	3×3
Bunch param.	
RMS radius (σ_{r0})	200 μm
RMS length (σ_z)	6.9 cm
Norm. emit. (ϵ_N)	3.6 mm mrad
Seed position (ahead of bunch center)	3.81 cm
Relativistic factor (γ)	426.44
Relative energy spread	0.035 %
Population	3×10^{11} protons
Peak density	$6.9 \times 10^{12}\,\text{cm}^{-3}$
Particles per cell	2×2

The simulation parameters, chosen after suitable convergence tests (Appendix A), are in Table 3.1. In simulations, the RIF is replaced by a Heavyside step function on the proton bunch density profile at the same position along the bunch as the RIF. The right edge of the simulation window is at $\xi = 0\,\mu\text{m}$, the seeding position is $\xi = 8\,\mu\text{m}$, and the bunch center is at $\xi = 3.8108$ cm. Effects such as hosing [90] are excluded in 2D simulations, but 2D simulations reproduce im-

portant effects seen in the experiment. No severe transverse asymmetries were observed in the experiment, although small ones are observed at the bunch rear in the cases with $g > 0$. After the plasma, all simulation macroparticles were propagated in vacuum to $z = 13.5$ m so as to compare with experimental results.

The g values measured in the experiment are −1.93, −0.93, −0.52, +0.03, +0.43, +0.87, +1.30, and +2.00 %/m. In order to cover the same span as in the experiment, we use nine g values from −2 to +2 %/m with a step of 0.5 %/m in simulations. For simplicity, I refer to g values using the closest simulation value. The bunches from both simulations and experiment are shown propagating to the right.

3.3 Density profile of the microbunch train

I display in Figs. 3.1 and 3.2 time-resolved images of all g values measured in the experiment. The values $g = -2, 0$, and +2 %/m were published in [48] while $g = -1$ and +1 %/m were published in [49].

The experimental profiles are generated by summing the counts from the streak camera images in the transverse extent of $\sigma_{r,\mathrm{screen}} = \pm 0.536$ mm. I obtain this value by performing a Gaussian fit to the part of the bunch ahead of the ionization front ($t < 0$ ps in experimental images) and taking an average of those values. Streak camera images have a resolution of ≈ 180 μm in space and ≈ 3 ps in time.

In simulations, I produce time-resolved images by summing the charge of the macroparticles in bins with the same size as the pixels in the experimental images coming from the streak camera. Because simulations are 2D axisymmetric, I divide the counts by the volume in the cylindrical ring which corresponds to each bin. For the profiles, I then sum the densities up to $\sigma_{r,\mathrm{screen}}$. This produces images similar to those of the experiment.

I take the case of $g = 0$ %/m in Figs. 3.1(g)(h) as reference. Without a density gradient, the dephasing of the wakefields due to their v_{ph} slowdown (Eq. 3.2) leads to loss of charge of the microbunches and, thus, a short microbunch train compared to $\sigma_t = 230$ ps. I will show in the following that, consistent with the combined effect of Eqs. 3.2 and 3.3 on v_{ph}, with $g < 0$ [Figs. 3.1(a)-(f)] the microbunch trains are shorter than with $g = 0$ %/m and have less charge corresponding to a larger relative dephasing of the wakefields with respect to the microbunch train and with $g > 0$ (Fig. 3.2) the microbunch trains are longer with more charge corresponding to less relative dephasing.

Figure 3.1 shows that for $g < 0$, the density on axis along the microbunch train decreases continuously from $t = 0$ to 200 ps, after which the density remains around a constant value, which is much smaller than the first microbunch. This is in agreement with dephasing defocusing wake-

fields, which expel the charge of the microbunches, discussed in more detail in Sec. 3.4. The first microbunch is normally longer than the rest because it is always subject to dephasing focusing wakefields [50]. For the same reason, the first two or three microbunches have a larger density on axis than the bunch propagating without plasma, seen in the region $t < 0$ ps.

Figures 3.1(a)(b) show that with $g = -2$ %/m, there is a hollow region around the axis inside of the red lines for $t \approx 100$ to 200 ps, in both simulations and experiment. Thereafter, in the experiment, the density is evenly distributed and does not form microbunches. In the same region, some charge is seen in the simulations, however, observing the profile in 3.1(b), it is noted that the amount of charge there is small and does not form microbunches. As explained in Sec. 3.4, this is a result of the transverse wakefields which are quickly dephasing.

Figure 3.2 shows that with $g > 0$, the trains are longer and the microbunches have a larger density on axis than with $g \leq 0$ (Fig. 3.1). This is in agreement with wakefields with less dephasing after SM saturation, as discussed in Sec. 3.4. As with $g < 0$, the first couple of microbunches have a larger density on axis than the rest and than the bunch propagating without plasma. The microbunch train is longer in simulations than in the experiment, and the density of each microbunch is constant or decreases slowly along t, whereas the density of each microbunch in experimental images is always decreasing. This is explained if nonaxisymmetric transverse instabilities develop and lead to a reduction of charge on axis on the bunch rear. Evidence of nonaxisymmetric instabilities can be found in the small wiggles present in the tail of the microbunch train in $g > 0$, e.g., around $t = 300$ ps in Figs. 3.2(e)(g). Transverse asymmetries could also develop for $g < 0$, but in those cases the charge in the bunch rear is expelled from the axis, so that no wiggles can be seen as with $g > 0$.

Figures 3.1 and 3.2 show that the plasma density gradients have three effects on the proton density distribution. First, they change the length of the microbunch train, i.e., the number of microbunches in the train. Second, they change the density on axis and the shape of each microbunch. And last, they increase the chance of observing nonaxisymmetric effects when $g > 0$.

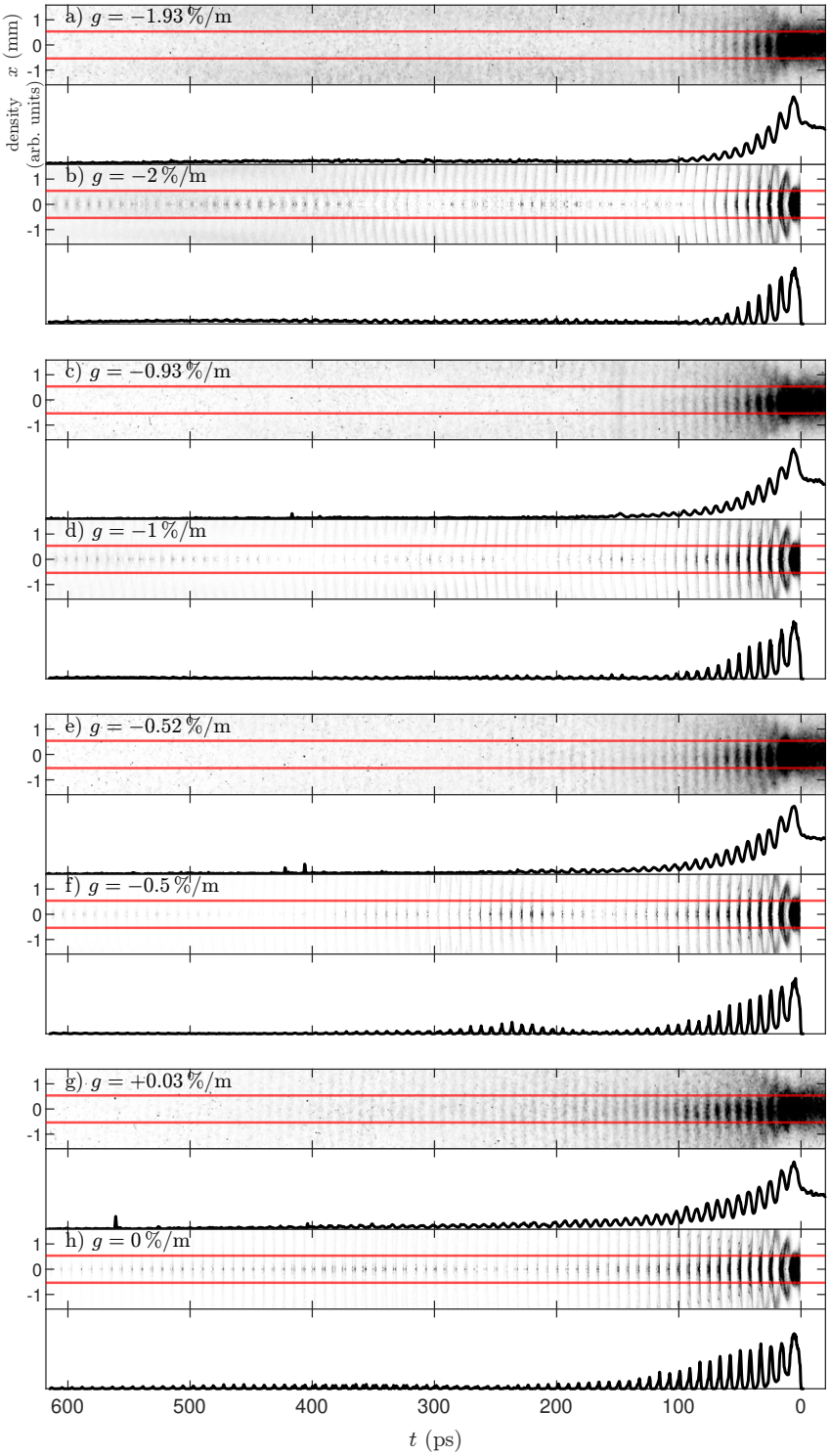

Figure 3.1: Time-resolved experimental [(a)(c)(e)(g)] and simulation [(b)(d)(f)(h)] images and profiles of the modulated bunch with various $g \leq 0$. Longitudinal profiles obtained by summing counts in the experimental images and by summing density values in simulations, within $\sigma_{r,\mathrm{screen}} = \pm 0.536\,\mathrm{mm}$ (red lines on image) of the axis. Images from simulations are mirrored about the bunch propagation axis (2D axisymmetric geometry) for a more direct comparison with experimental ones. Bunches propagating to the right.

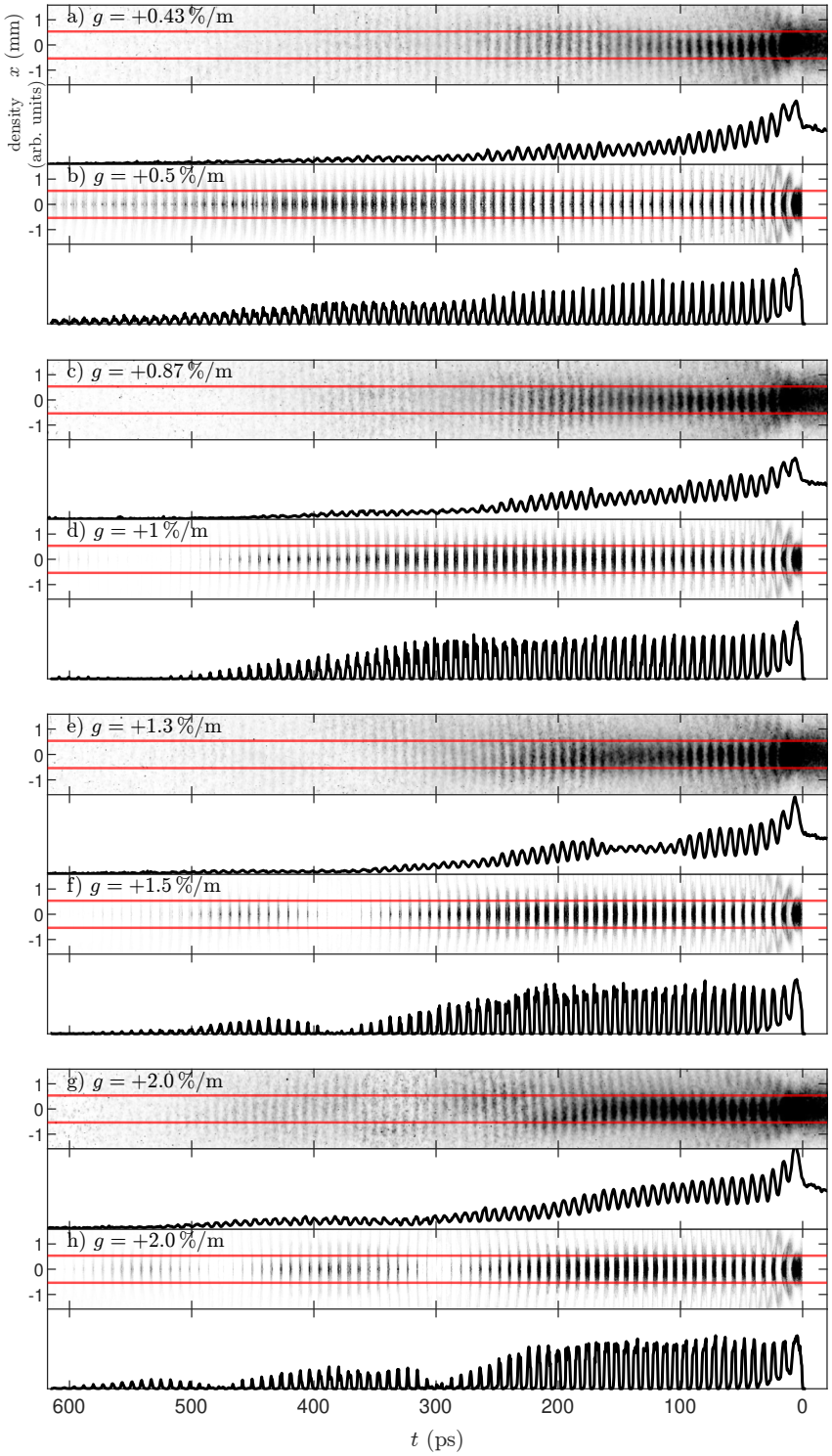

Figure 3.2: Time-resolved experimental [(a)(c)(e)(g)] and simulations [(b)(d)(f)(h)] images and profiles of the modulated bunch with various $g > 0$. Longitudinal profiles obtained by summing counts in the experimental images, or summing density values in simulations, within $\sigma_{r,\mathrm{screen}} = \pm 0.536\,\mathrm{mm}$ (red lines on image) of the axis. Images from simulations are mirrored about the bunch propagation axis (2D axisymmetric geometry) for a more direct comparison with experimental ones. Bunches propagating to the right.

3.4 Dephasing of the wakefields

The position with respect to the wakefields, shape, and charge of each microbunch determine the shape of the wakefields behind it, and the future behavior of the microbunch itself. To have a microbunch train that does not evolve (or evolves less) after the saturation of SM and that drives the highest amplitude wakefields, microbunches should remain in the focusing and decelerating phase of the wakefields. Once the charge between microbunches has left the wakefields, each microbunch can only change its position within its range in ξ at that moment. This occurs when the charge from the rear or front of each microbunch is expelled by the defocusing wakefields. Therefore, to avoid charge loss, the phase of the wakefields should remain constant after the microbunch train has been formed. Dephasing of the wakefields leads to charge loss and evolution of the microbunch train, which leads to further dephasing.

Figures 3.3, 3.4, and 3.5 show the evolution of the transverse wakefields, both along ξ and z, around three positions ξ_0 along the bunch: one close to the seeding position $\xi_0 = 1\,\mathrm{cm}$, i.e., very early in the wakefields, and then at $\xi_0 = \sigma_z$ and $\xi_0 = 2\sigma_z$, i.e., late in the wakefields. From these waterfall plots one can follow the phase of the wakefields. The plots are built by taking a lineout of the wakefields at $x = \sigma_{r0} = 0.2\,\mathrm{mm}$ and stacking them from the bottom ($z = 0\,\mathrm{m}$) to the top ($z = 10\,\mathrm{m}$). The zero-crossing of the fields is taken as the phase of the wakefields around that position in ξ. Together with the transverse wakefields, I include the position of the microbunch formed closest to each ξ_0 in each plot, marked by the green line. The opacity of the line is proportional to the peak value of the charge profile of each microbunch, calculated by integrating the density profile in $|x| < 0.2\,\mathrm{mm}$, normalized to its maximum value along z. When the line is fully transparent, the microbunch charge has been completely expelled from the region $|x| < 0.2\,\mathrm{mm}$ around the axis.

In Figs. 3.3, 3.4, and 3.5, $v_b \approx c$ is a vertical line. Zero-crossing lines with a negative slope have a subluminal v_{pb}, and lines with positive slope have a superluminal v_{pb}. When green lines are not vertical, it means that charge is being expelled from the front/back of the microbunch and brought towards the axis to the back/front by the transverse wakefields, so that the microbunch position (the position with the largest amount of charge) changes.

Figures 3.4(d)-(f) show that, as expected from Eq. 3.2, with $g = 0\,\%/\mathrm{m}$ $v_{pb} < v_b$. Then, once more, as expected from combining the effects of Eqs. 3.2 and 3.3 on v_{pb}, the behavior of the phase of the wakefields is asymmetric for positive and negative gradients, i.e., cases with negative gradients have a large phase slippage that leads to charge loss and shorter microbunch trains and cases with positive ones have a constant phase that leads to charge conservation and longer microbunch trains. Even though the difference in dephasing is small within each subfigure, as the lines appear to be parallel, in Figs. 3.3, 3.4, and 3.5, by looking at the different ξ_0, the ξ dependence of Eqs. 3.2

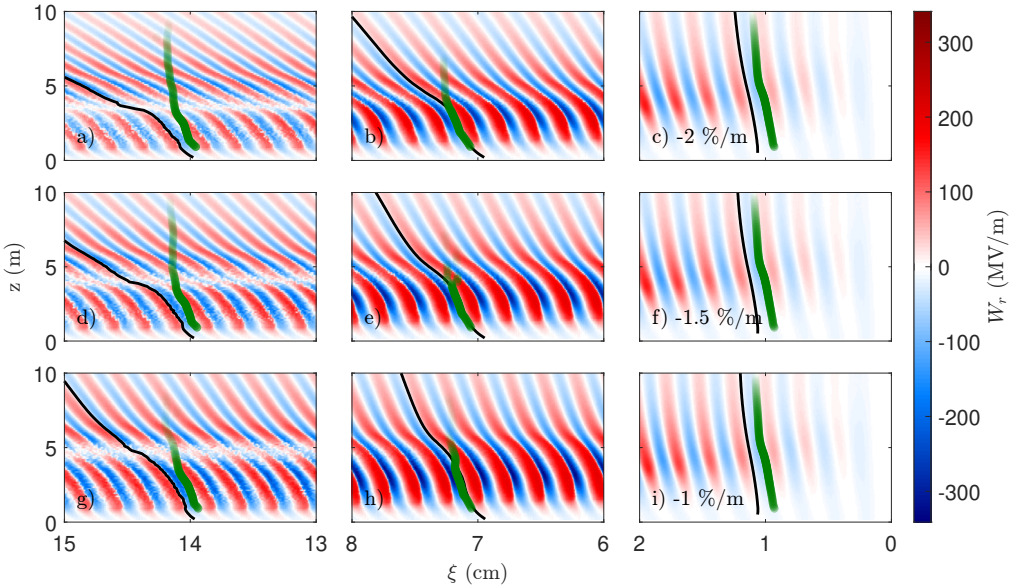

Figure 3.3: Waterfall plots of W_r evaluated at $r = 0.2\,\text{mm}$ around $\xi_0 = 1, 7$, and $14\,\text{cm}$ for $g = -2\,\%/\text{m}$ (a)-(c), $g = -1.5\,\%/\text{m}$ (d)-(f), and $g = -1\,\%/\text{m}$ (g)-(i). Black lines are the zero-crossing of the fields starting closest to each ξ_0. Green lines are located at the position of the peak of the charge profile of the microbunch formed closest to each ξ_0. The opacity of the green line corresponds to the value of the peak, normalized to its maximum value along z.

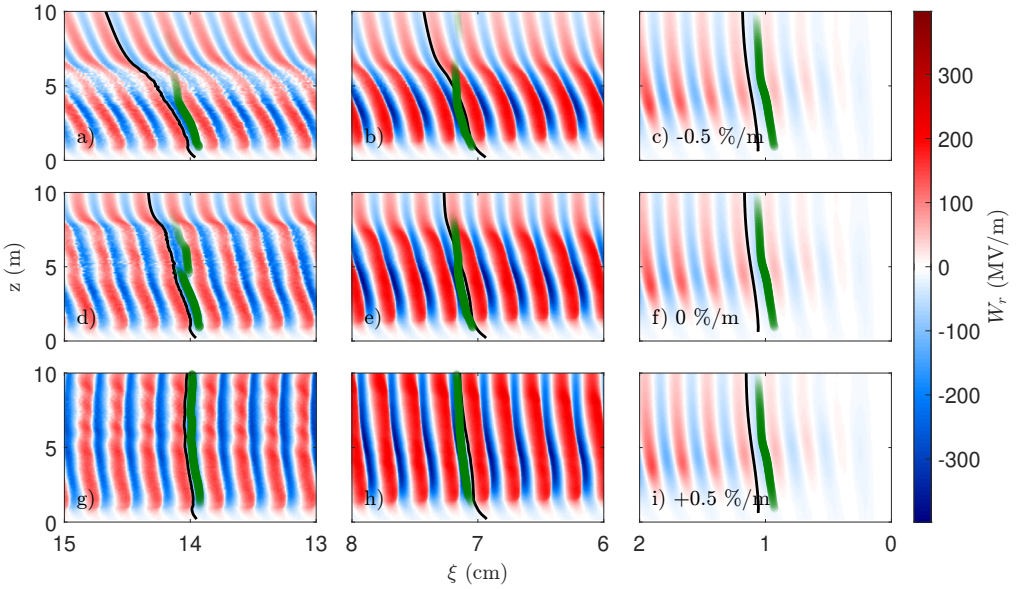

Figure 3.4: Waterfall plots of W_r evaluated at $r = 0.2\,\text{mm}$ around $\xi_0 = 1, 7$, and $14\,\text{cm}$ for $g = -0.5\,\%/\text{m}$ (a)-(c), $g = 0\,\%/\text{m}$ (d)-(f), and $g = +0.5\,\%/\text{m}$ (g)-(i). Black lines are the zero-crossing of the fields starting closest to each ξ_0. Green lines are located at the position of the peak of the charge profile of the microbunch formed closest to each ξ_0. The opacity of the green line corresponds to the value of the peak, normalized to its maximum value along z.

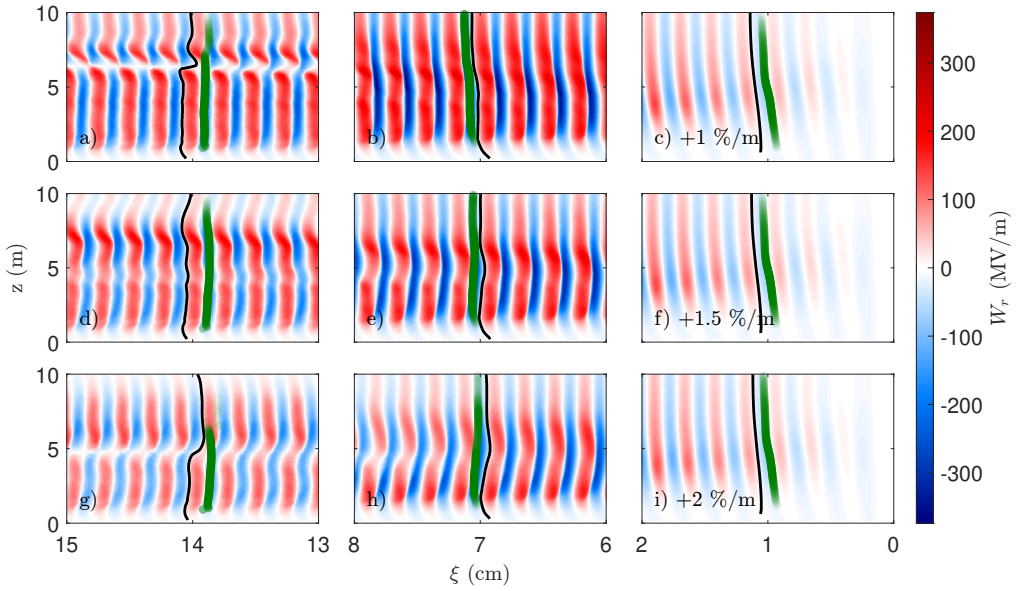

Figure 3.5: Waterfall plots of W_r evaluated at $r = 0.2\,\text{mm}$ around $\xi_0 = 1, 7$, and 14 cm for $g = +1\,\%/\text{m}$ (a)-(c), $g = +1.5\,\%/\text{m}$ (d)-(f), and $g = +2\,\%/\text{m}$ (g)-(i). Black lines are the zero-crossing of the fields starting closest to each ξ_0. Green lines are located at the position of the peak of the charge profile of the microbunch formed closest to each ξ_0. The opacity of the green line corresponds to the value of the peak, normalized to its maximum value along z.

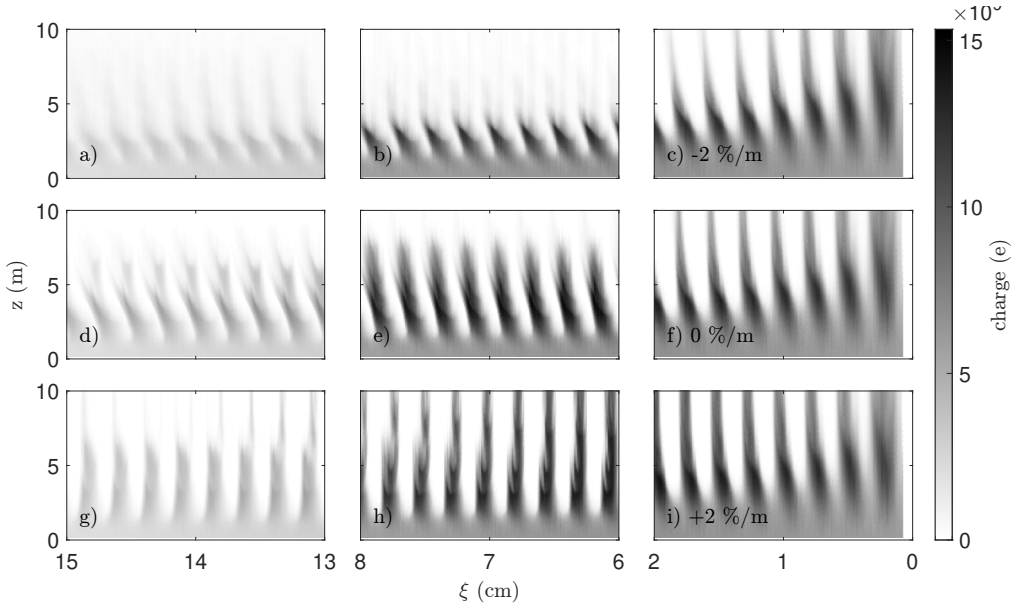

Figure 3.6: Waterfall plots of the microbunch train by integrating its density in $|x| < 0.2\,\text{mm}$ around $\xi_0 = 1, 7$, and 14 cm for $g = -2\,\%/\text{m}$ (a)-(c), $g = 0\,\%/\text{m}$ (d)-(f), and $g = +2\,\%/\text{m}$ (g)-(i).

and 3.3 is clear: the phase slippage is larger in the bunch rear than in the front. Furthermore, looking at the intensity of the wakefields color, the amplitude is larger at the middle and back than at the front of the bunch, as usual in SM.

The wakefields around $\xi_0 = 1\,\text{cm}$ [Figs. 3.3(c)(f)(i), 3.4(c)(f)(i), and 3.5(c)(f)(i)] behave similarly with all g values, since the effects of both dephasing caused by Eq. 3.2 and by the density gradients are $\propto \xi$ and, thus, small compared to later along the bunch. The expected maximum difference in ξ-position at the plasma end for the same phase among the gradients is

$$\Delta\xi = \phi c/\omega_p\left(1/\sqrt{1+g_p z/100} - 1/\sqrt{1+g_m z/100}\right), \tag{3.5}$$

where ϕ is the phase, g_p the largest positive gradient and g_m the largest negative gradient. For ϕ closest to $\xi_0 = 1\,\text{cm}$, $\Delta\xi = 0.18\,\text{cm}$. In simulations, $\Delta\xi_{\text{sim}} = 0.12\,\text{cm}$. This is in agreement with Subsec. 3.5.2, where simulations show that while with $g \leq 0$ the wakefields frequency is equal to f_{pe}, with $g > 0$ it is lower.

The zero-crossing lines at $\xi_0 = 1\,\text{cm}$ show the increase of v_{ph} as a function of g. This line starts with the largest negative slope with $g = -2\,\%/\text{m}$, which becomes less negative as g increases (without becoming positive). This is in agreement with the decrease of $\lambda_{pe} \propto n_{pe}^{-1/2}$ due to the increasing $n_{pe}(z,g)$.

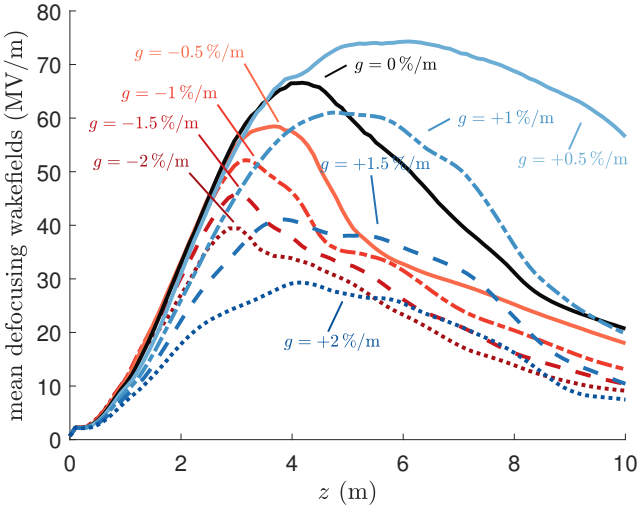

Figure 3.7: Mean amplitude of the defocusing wakefields, averaged over the whole simulation window, along z for various g values, from simulation results. I previously published this figure in [49].

An example of how a microbunch can be displaced as long as there is proton charge within the wakefields among microbunches can be seen in Fig. 3.3(b), for $g = -2\,\%/\text{m}$ at $\xi_0 = 7\,\text{cm}$. There, the microbunch charge line has a negative slope following the focusing wakefields until $z \approx 3\,\text{m}$, where the SM saturates. The saturation point is considered as the maximum value of the mean defocusing fields along z (Fig. 3.7). Afterwards, the microbunches have formed and there is not enough charge that can be brought back to axis. This is seen as the microbunch line becoming

vertical. Since the wakefields continue to dephase with respect to the bunch, the microbunch loses charge and the line becomes increasingly transparent, until it disappears at $z \approx 7.5\,\mathrm{m}$. A similar effect occurs at $\xi_0 = 7\,\mathrm{cm}$ for $g \leq 0$ [Figs. 3.3(b)(e)(h) and 3.4(b)(e)], with the difference that the bunch is completely expelled at an increasingly larger z as $|g|$ and, thus, the phase slippage, decreases. In general, the dephasing of the wakefields explains how microbunch trains with $g \leq 0$ become shorter.

For $g > 0$ at $\xi_0 = 7\,\mathrm{cm}$ [Fig. 3.4(h) and Figs. 3.5(b)(e)(h)], the microbunch remains in the focusing wakefields for all z. The vertical lines are a result of the positive contribution to v_{ph} given by the gradient and the negative one coming from Eq. 3.2. Due to less dephasing of the wakefields, especially after SM saturation, microbunches remain on axis, as is seen with the fact that all green lines reach $z = 10\,\mathrm{m}$. This explains how microbunch trains with $g > 0$ remain long. Nevertheless, an overcompensation can occur, e.g., at $g = +2\,\%/\mathrm{m}$ and $\xi_0 = 14\,\mathrm{cm}$, $v_{ph} > c$ and the microbunch at that position is expelled from the wakefields.

Equations 3.2 and 3.3 show that v_{ph} increase with ξ, so that the dephasing is seen at $\xi_0 = 14\,\mathrm{cm}$ [Figs. 3.3(a)(d)(g), 3.4(a)(d)(g), and 3.5(a)(d)(g)]. The negative slope for $g = -2\,\%/\mathrm{m}$ and $g = -1.5\,\%/\mathrm{m}$ is so large that the microbunch goes through several regions of focusing and defocusing wakefields as it propagates in the plasma. This, together with the low amplitude of the wakefields, leads to a slow expulsion the microbunch charge. Other $g < 0$ values lead to higher wakefields amplitude (Fig. 3.7), which expel the microbunches earlier in z.

The waterfall plots of the microbunch train in Fig. 3.6 give a more detailed look into the microbunch train evolution for different gradient cases: the most negative one, zero, and the most positive one. The properties shown in Figs. 3.3, 3.4, and 3.5 are also found in Fig. 3.6. At the bunch front, $\xi_0 = 1\,\mathrm{cm}$, shown in Figs. 3.6(c)(f)(i), the distance between microbunches is the largest with $g = -2\,\%/\mathrm{m}$ and the shortest with $g = +2\,\%/\mathrm{m}$, in agreement with the larger phase slippage and lower frequency (explained later in Subsec. 3.5.2) with $g < 0$ than with $g > 0$. The low amplitude of the wakefields allows for the displacement of the microbunches. The progressive increase of the distance among microbunches from positive to negative gradients can be seen in Figs. B.1, B.2, and B.2 in Appendix B.

In the middle of the bunch at $\xi_0 = 7\,\mathrm{cm}$, shown in Figs. 3.6(b)(e)(h), with $g = -2\,\%/\mathrm{m}$, the dephasing wakefields expel the microbunch charge the earliest along the plasma. The microbunch charge remains in the wakefields by the end of the plasma only with $g = +2\,\%/\mathrm{m}$, as a result of the constant phase of the wakefields in that case. Figures B.1, B.2, and B.2 in Appendix B show how the charge of the microbunches is lost at progressively larger distances along the plasma as the gradient goes from negative to positive. At the bunch rear, shown in Figs. 3.6(a)(d)(g), charge loss is due to dephasing in $g \leq 0$ and to overcompensation in $g = +2\,\%/\mathrm{m}$.

These results are consistent with the microbunch trains in Figs 3.1 and 3.2 and with Eq. 3.2. The charge in the microbunches is in general lost when there is dephasing of the wakefields with respect to the microbunch train and preserved on axis when the relative phase of the wakefields is constant. A more accurate explanation is obtained by considering the amplitude of the transverse wakefields: a higher amplitude of dephasing wakefields expels the charge more quickly. A modest positive gradient leads to the phase that changes the least and trains with more charge per microbunch. It also leads to the highest amplitude wakefields (Fig. 3.7). The discussion in this chapter complements and is in agreement with my previous publications [49, 91]. As additional information, Figs. 3.3, 3.4, and 3.5 are an alternative display of the information in Fig. 5 of Ref. [49] (also found in Fig. B.4 in Appendix B) and compliments Fig. 5 in [91] that shows the longitudinal wakefields (also found in Fig. B.5 in Appendix B).

3.5 Modulation frequency of the proton bunch

3.5.1 Modulation frequency vs transverse distance from the axis

Previously, it was demonstrated that after 10 m of propagation in a constant-density plasma, the microbunch train $f_{\mathrm{mod}} \approx f_{pe}$ [63]. In those experiments, the plasma density values covered a range of one order of magnitude. When applying the plasma density gradient, f_{mod} lies between the $f_{pe}(z = 0\,\mathrm{m})$ and $f_{pe}(z = 10\,\mathrm{m})$ [48]. The charge distribution of each microbunch has a curved shape in the transverse direction as can be seen in Figs. 3.1 and 3.2 near the seeding position. The transition from a C-shape in $g < 0$ to an l-shape and finally even a D-shape in $g > 0$ is clearly visible in the simulation images shown in the insets of Fig. 3.8. Considering that the modulation starts at the seeding position in ξ for all x, a curvature in the density distribution could indicate a change in f_{mod} along x. When using a plasma gradient, $f_{pe}(z)$ varies along the plasma. The expectation is that the proton distribution expelled out of the wakefields early along the plasma when the SM develops carries with it the f_{mod} corresponding to $f_{pe}(z \approx 0\,\mathrm{m})$. This distribution might appear at a larger distance from the axis on time-resolved images.

The test this hypothesis and further study the frequency evolution of the modulated bunch, I perform a DFT analysis on time-resolved images of the microbunch train from simulations and experiment. Experimental images are measured after 10 m of propagation in plasma and 3.5 m in vacuum, therefore, the simulation macroparticles are propagated in the same manner to do the comparison. I study the relation of f_{mod} with x by calculating f_{mod} in slices with a width equal to c/ω_{pe} for all g. In experimental images I sum the counts within the slice in the time-resolved images. In simulations, when I compare experimental and simulation results, I create the density profile as described previously in Sec. 3.3 and sum the density in each slice. When studying only simulation results I sum the density values of the proton bunch given by OSIRIS. The window for

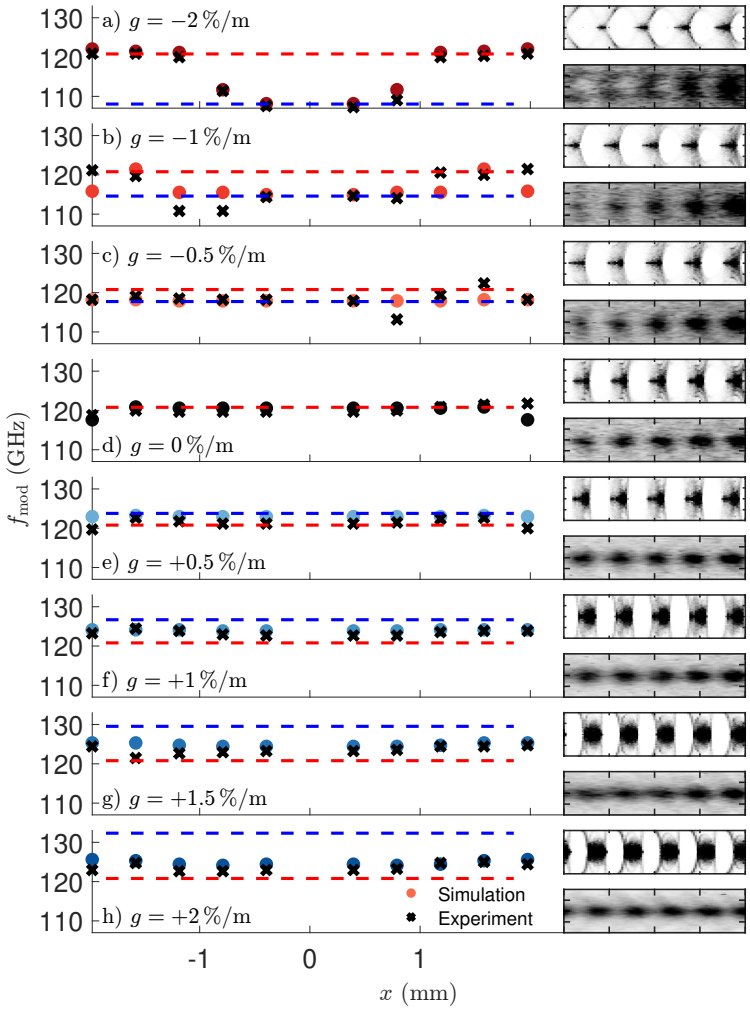

Figure 3.8: Modulation frequency f_{mod} in c/ω_{pe} = 0.395 mm-wide slices along the transverse direction of the bunch for various g values. Simulations results (dots) are mirrored around x = 0 mm to compare to both sides of the experimental (crosses) images. Red dashed lines: $f_{pe}(z = 0\,\mathrm{m})$. Blue dashed line: $f_{pe}(z = 10\,\mathrm{m})$. Insets: time resolved images for the bunch from simulations (top) and experiment (bottom) in a 40-ps range.

the DFT starts 12.5 ps behind the seeding position to exclude the first bunch, which is longer than the rest [50], and extends to $2\,\sigma_t$. The DFT is performed with 0.3 GHz spacing. This frequency step corresponds to the accuracy of plasma density measurements [84]. I take the frequency at the highest peak in the power spectrum as f_{mod}.

Figure 3.8(d) shows the case with $g = 0\,\%/\mathrm{m}$, in which all experimental (crosses) and simulation (dots) values of $f_{\mathrm{mod}} \approx f_{pe}$ (red dotted line). Figures 3.8(a)(b) shows that with $g = -2\,\%/\mathrm{m}$ and $g = -1\,\%/\mathrm{m}$, $f_{\mathrm{mod}} \approx f_{pe}(z = 10\,\mathrm{m})$ (blue dotted line) in the slice closest the axis increases as a function of x and reaches $f_{pe}(z = 0\,\mathrm{m})$ at $x > 1\,\mathrm{mm}$. For $g > 0$, Figs. 3.8(e)-(h), f_{mod} remains within $f_{pe}(z = 10\,\mathrm{m})$ and $f_{pe}(z = 0\,\mathrm{m})$, being closer to the latter, and changing less along x compared to $g < 0$. In general, as g increases, f_{mod} also increases.

The difference in behavior between positive and negative g, i.e., f_{mod} changes more along x with $g < 0$ while it remains relatively constant with $g > 0$, is explained by the fact that with $g < 0$ the dephasing occurring during SM growth and after saturation is enhanced, so that charge from microbunches is being continually expelled from the wakefields as the bunch propagates, carrying the local frequency information with it. The frequency measured closest to the axis with $g < 0$ corresponds to that from the first few microbunches that remain on the train (Fig. 3.1).

On the other hand, with $g > 0$ the dephasing occuring during SM is counteracted, making the phase closer to being constant along z [Figs. 3.4(g)(h)(i), 3.5, and 3.6(g)(h)(i)]. The relative phase of the wakefields being constant has several consequences: λ_{pe} and f_{pe} are also constant, microbunch charge is expelled at a slower rate than $g < 0$ (Fig. 3.9), and trains are longer (Fig. 3.2). Once the microbunch train is formed (after saturation), f_{mod} cannot change easily for $g > 0$ since most of the charge between microbunches has been expelled from the wakefields, which limits the microbunch position shift to the ξ-ranges in which each microbunch was when SM reached saturation.

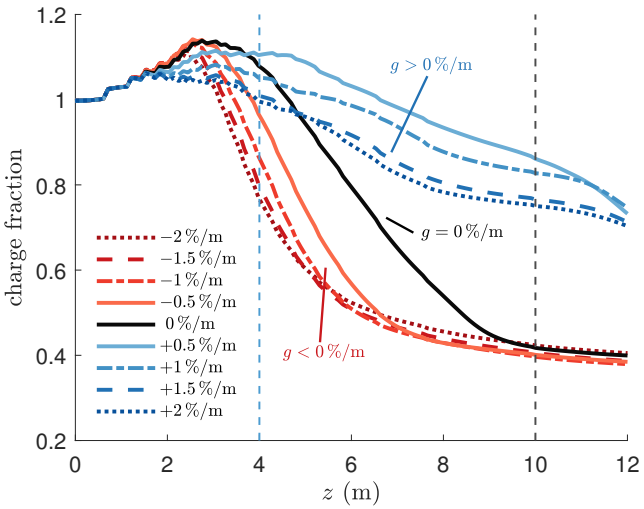

Figure 3.9: Proton bunch charge fraction in $|x| < \sigma_r(z)$, for various g values, calculated from simulation results. Black dashed line: position of plasma end. Blue dashed line: position of the peak in the mean defocusing wakefields for $g = 0\,\%/\mathrm{m}$ (see Fig. 3.7).

There is a good agreement between simulation and experimental trends and values. The difference in frequencies along x for $g < 0$ explains the C-shape of the microbunches as seen from the corresponding pictures of the microbunches shown on the side of Fig. 3.8 and agrees with the hypothesis that charge found at larger x left the wakefields earlier along z. Proton macroparticle trajectories confirm this (Fig. 3.10). In some single slices, f_{mod} measurements differ between the simulation and experiment, which can be explained by transverse asymmetries in the microbunch train in the experiment [e.g., seen around $t = 300$ ps in Figs. 3.2(e)(g)], by variations among events, and by the fact that the g in experiment is slightly different than the one used in simulations.

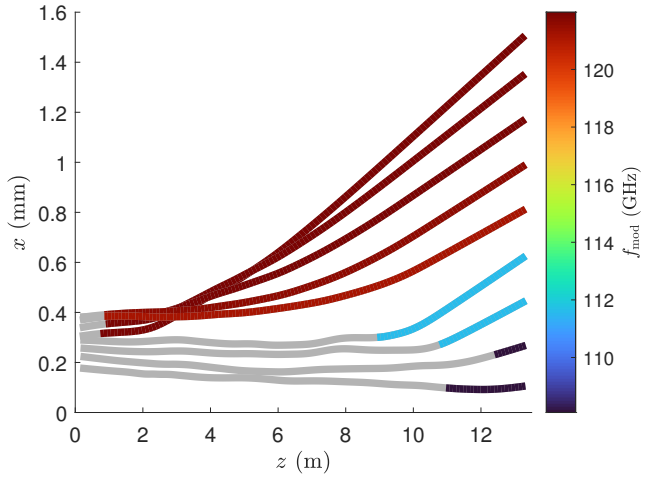

Figure 3.10: Mean radial position along the plasma and up to the screen position of simulation macroparticles that reach the screen position in 180 µm-wide slices for $g = -2$ %/m. Lines are colored once the f_{mod} of the distribution along the plasma matches the f_{mod} measured at $z = 13.5$ m.

3.5.2 Modulation and wakefields frequency vs propagation distance

I explore the relation between the on-axis ($|x| \leq 0.2$ mm) f_{mod} and the on-axis ($x = 10$ µm, to avoid noisy data at $x = 0$ µm) frequency of the wakefields f_s following their evolution along the plasma and for f_{mod} up to the screen position $z = 13.5$ m. I also explore the difference in the frequency evolution for various g.

In Fig. 3.11, both f_{mod} and f_s start at $1.016\, f_{pe}(z = 0\,\mathrm{m})$. As already discussed in chapter 2, this is due to the charge neutralization of the proton bunch by the plasma electrons, increasing the local plasma density on axis. The oscillation frequency of the plasma electrons can be approximated by $\omega_{pe}(n_b) = \sqrt{\frac{(n_{pe}+n_b)e^2}{m_e\epsilon_0}}$, which means $\frac{f_{pe}(n_b)}{f_{pe}(z=0\,\mathrm{m})} = 1.0187$ for $n_b/n_{pe} = 0.0377$, close to the measured value.

With all g, f_s (circles) changes earlier than f_{mod} (squares), approaching the value of f_{pe} (continuous line). The heavy protons move transversely more slowly than light plasma electrons, so f_{mod} adapts several meters after the change in f_s.

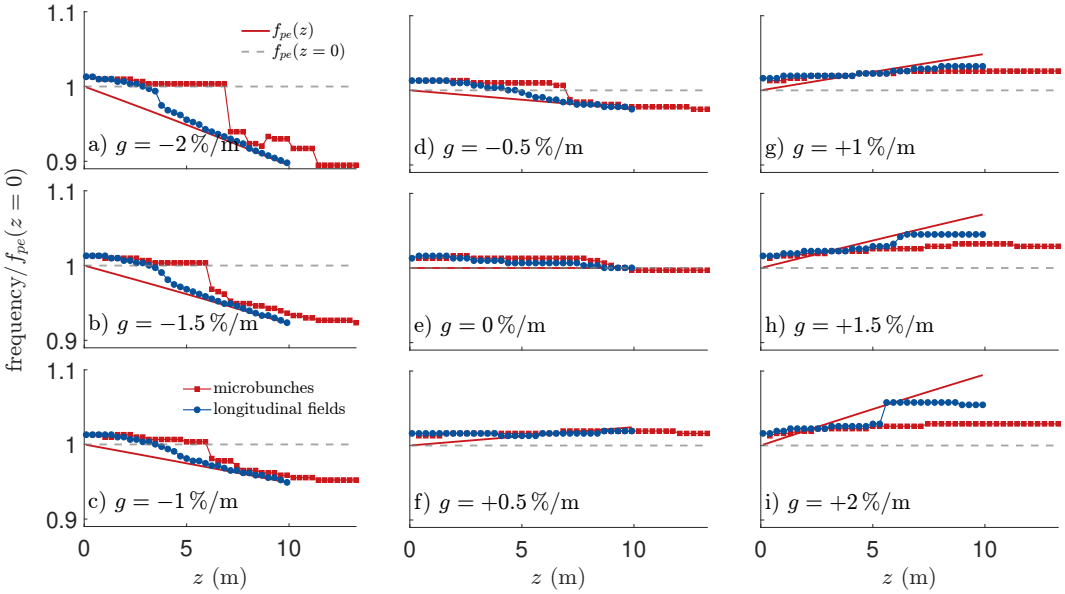

Figure 3.11: On-axis ($|x| \leq 0.2\,\mathrm{mm}$) proton bunch modulation frequency f_{mod} (squares) and on-axis ($x = 10\,\mu\mathrm{m}$) frequency of the wakefields f_s (circles) as a function of z for various g, from simulations, calculated as the peak of the DFT power spectrum.

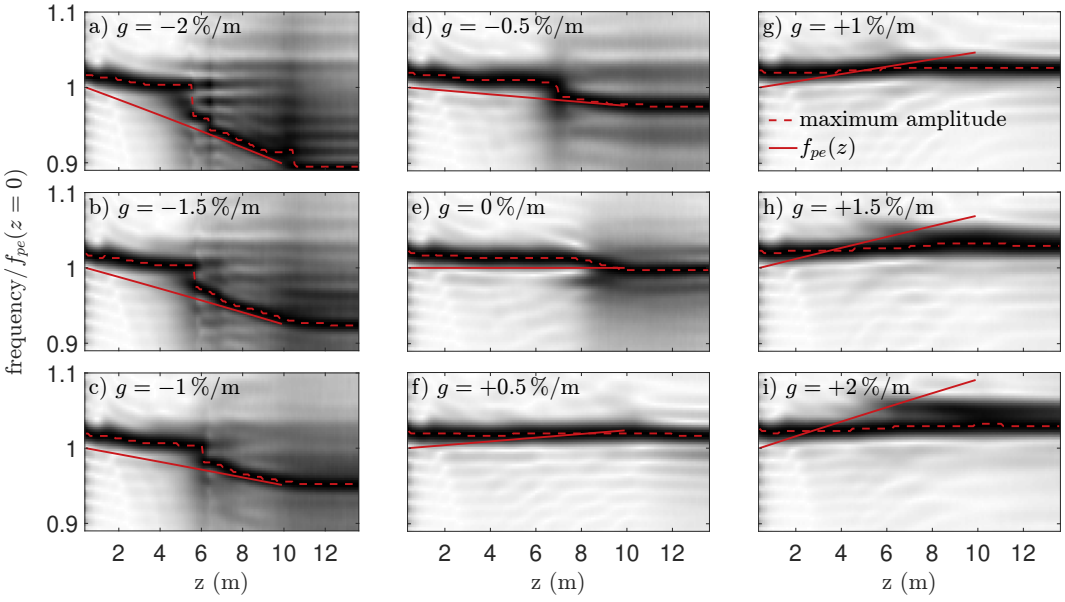

Figure 3.12: Waterfall plots of the modulated bunch DFT power spectrum along z for various g, from simulations. Spectra normalized to their maximum at each z. The dashed line is the same as the squares in Fig. 3.11. The period signal starting at $z \approx 0\,\mathrm{m}$ shows the artifact of the DFT caused by the finite time window.

With $g = 0\,\%/\mathrm{m}$ [Fig. 3.11(e)], both f_{mod} and f_s decrease smoothly (with no "jump") from the initial value to f_{pe}. It is interesting to note that the frequency value measured in [63] is reached only near the plasma end.

With $g < 0$ [Figs. 3.11(a)-(d)], f_s follows $f_{pe}(z)$ after $z \approx 6\,\mathrm{m}$. Looking at the microbunch in the case of $\xi_0 = 7\,\mathrm{cm}$ in Figs. 3.3(b)(e)(h) and 3.4(b), this is the approximate z at which the microbunch charge is lost, thus, only the microbunches at the front remain. When the modulated charge distribution leaves the transverse range used for the DFT, a "jump" in f_{mod} occurs somewhere in the range $z = 6$ to $7\,\mathrm{m}$. A decreasing f_s corresponding to an increasing λ_{pe}, which comes from the gradient, is equivalent to a decreasing v_{ph} along ξ and z, and is the same behavior v_{ph} has in Eq. 3.2. This enhancement between both effects eventually leads to $f_s = f_{\mathrm{mod}} = f_{pe}$ for $g < 0$ at $z > 6\,\mathrm{m}$.

With $g > 0$ [Figs. 3.11 (f)-(i)], f_{mod} remains relatively constant along z when compared to $g < 0$. The relative change of f_{mod} is 1.5 %, whereas the change in density of 20 % leads to a change in f_{pe} of $\approx 10\,\%$. With $g = +0.5\,\%/\mathrm{m}$ and $g = +1\,\%/\mathrm{m}$, $f_s \approx f_{\mathrm{mod}}$ along the whole plasma. When both frequencies are the same, wakefields can be driven the most resonantly. These two g-values show the largest wakefields amplitude and lead to the largest energy gain for test electrons, as explained later in Sec. 3.6. After $z = 5\,\mathrm{m}$, f_s and f_{mod} differ with the largest gradients $g = +1.5\,\%/\mathrm{m}$ and $g = +2\,\%/\mathrm{m}$, since there is overcompensation of the effect of Eq. 3.2. Contrary to $g < 0$, an increase in f_{pe} with $g > 0$ compensates for the phase velocity slowdown of Eq. 3.2, having as a result a more constant wakefields and bunch frequency, which is in agreement with the constant relative phase of the wakefields seen in Figs. 3.4(g)(h)(i) and 3.5.

Figure 3.12 shows the modulated bunch DFT power spectra along z, which gives a deeper insight to Fig. 3.11, clarifies the "jumps" seen there, as well as shows the complex frequency evolution of microbunch trains. The power spectrum is not always comprised of a single peak, but several can be present as the modulated bunch evolves and charge leaves (and sometimes comes back to) the region around the axis ($|x| \leq 0.2\,\mathrm{mm}$) during propagation. For $g < 0$ [Figs. 3.12(a)-(d)], the lower frequency that becomes the peak after $z \approx 5$ or $6\,\mathrm{m}$ already starts to form about a meter before. After the "jump", the relative difference of amplitudes between the highest peak and the rest becomes smaller and several peaks are observed, an indication of the complex evolution of (what remains of) the microbunch train after saturation.

With $g > 0$ [Figs. 3.12(e)-(i)], the relative difference in amplitude between the highest peak and the rest remains high throughout z. The longer microbunch train in that case explains this result (Fig. 3.2). For $g = +2\,\%/\mathrm{m}$ [Fig. 3.12(i)], a secondary peak appears at $z \approx 6$ at $f_{pe}(z)$ and remains until the end of the plasma, but its amplitude is never larger than that of the peak at a lower frequency. In those cases, after saturation of SM, defocusing fields, in which f_s is slightly larger than f_{mod}, expel charge from microbunches to make the long microbunch train have a beating

pattern, Fig 3.13(b). This is in agreement with experimental results in which two frequencies were measured using a CTR spectrogram for $g = +2\,\%/\mathrm{m}$ [48].

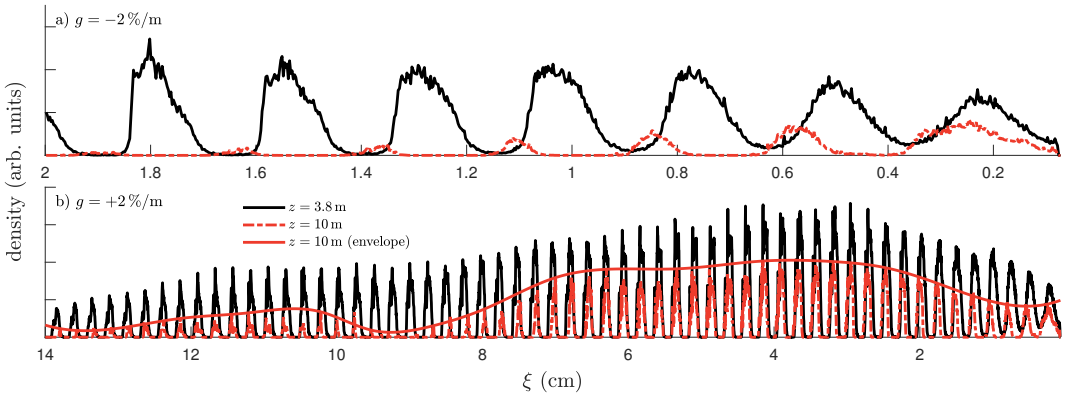

Figure 3.13: Longitudinal profile of the microbunch train within $|x| < 180\,\mu\mathrm{m}$ for (a) $g = -2\,\%/\mathrm{m}$ ($\xi < 2$ cm, close to the bunch front) and (b) $g = +2\,\%/\mathrm{m}$ ($\xi < 14$ cm) at two locations along propagation: close to saturation ($z = 3.8$ m, black line), and plasma exit ($z = 10$ m, red line), together with the envelope for $g = +2\,\%/\mathrm{m}$ (continuous red line). Figure from [49].

The streak camera images do not have sufficient resolution and signal to noise ratio to display the same complexity of the frequency spectra obtained in simulations. Even though the frequency evolution of the bunch and wakefields is complex, it is possible to extract relevant information to understand the SM process. In the experiment, measurements are done at a single position $z = 13.5\,\mathrm{m}$, and with the good agreement between simulations and experiment at that position, we can use the simulation values to confirm and explain those experimental results.

3.6 Amplitude of the wakefields and energy gain of injected electrons

The amplitude of the wakefields driven by a microbunch train depends on the relative position of the microbunches within the wakefields and on the charge of each microbunch. The amplitude of the fields is larger when the microbunch train is longer, there is more charge in each microbunch, and they are positioned in the decelerating wakefields, since they transfer more energy to the wakefields. A positive density gradient leads to longer trains with more charge per microbunch (Fig. 3.2), but as the gradient is larger, the dephasing between wakefields and microbunches increases, which can lead to microbunches in the accelerating fields, which lowers their amplitude. Therefore, there is a g value which leads to a maximum increase in amplitude and maximum energy gain of a witness electron bunch injected at a given z.

AWAKE reported in run 1 [57, 88] that the use of small positive gradients results in larger acceleration in 10 m of plasma. The electron bunches were injected at an angle into the wakefields driven by the modulated proton bunch and with a delay of 200 ps with respect to the seeding position. The electron and proton bunches cross at $z \approx 2$ m. In particular, for a plasma density $n_{pe} = 7 \times 10^{14}\text{cm}^{-3}$, $g \approx 0.2\,\%/\text{m}$ leads to more energy gain, and for $n_{pe} = 1.8 \times 10^{14}\text{cm}^{-3}$ more energy gain is achieved with $g = 0.53 \pm 0.03\,\%/\text{m}$. The latter is in agreement with simulation results that were obtained using the same $n_{pe} = 1.8 \times 10^{14}\text{cm}^{-3}$.

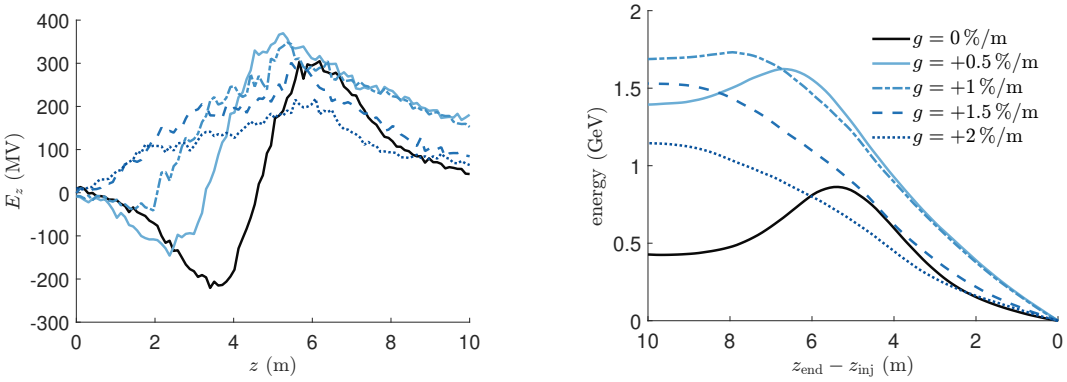

Figure 3.14: (a) Amplitude of $|E_z|$ along z at the ξ that leads to the energy gain in (b). (b) Maximum energy gain possible for an electron bunch injected at $\xi = 200 \pm 5$ ps depending on z_{inj} for all g values.

Figure 3.14(a) shows the amplitude of the accelerating wakefields with $g \geq 0$ for the ξ position of maximum energy gain. With $g < 0$, the dephasing of the wakefields hinders any significant energy gain as the electron bunch goes through accelerating and decelerating wakefields all along the plasma [as seen in Figs. 3.3 and 3.4(a)(b)(c)], and thus, I do not show those curves.

To calculate the maximum energy gain for test electrons for different injection positions z_{inj}, I sum the energy gain due to the accelerating wakefields in Fig. 3.14(a) in each time step in the simulation

$$\text{energy} = \sum E_z(\xi \approx 200\,\text{ps})\,dz \tag{3.6}$$

from $z = 10$ m to $z = 0$ m. Figure 3.14(b) shows the result of this calculation. Depending on z_{inj}, either $g = 0.5\,\%/\text{m}$ or $g = 1\,\%/\text{m}$ provides the most energy gain: when the test electrons enter the wakefields anywhere from $z = 0$ to 3 m, $g = 1\,\%/\text{m}$ leads to the highest energy gain. Afterwards, it is $g = 0.5\,\%/\text{m}$. For $g = 0\,\%/\text{m}$, the highest energy gain is achieved by injecting at $z \approx 5$ m, where the dephasing of the wakefields is small enough for the electron bunch to be in the accelerating phase of the wakefields until the plasma end (Fig. 3.4).

Charge capture for a bunch injected at an angle is a complicated process, and it has been demonstrated in simulations that electrons could oscillate near the plasma boundary and enter the wakefields at a posterior z, compared to the injection position [92]. This could explain why in the experiment the g value that leads to maximum energy gain is $g = 0.5\,\%/\mathrm{m}$ instead of $g = 1\,\%/\mathrm{m}$. The relative difference in maximum energy gain for $g = 0.5\,\%/\mathrm{m}$ and $g = 1\,\%/\mathrm{m}$ is 9 %.

The combination of a larger amplitude of the wakefields together with less dephasing leads to more energy gain. As expected, there is one optimum combination of both for one g value at one injection position (both in z and ξ), in this case either $g = 0.5\,\%/\mathrm{m}$ or $g = 1\,\%/\mathrm{m}$. Even though slightly positive gradients increase the amplitude of the wakefields and the energy gain, Fig. 3.14(a) shows that they do not stop the evolution of the microbunch train which eventually leads to a decrease in the amplitude of the wakefields.

3.7 Conclusion

The results I present show the intricate relation among the phase and amplitude of the wakefields, frequency of the modulated bunch, length of the microbunch train, and ultimately energy gain of a witness electron bunch. They also show the good agreement between simulation and experimental results, e.g., in the microbunch train profile after the end of the plasma, the modulation frequency along the transverse direction, and the energy gain of test electrons. In particular, in simulations and experimental results, with $g > 0$ the microbunch trains are longer and have more charge per microbunch, f_{mod} carries the history of the modulation along the plasma, and small positive gradients (e.g., $g = 0.5\,\%/\mathrm{m}$ for $n_{pe} = 1.81 \times 10^{14}\,\mathrm{cm}^{-3}$) leads to more energy gain of test electrons.

The length of the microbunch train and f_{mod} after the plasma is explained by the phase evolution. Consistent with a $v_{ph} < v_b$ during self-modulation growth predicted by Eq. 3.2 with $g = 0\,\%/\mathrm{m}$ and enhanced with $g < 0$, $g > 0$ decreases the dephasing by adding a positive v_{ph}, which leads to longer microbunch trains with more charge per microbunch.

In general, f_{mod} measured 3.5 m after the plasma end carries the modulation history. For $g < 0$, as charge is continually expelled from the microbunch train, the charge furthest from the axis carries f_{mod} from early along the plasma. The initial $f_{\mathrm{mod}}(z = 0\,\mathrm{m})$ is indeed $\approx f_{pe}(z = 0\,\mathrm{m})$ and $f_{\mathrm{mod}}(z = 13.5\,\mathrm{m}) = f_{pe}(z = 10\,\mathrm{m})$, indicating a large frequency evolution consistent with large dephasing. With $g > 0$, since $f_{\mathrm{mod}}(z = 0\,\mathrm{m}) > f_{pe}(z = 0\,\mathrm{m})$ and the gradients increase the wakefields frequency, f_{mod} evolves less than $g < 0$ along the plasma, reproduced in the more constant f_{mod} measured in transverse slices at $z = 13.5\,\mathrm{m}$.

The less dephasing and larger frequency resonance seen with small positive gradients leads to larger amplitude wakefields and, thus, larger energy gain for test electrons. This is observed in both experiment and simulations.

It has been shown before that plasma gradients with a limited extent have the same effect as a density step. By understanding the evolution of the system when introducing plasma density gradients and with the good agreement between simulations and experimental results, we can use simulations to propose plasma density profiles which lead to electron bunch acceleration to higher energies.

4 Self-Modulation with two Seeds: Electron Bunch and Density Cut

"With great seeding, comes great wakefields" - Unknown

4.1 Introduction

A long relativistic proton bunch propagating in plasma can undergo self-modulation (SM) [34], which transforms it into a microbunch train that resonantly drives wakefields [12] and can be used to accelerate particle bunches to high energies [57]. To produce accelerated bunches with reproducible properties, the SM must be seeded [56], so that its phase and amplitude can be repeated event by event. When there is more than one seed, two SM processes could develop simultaneously and interact. This is particularly interesting for the future of AWAKE [69], as explained in the following.

In run 2c (see chapter 1) there will be two plasmas, both 10 m long: a first one for SM and a second one for acceleration, separated by a 1 m gap where injection devices are placed. When the proton bunch is seeded with the RIF [51], the unmodulated bunch front that is ahead of the RIF propagates in neutral Rb gas and vacuum. It then reaches the pre-ionized second plasma where it can undergo self-modulation. The wakefields driven by this part of the bunch interact with the wakefields from the microbunch train. When the wakefields from both parts are out of phase and the amplitude of the wakefields from the front is high enough, the wakefields have a detrimental effect on the microbunch train. In particular, charge loss from the microbunches can occur, which lowers the amplitude of the wakefields driven by the microbunch train.

The interaction between two self-modulating parts can be replicated using only the first plasma. This occurs when the unmodulated proton bunch propagating in plasma has two seeds for SM. To study the effect that the self-modulating bunch front has on the bunch rear in a way that could also be reproduced in experiments, I use the two seeding mechanisms available in experiments: ionization front seeding [51] (replaced by a density cut in simulations [52]) and electron bunch seeding [53]. I place the electron bunch inside of the proton bunch, in contrast with the usual electron bunch seeding in which it is ahead of the proton bunch ($2.5\,\sigma_z$ in the experiment) [53].

In the linear regime, the growth of the amplitude of the transverse wakefields is given by

$$W_\perp(\xi, z) = W_{\perp,0} \exp(\Gamma(\xi, z) z), \tag{4.1}$$

where ξ is the position along the bunch, z the propagation distance in plasma, $W_{\perp,0}$ is the initial amplitude of the wakefields, and Γ is the growth rate of the modulation which depends on the proton bunch and plasma densities [13, 14]. When using two seeds, each self-modulating part has a different $W_{\perp,0}$, which, together with the ξ-dependence of the proton bunch density, leads to a different growth in each part.

For this study, I consider that the plasma density is a step function at the beginning of the plasma, i.e., there is no plasma density ramp. I use for this chapter results from the study I published previously in [93].

4.2 Simulation parameters

I study the interaction between the front and rear of the bunch using the quasi-static PIC code LCODE [47], in 2D axisymmetric geometry, with parameters based on the AWAKE baseline chosen after appropriate convergence tests (Appendix A), found in Table 4.1 for the proton bunch and plasma and in Table 4.2 for the electron bunch. The simulation parameters in this chapter are the same as the ones used in Secs. 5.3 and 5.4 in chapter 5. I use a plasma density $n_{pe} = 2{\times}10^{14}$ cm^{-3} to enable a possible comparison with the experiment.

Table 4.1: Simulation parameters based on the AWAKE baseline.

Plasma and window param.	**Phys. value**
Plasma density (n_{pe})	2×10^{14}cm^{-3}
Plasma radius	0.1 cm
Plasma length (L)	10 m
Simulation window width	0.11 cm
Transverse resolution	7.5 μm
Longitudinal resolution	0.025 ps
Time step	0.63 ps
Proton bunch param.	
RMS radius (σ_{r0})	200 μm
RMS length (σ_z)	250 ps $\cdot\, c$
Normalized emittance (ε_N)	3.6 mm mrad
Seed position (ahead of bunch center)	500 ps
Energy per proton	400 GeV
Relative energy spread	0.035 %
Population	3×10^{11} protons

Table 4.2: Simulation parameters of the seed electron bunch.

Seed bunch param.	**Phys. value**
RMS radius (σ_{r0e})	200 μm
RMS length (σ_{ze})	1 ps *cdot c*
Norm. emit. (ϵ_{Ne})	3 mm mrad
Energy	18.89 MeV
Relative energy spread	0.035 %
Population	changing

4.3 Seeding through transverse momentum modulation of the proton bunch

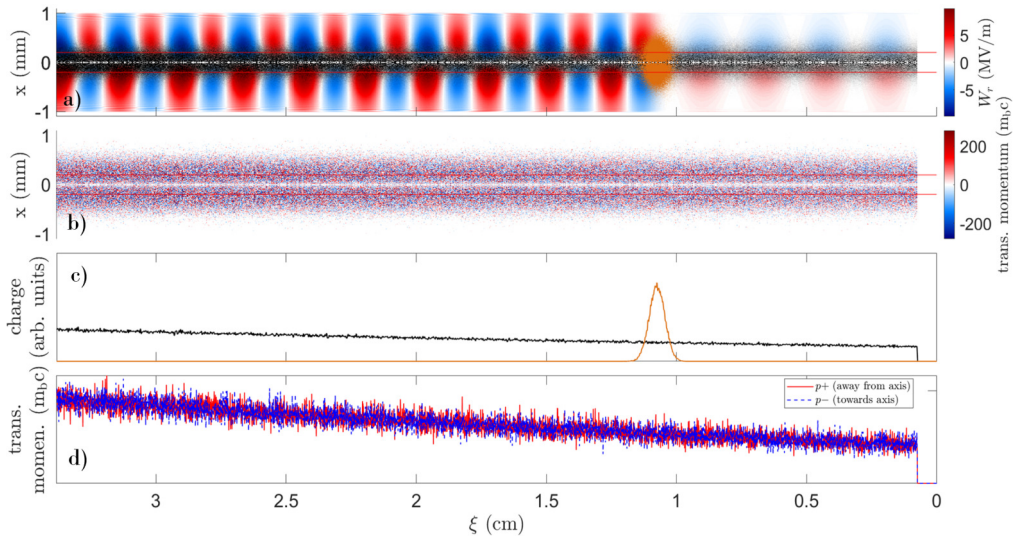

Figure 4.1: At $z = 0$ m: (a) Transverse wakefields together with proton bunch density (black) and 200 pC electron bunch density (orange). Bunches propagating to the right. (b) Transverse momentum of proton macroparticles. (c) Charge profile of the proton and electron bunches created by integrating the density within $|x| < \sigma_{r0} = 0.2$ mm [red lines in (a)]. (d) Sum of transverse momentum.

The adiabatic response of the plasma to the proton bunch leads to focusing wakefields for the protons all along the bunch, as seen in Fig. 4.1(a) in the region $\xi < 1$ cm. These wakefields are thus defocusing for electron bunches. The wakefields have a MV/m amplitude and expel a 19 MeV seed electron bunch from the plasma before $z \approx 0.6$ m, as seen in Fig. 4.2(a). At that z, the proton bunch profile is not significantly modulated, as seen in its charge profile in Fig. 4.2(c). Nevertheless, the protons have already acquired the transverse momentum that kick-start the modulation.

Figures 4.1(b)(d) show that at $z = 0$ m the transverse momentum of the protons is evenly and randomly distributed. Then, protons start acquiring transverse momentum due to the seed wakefields driven by the electron bunch that are focusing and defocusing (as opposed to the only fo-

cusing wakefields driven by the long proton bunch), as seen in Fig. 4.1(a) at $\xi > 1$ cm. Although the displacement of the protons is not yet significant by $z = 0.6$ m, Figs. 4.2(b)(d) at $\xi > 1$ cm show a periodic change in momentum, where protons are going in to and out off the axis.

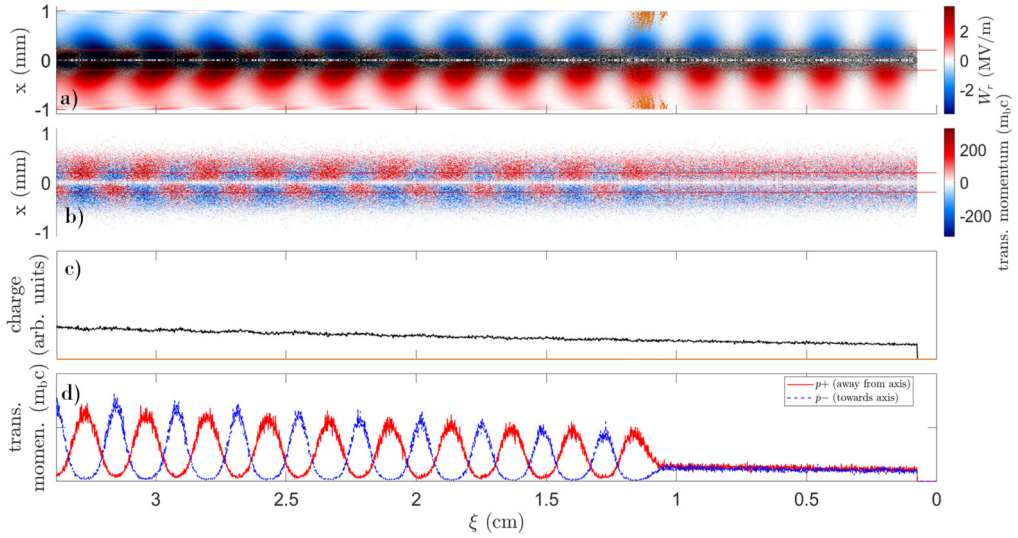

Figure 4.2: At $z = 0.6$ m: (a) Transverse wakefields together with proton bunch density (black) and 200 pC electron bunch density (orange). Bunches propagating to the right. (b) Transverse momentum of proton macroparticles. (c) Charge profile of the proton created by integrating the density within $|x| < \sigma_{r0} = 0.2$ mm [red lines in (a)]. (d) Sum of transverse momentum.

4.4 Seed electron bunch inside of proton bunch

An electron bunch with a high enough charge placed close to the density cut can seed the SM, i.e., the position of the microbunches in the train at the end of the plasma is determined by the initial position of the electron bunch. There is a charge below which the density cut, and not the electron bunch, does the seeding (in an extreme case, when the charge is reduced to 0 pC).

For the proton bunch density and density cut position in Table 4.1, a charge of 100 pC for the electron bunch is not enough to seed the wakefields. Figure 4.3 shows the initial setup of the proton and electron bunches, where the difference between Fig. 4.3(a) and (b) is the position of the seed electron bunch, which has been shifted by $\lambda_{pe}/2$, where

$$\lambda_{pe} = \sqrt{\frac{\pi}{n_{pe} r_e}}, \tag{4.2}$$

is the plasma wavelength, and r_e is the classical electron radius. This shift is also clearly seen in Fig. 4.3(c).

Figure 4.4 shows the modulated bunch at the end of the plasma at $z = 10$ m. The phase of both the modulated bunch [Fig. 4.4(c)] and the transverse wakefields [Fig. 4.4(d)] is approximately the

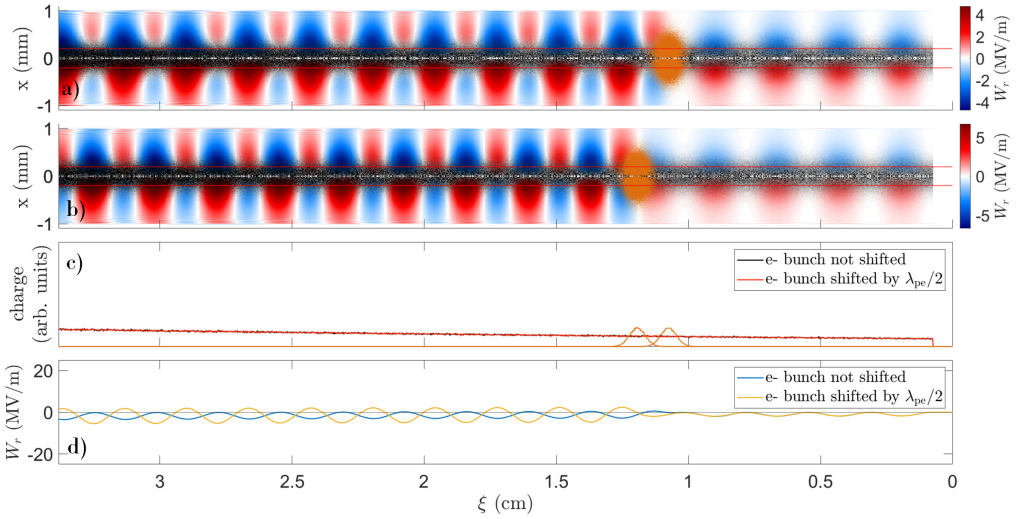

Figure 4.3: At $z = 0$ m: (a) and (b) Transverse wakefields together with proton bunch density (black) and 100 pc electron bunch density (orange). Bunches propagating to the right. (c) Charge profiles of the proton (red and black) and electron (orange) bunches by integrating the density within $|x| < \sigma_{r0} = 0.2$ mm [red lines in (a)]. (d) Lineouts of the transverse wakefields at $x = \sigma_{r0} = 0.2$ mm.

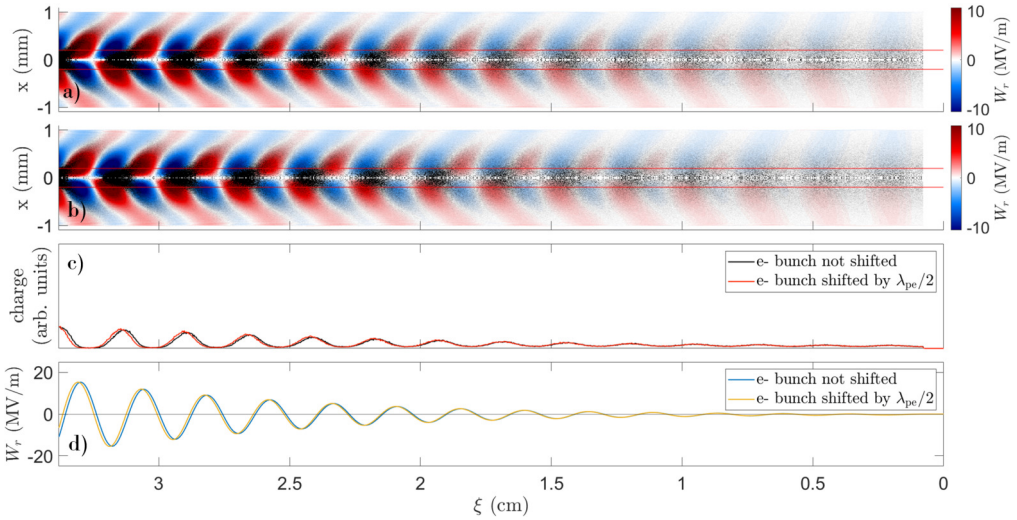

Figure 4.4: At $z = 10$ m: (a) and (b) Transverse wakefields together with proton bunch density (black), propagating to the right. (c) Charge profiles of the proton (red and black) bunches by integrating the density within $|x| < \sigma_{r0} = 0.2$ mm [red lines in (a)]. (d) Lineouts of the transverse wakefields at $x = \sigma_{r0} = 0.2$ mm.

same, which is a nice result of the seeding done by the density cut, not the electron bunch. In this case, the initial amplitude of the seed wakefields [Fig. 4.3(d) at $\xi > 1$ cm] of around 3 MV/m driven by the electron bunch was not high enough to transfer enough transverse momentum to the pro-

tons before it was expelled from the wakefields. The focusing wakefields driven by the proton bunch make the wakefields driven by the seed electron bunch asymmetric around 0 MV/m.

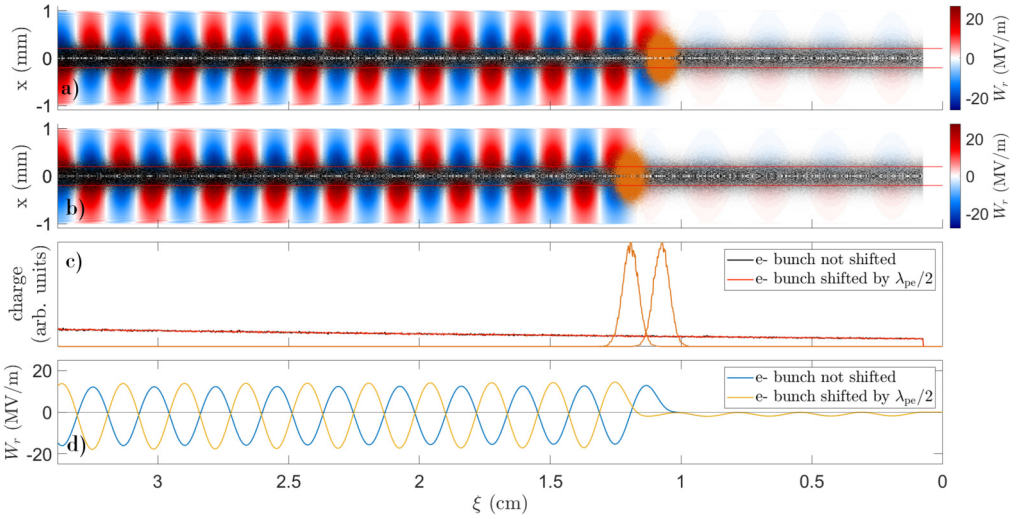

Figure 4.5: At $z = 0$ m: (a) and (b) Transverse wakefields together with proton bunch density (black) and 550 pc electron bunch density (orange). Bunches propagating to the right. (c) Charge profiles of the proton (red and black) and electron (orange) bunches by integrating the density within $|x| < \sigma_{r0} = 0.2$ mm [red lines in (a)]. (d) Lineouts of the transverse wakefields at $x = \sigma_{r0} = 0.2$ mm.

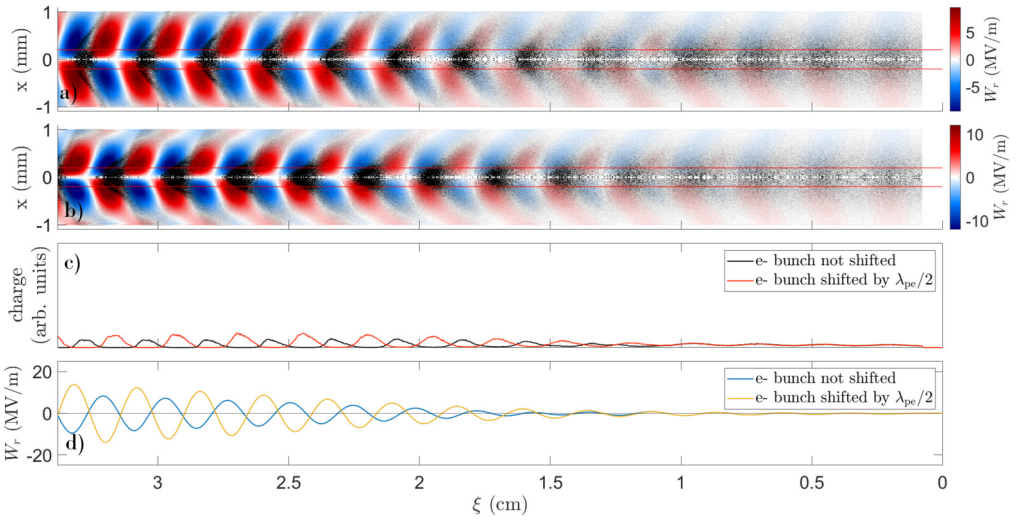

Figure 4.6: At $z = 10$ m: (a) and (b) Transverse wakefields together with proton bunch density (black), propagating to the right. (c) Charge profiles of the proton (red and black) bunches by integrating the density within $|x| < \sigma_{r0} = 0.2$ mm [red lines in (a)]. (d) Lineouts of the transverse wakefields at $x = \sigma_{r0} = 0.2$ mm.

Figure. 4.5 shows a similar initial setup to Fig. 4.3, with the difference that the electrons have a charge of 550 pC and drive seed wakefields with an amplitude of around 15 MV/m [Fig. 4.5(d)]. After propagating the bunches in the plasma, Fig. 4.6 shows that, in this case, the modulated bunch [Fig. 4.6(c)] and the transverse wakefields [Fig. 4.6(d)] have a phase shift of approximately $\lambda_{pe}/2$ between each other. The electron bunch transferred enough momentum through its wakefields to enable seeding.

4.5 Transition between seeding from density cut and electron bunch

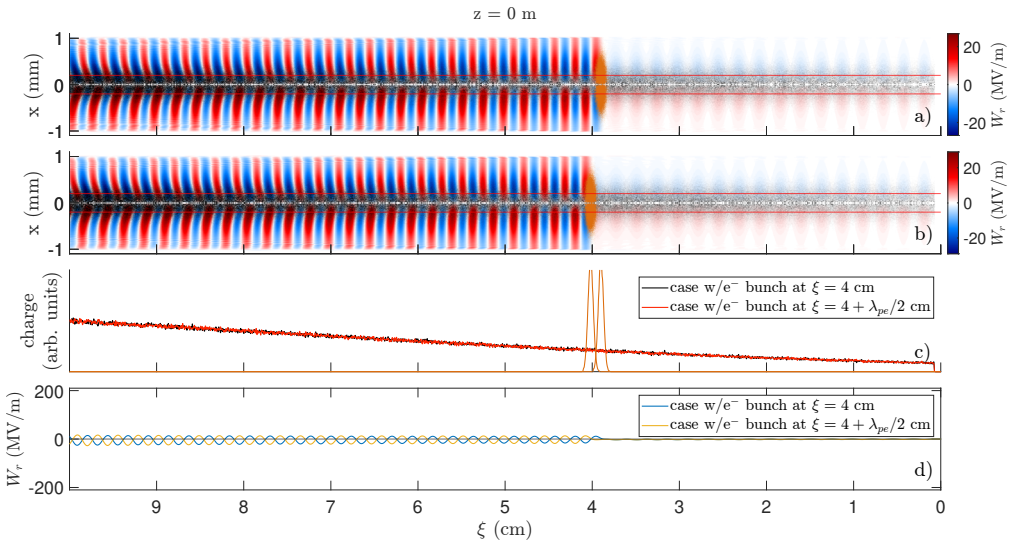

Figure 4.7: At $z = 0$ m: (a) and (b) Transverse wakefields together with proton bunch density (black) and 200 pc electron bunch density (orange). Bunches propagating to the right. (c) Charge profiles of the proton (red and black) and electron (orange) bunches by integrating the density within $|x| < \sigma_{r0} = 0.2$ mm [red lines in (a)]. (d) Lineouts of the transverse wakefields at $x = \sigma_{r0} = 0.2$ mm.

In the transition between being seeded by the electron bunch or by the density cut, changing the position of the electron bunch while maintaining the density cut position constant has interesting effects on the microbunch train, which can be used to measure the growth of SM. Figures 4.7(a)(b) show the initial transverse fields driven by the electron bunches at the beginning of the plasma, which have an amplitude of ≈ 20 MV/m, larger than the ones driven by the density cut. The seed electron bunches are placed at $\xi = 4$ and $\xi = 4 + \frac{\lambda_{pe}}{2}$ cm behind the density cut [Figs. 4.7(a)-(c)]. The wakefields they drive are therefore shifted by $\lambda_{pe}/2$ with respect to each other, as indicated by the lineouts in Fig. 4.7(d).

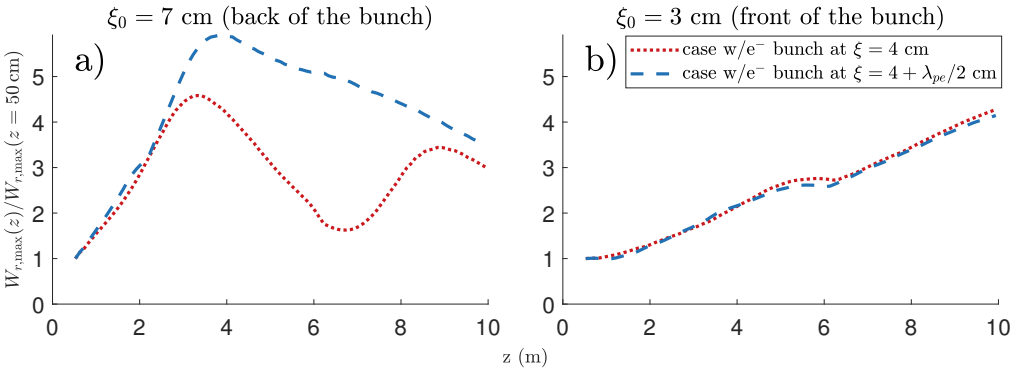

Figure 4.8: Amplitude of the wakefields in the ranges (a) $\xi_0 = 7 \pm \lambda_{pe}/2$ cm and (b) $\xi_0 = 3 \pm \lambda_{pe}/2$ cm, 3 cm behind each seed, normalized to the amplitude in the same ξ-region at $z = 50$ cm, when the seed electron bunches left the simulation window. The curves start at $z = 50$ cm to compare the SM growth excluding the fields driven by the seed electron bunch.

Figure 4.8 shows that the growth of the transverse fields is larger behind the electron bunch than behind the density cut, up to $z \approx 3.5$ m, at which point microbunches are already formed in the back of the bunch. This is due to the overall higher initial wakefields and higher proton density in the region behind the electron bunch [Fig. 4.7(c)(d)]. The larger growth leads to an earlier formation of microbunches behind the seed electron bunch whereas the bunch front is starting to modulate, but has not yet reached saturation, as observed in the growth after $z = 3$ m in Fig. 4.8(b). This difference in modulation growth is seen in Fig. 4.9(a)(c). The transverse wakefields at this z are still shifted by $\approx \lambda_{pe}/2$ and are continuously growing from front to back, as the effect from the wakefields of the bunch front is still small. The wakefields have reached an amplitude of $\approx$ 200 MV/m at the rear $\xi = 10$ cm, a consequence of SM.

In the first centimeters of propagation, the transverse fields driven by the unmodulated proton bunch are always defocusing for the electron bunch. As the electron bunch propagates, it loses energy through its own wakefields and is expelled out of the plasma at $z \approx 50$ cm. As the proton bunch continues to propagate, the modulation in the bunch front grows. The amplitude of the wakefields driven by the modulating bunch front eventually becomes large enough to start affecting the microbunch at the initial electron bunch ξ-position, which in turn affects the one behind it, and eventually the entire microbunch train. The effect on the microbunch train depends on its relative phase with respect to phase of the modulation and thus wakefields in the front. When the microbunches are in the focusing phase of the wakefields driven by the front, they continue propagating along the plasma. On the contrary, when they are in the defocusing phase, they are defocused and disappear.

At $z = 10$ m and after $\xi_0 \approx 6$ cm, the microbunches have been expelled in one case, shortening the bunch train, and remain in the other case [Figs. 4.10(a)-(c)]. This significant difference could

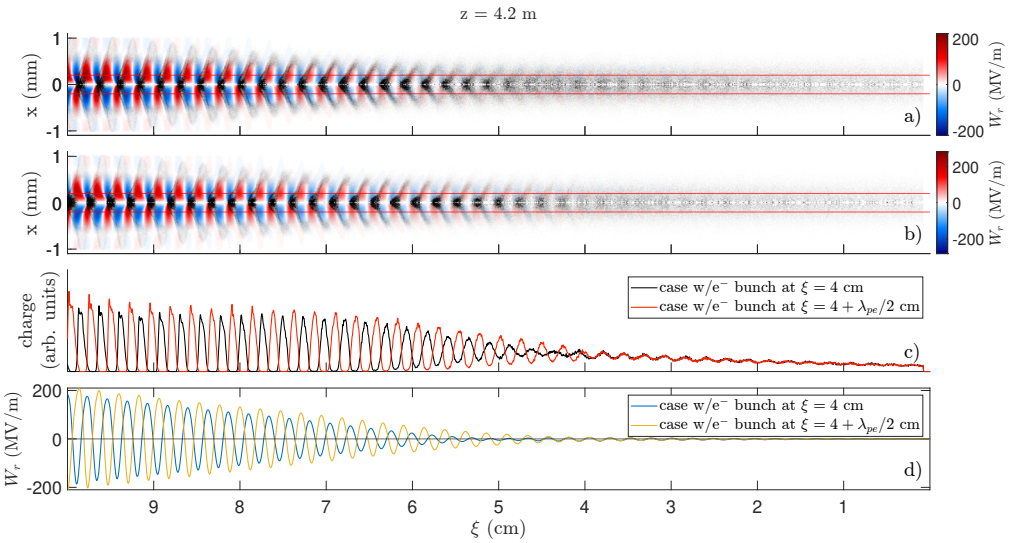

Figure 4.9: At $z = 4.2\,\mathrm{m}$: (a) and (b) Transverse wakefields together with proton bunch density (black), propagating to the right. (c) Charge profiles of the proton (red and black) bunches by integrating the density within $|x| < \sigma_{r0} = 0.2\,\mathrm{mm}$ [red lines in (a)]. (d) Lineouts of the transverse wakefields at $x = \sigma_{r0} = 0.2\,\mathrm{mm}$.

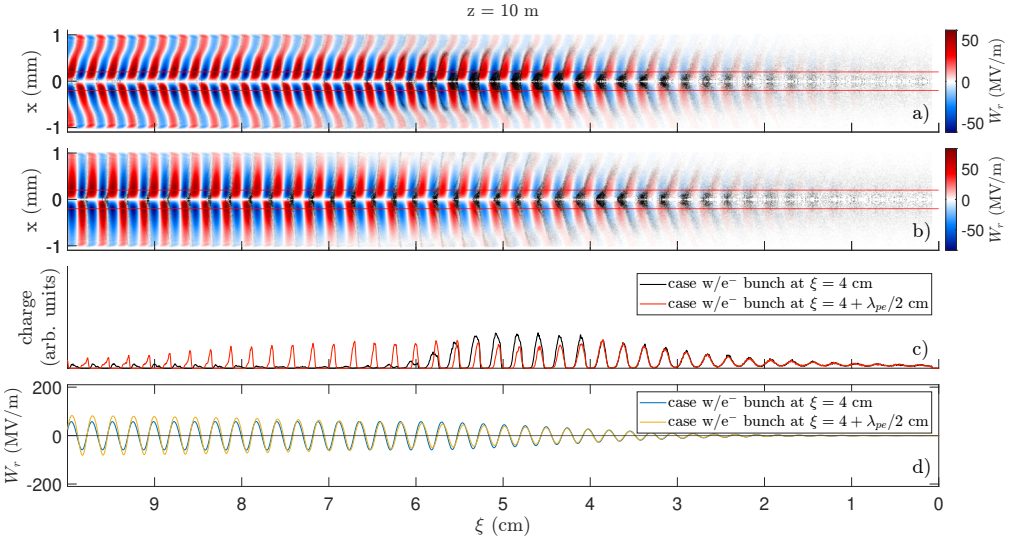

Figure 4.10: At $z = 10\,\mathrm{m}$: (a) and (b) Transverse wakefields together with proton bunch density (black), propagating to the right. (c) Charge profiles of the proton (red and black) bunches by integrating the density within $|x| < \sigma_{r0} = 0.2\,\mathrm{mm}$ [red lines in (a)]. (d) Lineouts of the transverse wakefields at $x = \sigma_{r0} = 0.2\,\mathrm{mm}$.

be measured in the experiment. Figure 4.10(a) shows the off-axis proton bunch density, that previously formed microbunches, in the defocusing wakefields. The lineout of the wakefields are in phase all along the bunch at $z = 10\,\mathrm{m}$ [Fig. 4.10(d)], after the out-of-phase microbunches have

been lost. The amplitude is also lower than in Fig. 4.9 because of the loss of charge of the microbunch train in both cases.

4.6 Conclusion

I show that self-modulation can be also seeded through a modulation in the momentum of the protons in the proton bunch. I also show that the seed electron bunch should have enough charge to drive wakefields of high enough amplitude to transfer its energy to the protons. A 100 pC, 19 MeV seed electron bunch does not seed the self-modulation, while a 550 pC, 19 MeV bunch does.

I show that when using two seeds for the self-modulation, in the transition between seeding with the electron bunch or the density cut, a shift in position of the electron bunch can lead to the defocusing of microbunches from axis, shortening the microbunch train. This occurs because, behind the electron bunch, the modulation growth is larger and the modulation saturates first, creating a microbunch train earlier in the propagation. Then the bunch front modulates and the wakefields it drives either expel microbunches from the axis or focus and maintain them until the plasma exit.

The effects shown in this chapter cannot be measured experimentally with the current setup since there is a plasma ramp, discussed in depth in the next chapter (chapter 5), leading to the long plasma in which the seed electron is expelled from the wakefields when propagating within the proton bunch. This electron bunch charge loss was measured in the experiment [94].

The results show that a self-modulating segment of the bunch can have detrimental effects in a already modulated bunch propagating behind it. To prevent any detrimental effects, a unmodulated segment of the bunch propagating in front of the microbunch train should be avoided. Nevertheless, this study was done inspired in the experimental setup of run 2a of AWAKE. To have a more complete assessment of the effects of the unmodulated segment of the bunch, simulations with the parameters of run 2c should be done. Two important differences to consider are the decreased density of the unmodulated bunch front, since it has been propagating and expanding in vacuum before reaching the second plasma, and the fact that the modulation in the bunch front would start from noise, not from a seed, which leads to a slower growth.

5 Influence of a Plasma Density Ramp on Electron Bunch Injection

"It's more important to master the cards you're holding than to complain about the ones your opponents were dealt" - Grimsley

5.1 Introduction

In a Plasma Wakefield Accelerator (PWFA) [10], when the drive bunch density n_{b0} is much smaller than the plasma density n_{pe}, the plasma has a linear response to the drive bunch. This response is a periodic modulation of the plasma electron density that sustains electric and magnetic fields with a periodicity similar to

$$\lambda_{pe} = \sqrt{\frac{\pi}{n_{pe} r_e}}, \tag{5.1}$$

where r_e is the classical electron radius. By changing the sign of the charge of the drive bunch, the perturbation shifts in phase by π, otherwise it has an identical structure.

In the opposite situation, when $n_{b0} >> n_{pe}$, the plasma has a non-linear response to the drive bunch that differs in structure for a negatively and positively charged bunch. A negatively charged bunch drives a blow-out[1] of plasma electrons [95], leaving in each period of the wakefields a region of plasma ions with transverse fields increasing linearly with radius. This regime is favorable for acceleration of a negatively charged bunch, while possibly preserving its emittance [96]. A positively charged drive bunch causes a flow-in[2] of plasma electrons towards the bunch propagation axis [97, 98], creating a high density filament, with a width much narrower than the cold plasma skin depth c/ω_{pe}, where c is the speed of light and $\omega_{pe} = \sqrt{\frac{n_{pe}e^2}{m_e \varepsilon_0}}$, where e and m_e are the electron charge and mass, respectively, and ε_0 is the permittivity of free space.

The density in the negatively charged filament can be $>> n_{pe}$ and leads to a defocusing force for negatively charged bunches. The plasma electrons forming the filament leave the axis after the bunch has passed, creating a region of partial or total depletion of plasma electrons [99].

[1] All plasma electrons leave the region around the drive bunch propagation axis, leaving a region with ions only.
[2] All plasma electrons in the region covered by the drive bunch move towards the drive bunch propagation axis.

Both regimes can occur along a plasma density ramp. Most plasma sources have a ramp at both ends. Bunches injected into the constant-density plasma must cross this ramp at low energy when entering the plasma and at high energy when exiting it. When $n_{pe} << n_{b0}$ in the constant-density plasma, this condition is also satisfied in the ramp. On the other hand, when $n_{pe} >> n_{b0}$ in the constant density plasma, a transition between non-linear and linear regimes occurs when the density at the start of the ramp $n_{pe,\text{start}} << n_{b0}$ and n_{pe} increases along its length to reach a value where $n_{pe,\text{end}} >> n_{b0}$. Plasma density ramps have been proposed as adiabatic, axially symmetric focusing devices to reduce, together with magnetic optics, the transverse size of an electron bunch to sub-micron values [96, 100, 101, 102].

The sub-micron transverse size is a requirement to match the beam rms width σ_r to the large focusing forces of the wakefields. The matching condition (see chapter 1) requires $\sigma_r^2 = \epsilon\sqrt{\gamma}c/\omega_{pe}$, where ϵ and γ are the geometric emittance and relativistic factor of the bunch, respectively. A smaller emittance requires a smaller σ_r.

There are theoretical descriptions of the transverse evolution of a bunch propagating through plasma ramps with various profiles, which may be non-adiabatic [100]. The non-adiabatic profiles achieve the goal of matching the bunch size to the plasma focusing force. A plasma ramp at the plasma exit can prevent a quick expansion of the bunch when its divergence is no longer counteracted by the focusing force in the plasma.

A ramp exists, e.g., in a windowless plasma source like the one used in AWAKE [12], which aims to use the energy of a relativistic long proton bunch, with rms length $\sigma_z >> \lambda_{pe}$, to accelerate electron or positron bunches to high energies through the scheme of self-modulation (SM) [34]. In AWAKE, a laser pulse ionizes the atoms of Rb vapor to create the plasma [103]. The Rb vapor flows to expansion volumes on both sides of the vapor source through an orifice, which has currently a radius $r_o = 5\,\text{mm}$. The laser pulse propagates and ionizes the atoms in the low-density vapor in the expansion volume.

The plasma density ramp leading to the plasma entrance used in this thesis is modelled after Refs. [60, 61] and changes along the plasma z as

$$\frac{n_{pe}(z)}{n_{pe0}} = \frac{1}{2} + \frac{z/2r_o}{2\sqrt{0.25 + \left(\frac{z}{2r_o}\right)^2}}, \tag{5.2}$$

where n_{pe0} is the density in the constant-density plasma. The ramp is shown in Fig. 5.1, normalized to n_{pe0}. Even though it appears to change rapidly from 0 to 1 around the plasma entrance ($z = 0\,\text{m}$) in linear scale, the logarithmic scale shows that there is a long, low-density ramp before the plasma entrance. At $z = -1\,\text{m}$, the density is five orders of magnitude lower than in the long plasma.

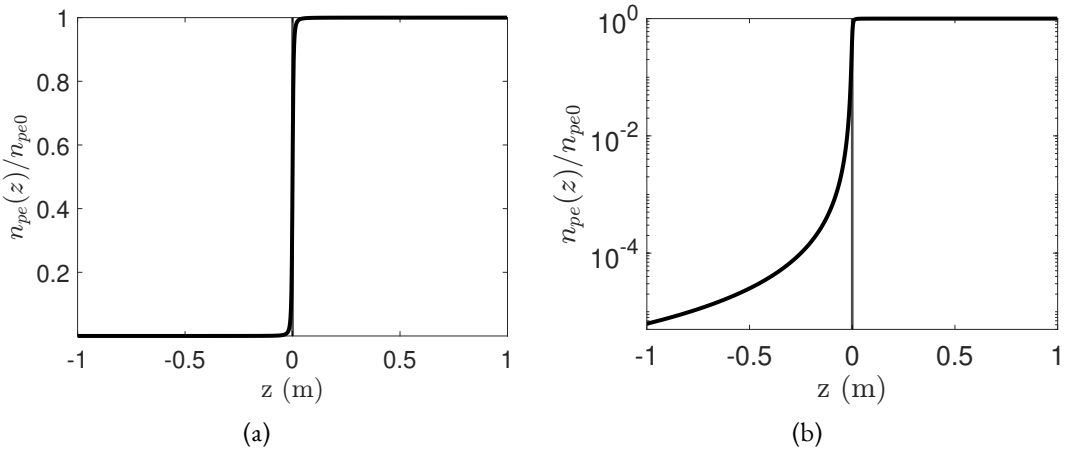

Figure 5.1: Density profile of the plasma ramp leading to the long plasma in (a) linear scale and (b) logarithmic scale. The vertical line at $z = 0$ m indicates the position of the plasma entrance, in which $n_{pe}(z) = \frac{1}{2} n_{pe0}$. A long, low-density ramp before the plasma entrance can be observed.

In the following analysis, when a plasma ramp is being considered, the plasma entrance refers to the point where $n_{pe}(z) = \frac{1}{2} n_{pe0}$, as indicated in Fig. 5.1. Otherwise, it is the point where there is a sudden onset of the plasma density.

A possible configuration of a PWFA relying on SM is to have two separate plasmas [69]: one for SM and one for acceleration, with a 1 m gap in between to set the electron bunch injection devices. In the first plasma a long proton bunch self-modulates and transforms into a microbunch train. The dephasing of the wakefields during SM growth [13, 14] leads to little energy gain or even expulsion of an electron bunch from the wakefields [48, 49] (also discussed in chapter. 3).

The bunch modulation reaches saturation in the first plasma. After saturation, the phase of the wakefields evolves much less. The modulated bunch, transformed now into a microbunch train, then propagates into the second plasma, in which the relatively constant phase of the wakefields allows for an electron bunch to be injected, gain energy, and conserve adequate properties for applications [54, 69], such as micron-level emittance and percent-level energy spread [69].

I study the effect the ramp may have on bunches injected into the plasma. Bunches may be injected for two reasons: seeding SM or to be accelerated. When injected for seeding, i.e., ahead of the proton bunch, the ramp has a focusing effect on the bunch that is not considered here. I study the case when the electron bunch is injected within the proton bunch. Using electron bunch seeded self-modulation (eSSM) [53] from within the proton bunch would enable the study of SM growing from two seeds: relativistic ionization front seeding (RIF) [51, 56, 63] and eSSM, as discussed in the previous chapter (chapter 4). I also study the effect of the ramp on an electron bunch injected within the microbunch train in the second plasma for acceleration.

5.2 Simulation parameters

Table 5.1: Simulation parameters of injected charged particle bunches.

Bunch param.	**Seed**	**Acceleration**
RMS radius (σ_{r0e})	200 µm	11.5 µm
RMS length (σ_{ze})	1 ps	0.2 ps $\cdot c$
Norm. emit. (ϵ_{Ne})	3 mm mrad	8 mm mrad
Energy	18.89 MeV	150 MeV
Relative energy spread	0.035 %	0.035 %
Population	3.43×10^9 electrons	6.24×10^8 electrons
Injection position (z_{inj})	-1 m	10.4 m

I study with PIC simulations the formation of a high-density plasma electron filament on the propagation axis of a relativistic long proton bunch travelling through a plasma ramp where $n_{pe,\text{start}}(z) << n_{b0}$ and $n_{pe,\text{end}}(z) >> n_{b0}$. I obtained all results in this chapter using the 2D axisymmetric quasi-static code LCODE [47], with parameters based on those of AWAKE.

Table 5.2: Simulation parameters of the plasma and proton bunch in the first plasma, based on the AWAKE baseline.

Plasma and window param.	**Phys. value**
Constant plasma density (n_{pe0})	$2 \times 10^{14}\text{cm}^{-3}$
Plasma radius	0.1 cm
Plasma length (L)	10 m
Simulation window width	0.11 cm
Transverse resolution	7.5 µm
Longitudinal resolution	0.025 ps
Proton bunch param.	
RMS radius (σ_{r0})	200 µm
RMS length (σ_z)	250 ps $\cdot c$
Normalized emittance (ϵ_N)	3.6 mm mrad
Seed position (ahead of bunch center)	500 ps
Energy per proton	400 GeV
Relative energy spread	0.035 %
Population	3×10^{11} protons

The simulation window length is indicated in each figure. I use a proton bunch with a Gaussian density distribution, both radially and longitudinally. The RIF [51], which enables the seed wakefields in the experiment, is replaced by a Heavyside step function in the density of the bunch at the time delays along the bunch indicated in the tables.

I study the effect of the plasma electron filament on two injected electron bunches, one for seeding and one to be accelerated, whose properties, in Table 5.1, are also based on AWAKE. I also study the effect of a plasma ramp on a positron bunch that has the same properties as the electron bunch. All beams, including the proton one, are set to have a waist, the position along z where σ_r

is minimum, at $z = 0\,\mathrm{m}$, ignoring space charge effects. I follow the evolution of the bunches and the plasma response in a window that is moving at c.

I use a low $n_{pe0} = 2 \times 10^{14}\,\mathrm{cm}^{-3}$ for simulations regarding seeding in the first plasma. I chose this density so that the time delay between microbunches $t_{\mathrm{delay}} \approx 1/f_{pe} \propto \sqrt{n_{pe}}$ is large enough to be resolved by the streak camera and, thus, enable a comparison with the experiment. The full set of parameters is in Table 5.2 and are based on AWAKE baseline parameters. These parameters are the same as the ones used in chapter 4. Results using these parameters are shown in Secs. 5.3, 5.4, and 5.5.

For simulations regarding acceleration in the second plasma (Sec. 5.6), I use a higher $n_{pe0} = 7 \times 10^{14}\,\mathrm{cm}^{-3}$ that leads to wakefields with the highest amplitude without incurring in filamentation [46], as $\sigma_{r0} \approx c/\omega_{pe}$. A higher amplitude can lead to larger energy gain for an injected electron bunch.

Table 5.3: Optimized simulation parameters [104] of the plasma with density step and proton bunch. This parameters are used for acceleration of positron or electron bunches.

Plasma and window param.	**Phys. value**
Constant plasma density (n_{pe0})	$7 \times 10^{14}\mathrm{cm}^{-3}$
Density step	$0.03 n_{pe0}$
Density step start	190 cm
Density step length	20 cm
Plasma radius	0.1 cm
Plasma length (L)	10 m
Simulation window width	0.11 cm
Resolution (trans. and long.)	4 μm
Proton bunch param.	
RMS radius (σ_{r0})	200 μm
RMS length (σ_z)	200 ps $\cdot\, c$
Normalized emittance (ϵ_N)	3.5 mm mrad
Seed position (ahead of bunch center)	200 ps
Energy per proton	400 GeV
Relative energy spread	0.035 %
Population	3×10^{11} protons

A density step [54] in the first plasma has been proposed to eventually stop the evolution of the microbunch train at a desired state and drive wakefields with a higher amplitude (compared to the case of a constant-density plasma). In simulations regarding acceleration in Sec. 5.6, I use a set of parameters that includes the density step and are optimized for maximum amplitude of the accelerating wakefields for an electron bunch. This set of parameters is specified in Table 5.3 and are also based on AWAKE baseline parameters.

Using only the first plasma, the amplitude of the wakefields can be indirectly measured from the energy gain of a witness electron bunch. This can be used, e.g., to study the effect of a density

Table 5.4: Simulation parameters of the plasma and proton bunch for studying the effect of the density step on the amplitude of the wakefields in the first plasma, based on [53].

Plasma and window param.	**Phys. value**
Constant plasma density (n_{pe0})	$1 \times 10^{14}\,\mathrm{cm}^{-3}$
Plasma radius	0.1 cm
Plasma length (L)	10 m
Simulation window width	0.11 cm
Transverse resolution	10.63 µm
Longitudinal resolution	0.0355 ps
Proton bunch param.	
RMS radius (σ_{r0})	105 µm
RMS length (σ_z)	250 ps $\cdot\, c$
Normalized emittance (ϵ_N)	1.4 mm mrad
Seed position (ahead of bunch center)	250 ps
Energy per proton	400 GeV
Relative energy spread	0.035 %
Population	1×10^{11} protons

step on the amplitude of the wakefields, where the expectation is an increase in the amplitude. Section 5.4 shows that an electron bunch is expelled when injected within the proton bunch, but it is possible that with an injection position behind the proton bunch, a fraction of the electron bunch charge reaches the plasma end. I study the behavior of the transverse wakefields behind the proton bunch, using the parameters in Table 5.4 which are based on [53]. All simulation parameters were chosen after suitable convergence tests (Appendix A).

5.3 Plasma electron filament in the ramp leading to the first plasma

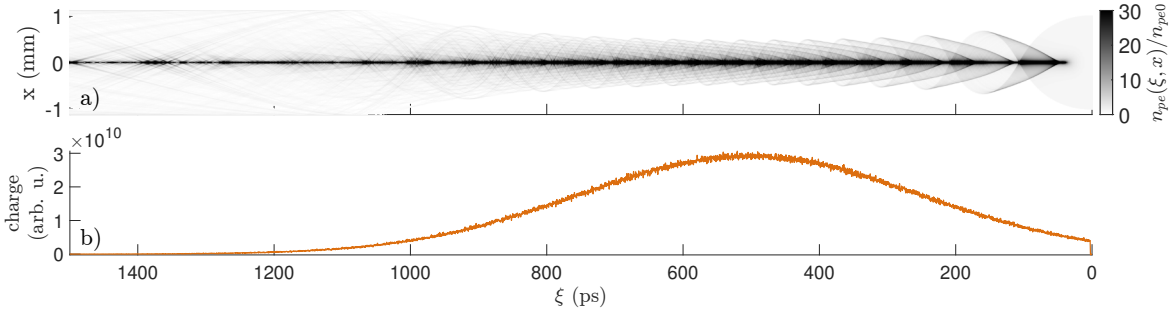

Figure 5.2: (a) Density distribution of the plasma electrons at the start of the plasma ramp forming a high-density filament, saturated at $30 n_{pe}(z)$ at $z = -1$ m to observe the fine structure off-axis, and mirrored about the axis (2D axisymmetric geometry). (b) Charge profile of the proton bunch, integrated in $|x| < 0.2$ mm, propagating to the right. The longitudinal binning for the proton bunch is $0.1\, c/\omega_{pe}$.

In this section, the density of the 10 m plasma is $2\times10^{14}\,\mathrm{cm}^{-3}$. I designate the position $z = -1\,\mathrm{m}$ (one meter upstream from the plasma entrance) as the start of the plasma ramp. The local density $n_{pe}(z = -1\,\mathrm{m}) = 1.25\times10^{9}\mathrm{cm}^{-3}$ is five orders of magnitude lower than in the long plasma and four orders of magnitude lower than n_{b0}. Under these conditions, $n_{pe} << n_{b0}$ and there is a non-linear response of the plasma to the proton bunch.

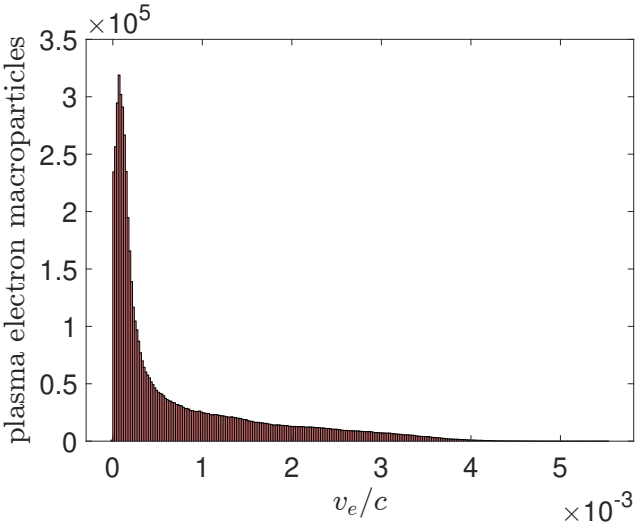

Figure 5.3: Histogram of plasma electron longitudinal velocity in the high-density filament at $z = -1\,\mathrm{m}$.

When the proton bunch propagates through the ramp, the plasma electrons are attracted by the transverse electric field E_r of the proton bunch and move towards the axis, creating a high-density filament, as seen in Fig. 5.2(a). The density distribution of the plasma electrons is shown in Fig. 5.2(a) and the proton bunch charge profile is in Fig. 5.2(b).

Figure 5.3 shows a histogram of the longitudinal velocity of the plasma electrons. The most common value is around $v_e = 5\times10^{-5}c$ and the maximum value is $v_e = 5.5\times10^{-3}c$. Therefore, the force that acts upon plasma electrons is mainly due to E_r. Assuming the limit $v_p \to c$, v_p the velocity of each proton, the azimuthal magnetic field of the bunch $B_\theta = E_r/c$ and the force due to the magnetic field that the plasma electrons are subject to $F_B = v_e B_\theta$, the force due to B_θ is much smaller than the one due to the E_r.

Figure 5.4(a) shows a zoom-in of the region behind the density cut in Fig. 5.2(a) together with the tracks of selected plasma electron macroparticles (red lines) at various transverse positions. The tracks show that the plasma electron macroparticles placed initially at $x \leq \sigma_r = 0.2\,\mathrm{mm}$ reach the axis at approximately the same time (same ξ) and create the spike in the on-axis density profile at $\xi \approx 48\,\mathrm{ps}$ in Figure 5.4(b). The plasma electron macroparticles initially placed in $x > \sigma_{r0}$ reach the axis at later times (larger ξ) the further from the axis their initial position is.

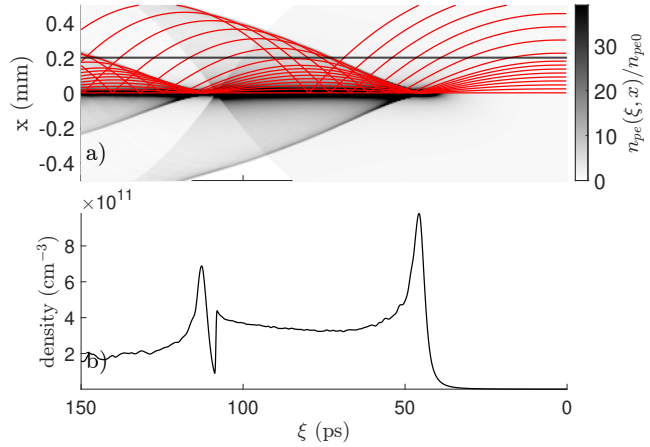

Figure 5.4: (a) Density distribution of the plasma electrons at the start of the plasma ramp forming a high-density filament, saturated at $30n_{pe}(z)$ at $z = -1$ m to observe the fine structure off-axis, and mirrored about the axis (2D axisymmetric geometry). The red lines indicate tracks of selected individual plasma electron macroparticles. The horizontal gray line is placed at $x = \sigma_{r0} = 0.2$ mm. (b) On-axis lineout of the plasma density in (a). The proton bunch (not in image) is propagating to the right.

In this case, as opposed to the case with a short bunch [99] (in which $\sigma_z \lesssim \lambda_{pe}/2$), Figs. 5.2(a) and 5.4 show that the plasma electrons do not leave the plasma after the spike, but return to the axis after crossing it. This is due to $E_r \propto q_b$, where q_b is the proton bunch charge. The charge profile has its center, i.e., maximum value and therefore maximum E_r, at $\xi = 500$ ps. The filament shows properties consistent with this, e.g., the caustic arcs[3] formed off-axis by the plasma electrons have their minimum width and length at $\xi = 500$ ps.

The transverse fields sustained by the filament are shown in Fig. 5.5. They are always negative, and, thus, defocusing for negatively charged particles, throughout the transverse extent of the plasma in the range $0 < \xi < 1000$ ps ($2\sigma_z$ ahead and behind the bunch center). Beyond that point, plasma electrons start leaving the plasma as the focusing force in the regions of lower n_b do not compensate for the transverse momentum that the plasma electrons acquired earlier along the bunch. Positive fields are observed near the plasma edges (this is discussed further in Sec. 5.7). The lineouts shown in Fig. 5.5(b) and Fig. 5.6(c) indicate that, within the proton bunch, the amplitude of the fields is approximately constant at distances from the axis where an injected charged bunch could be located $|x| < 0.4$ mm.

An approximation to the fields sustained in the blow-out regime can be calculated with Gauss' Law assuming only a charged cylinder with uniform density (the ion background). The situation with the filament is more complex, as the density changes both with x [Fig. 5.6(a)] and ξ

[3] Positions where the orbits of electrons share a common surface.

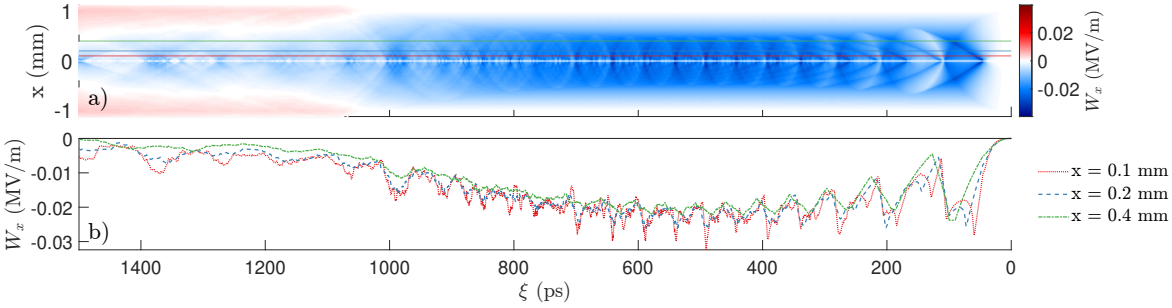

Figure 5.5: (a) Transverse fields sustained by the plasma electrons, mirrored about the axis (2D axisymmetric geometry). Fields with negative amplitude attract positively charged particles to the axis. (b) Lineouts of the transverse fields at various transverse distances.

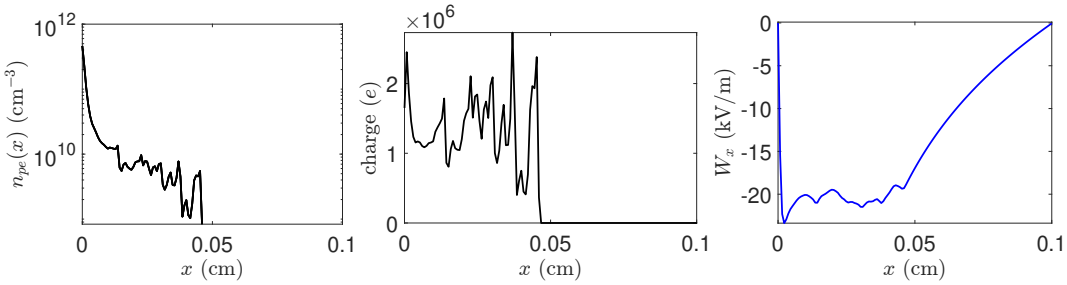

Figure 5.6: Transverse lineouts measured at $\xi = 500$ ps of (a) density of the plasma electron filament, (b) charge in the filament by integrating the density radially, and (c) transverse fields sustained by the filament. The high density on axis decreases quickly with x and the fields are relatively constant in the transverse region where a particle bunch could be injected.

[Fig. 5.2(a)]. A single negatively charged cylinder inside of the ion background is not enough to reproduce the fields from the filament.

Figure 5.6(a) shows a lineout in the transverse direction of the density in the filament, n_{fil}, at $\xi = 500$ ps. All plasma electrons are attracted to the axis due to E_r, therefore, n_{fil} is highly concentrated on axis and decreases quickly with x, where it is zero at $x > 0.46$ mm. Figure 5.6(b) shows the charge in the filament, obtained by

$$\text{charge} = 2\pi \int x\, n_{\text{fil}}\, dx. \tag{5.3}$$

It has several spikes along x but revolves around a constant value. Therefore, the field sustained by the filament is relatively constant in $x < 0.46$ mm and always defocusing for negatively charged particles, as is seen in Fig. 5.6(c). This region is larger than $c/\omega_{pe} = 0.376$ mm, thus, a bunch leaving this area cannot be recovered by focusing wakefields later in the constant-density plasma.

Figure 5.7(a) shows the seed electron bunch (in orange) placed within the proton bunch, and, thus, within the filament, at a possible injection position in ξ, together with its charge profile in Fig. 5.7(b) and the charge profile of the filament in Fig. 5.7(c). The position of the tracks (red lines) in Fig. 5.7(a) is not significantly different in the extent of the electron bunch when compared to Fig. 5.4(a) without bunch, although they differ behind the electron bunch. This difference is also seen in the charge profile of the filament in Fig. 5.4(c) and Fig. 5.7(b) in $\xi > 100$ ps.

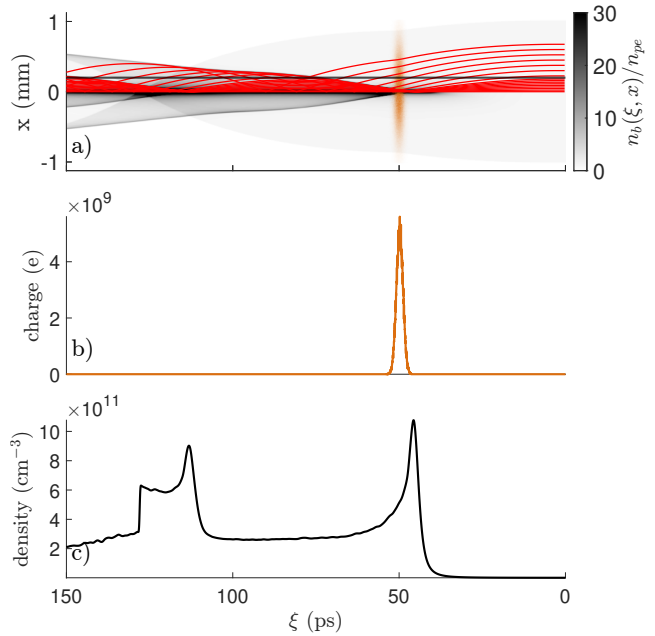

Figure 5.7: (a) Density distribution of the plasma electrons (gray) at the start of the plasma ramp forming a high-density filament, saturated at $30n_{pe}(z)$ at $z = -1$ m to observe the fine structure off-axis, together with the electron bunch density distribution (orange). Both mirrored about the axis (2D axisymmetric geometry). The red lines indicate tracks of selected individual plasma electron macroparticles. The horizontal gray line is placed at $x = \sigma_{r0} = 0.2$ mm. (b) Charge profile of the electron bunch by integrating its density in $|x| < 0.2$ mm. (c) On-axis lineout of the plasma density in (a). The proton bunch (not in image) and electron bunch are propagating to the right.

A negatively charged bunch is subject to defocusing fields when injected in the region $0 < \xi < 1000$ ps. Depending on the energy of the bunch, it could be completely expelled from the wakefields before reaching the plasma entrance. As an example, observing Fig. 5.5, I consider the amplitude of the transverse fields $W_x \approx 20$ kV/m, and a test electron initially on-axis with energy of 19 MeV and no transverse momentum. The propagation distance needed to move it transversely can be calculated by

$$z_{\text{expel}} = \sqrt{\frac{2\gamma m_e x c^2}{e W_x}}. \tag{5.4}$$

The electron is expelled away from the wakefields by a distance c/ω_{pe} in $z_{\text{expel}} = 87\,\text{cm}$, i.e., before it reaches the plasma entrance. As can be seen in Fig. 5.8, W_x increases as $n_{pe}(z)$ increases, which means that the bunch could be expelled even earlier. Protons with $\gamma = 426.3$ move only 0.25 μm in $z = 1\,\text{m}$ considering $W_x = 20\,\text{kV/m}$ as before.

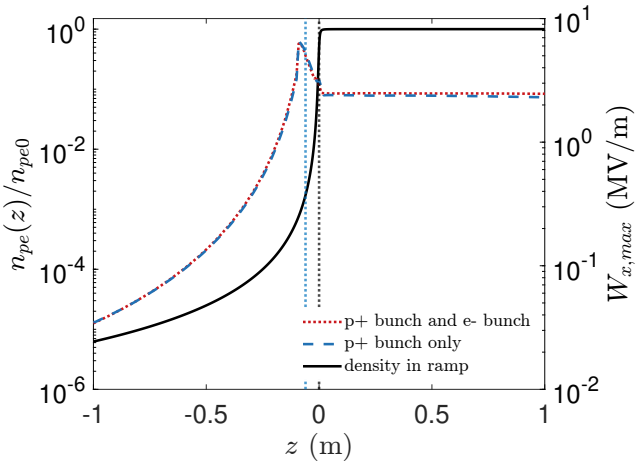

Figure 5.8: Maximum amplitude of the transverse wakefields in $\xi < 67\,\text{ps}$, the region where a seed bunch could be injected, for a proton and a seed electron bunch propagating co-axially (red line) and for only a proton bunch (blue line). The local plasma density is shown by the black line. All lines are in logarithmic scale. The blue vertical line indicates the position where $n_{pe}(z) = n_b(\xi = 67\,\text{ps})$ and the gray vertical line indicates the position of the plasma entrance.

Figure 5.8 shows that W_x is unaffected by a seed electron bunch at the injection position. Figure 5.7, when compared with Fig. 5.4, shows that this occurs because the change due to the electron bunch charge in the trajectories of the plasma electrons in the filament becomes significant only behind the electron bunch.

Figure 5.8 also shows that before the z-position where $n_{pe} = n_{b0}$, there is a non-linear plasma response where a filament is formed and, therefore, there will always be defocusing fields for a negatively charged bunch. After the plasma entrance, where $n_{pe} >> n_{b0}$, the plasma has a linear behavior. Thus, ignoring the phase slippage of the fields during SM growth [13, 14], there is either a focusing phase where a negatively charged bunch can be injected and remain on axis or, due to the adiabatic response of the plasma to the proton bunch, a less defocusing region that will eventually be focusing due to SM [see, e.g., Fig. 1.4(b) in chapter 1], where it might also be possible to inject an electron bunch.

5.4 Effect on an injected bunch for seeding in the first plasma

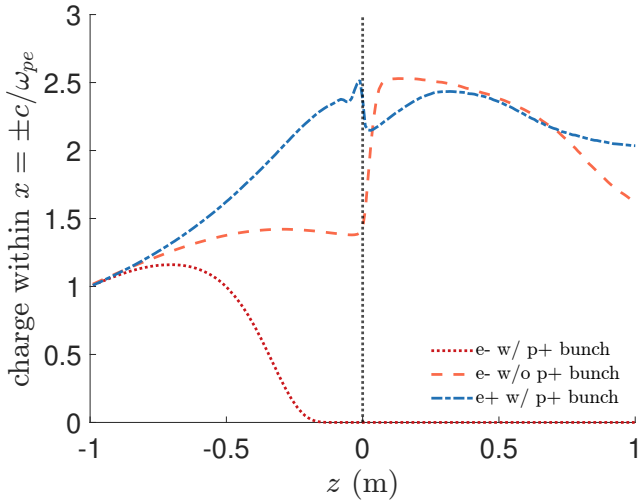

Figure 5.9: Charge evolution of seed charged particle bunches while propagating through the plasma ramp for three cases, indicated in the legend. Charge is calculated by integrating the density given by LCODE in $|x| < c/\omega_{pe} = 0.376\,\text{mm}$. A value of 1 indicates the amount of charge within $|x| < c/\omega_{pe}$ at $z = -1\,\text{m}$. The gray vertical line indicates the position of the plasma entrance. The electron bunch within the proton bunch is expelled completely before reaching the plasma entrance, while the electron bunch in front and the positron bunch remain on axis and can drive seed wakefields.

I place a seed electron bunch 50 ps behind the SM seeding position and let both proton and electron bunches propagate through the plasma ramp. Figure 5.9 shows that the electron bunch charge (red line) is lost from the region that wakefields would occupy once inside the long, constant-density plasma about 20 cm before reaching the entrance. This charge loss is also observed experimentally [94]. When there is no proton bunch, the electron bunch (orange dashed line) can propagate through the plasma ramp and reach the plasma entrance, where it focuses by its own wakefields and can drive seed wakefields for SM. In eSSM, successfully demonstrated experimentally [53], the electron bunch is placed ahead of the proton bunch, and thus is not subject to the fields sustained by the filament.

An electron bunch with higher energy may reach the plasma entrance and drive seed wakefields even with the plasma ramp and within the proton bunch. However, it was demonstrated in simulations that a high-energy bunch is less effective at seeding SM and is detrimental to the microbunch train [86, 105]. To obtain a longer microbunch train, the seed electron bunch should stop driving wakefields, e.g., by being expelled from the wakefields, after successfully given enough transverse momentum to the protons. A high-energy bunch remains on axis driving wakefields

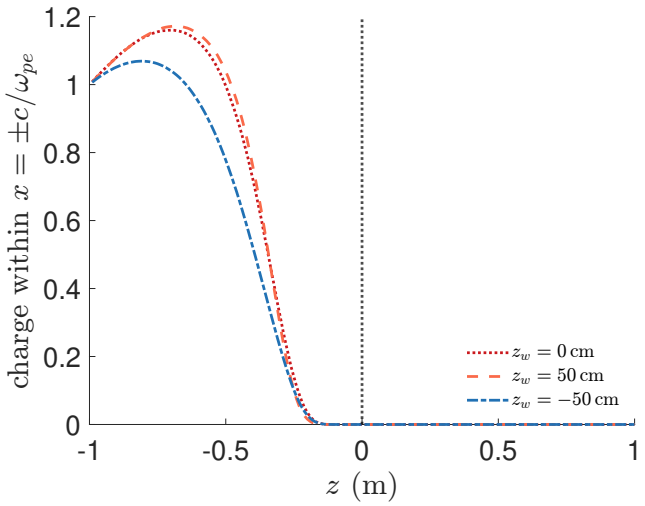

Figure 5.10: Charge evolution of seed electron bunches while propagating through the plasma ramp for three waist positions z_w. Charge is calculated by integrating the density given by LCODE in $|x| < c/\omega_{pe} = 0.376\,\text{mm}$. A value of 1 indicates the amount of charge within $|x| < c/\omega_{pe}$ at $z = -1\,\text{m}$. The gray vertical line indicates the position of the plasma entrance. The electron bunch charge is lost before the plasma entrance in all cases.

with a fixed phase, which interfere with the wakefields from SM due to their intrinsic dephasing [13, 14, 48, 49] (and discussed in chapter 3). This interaction causes expulsion of the microbunches that are out of phase with the wakefields from the electron bunch [105]. An optimization to find the best value between the energy of the electron bunch and efficient seeding is out of the scope of this work.

In Fig. 5.9 there is a slight defocusing of the electron bunch before the plasma entrance due to the space charge and the relatively low energy of the bunch, which can be seen by the decrease in the charge within c/ω_{pe} from $z = -0.4$ to 0 m. The waist position z_w for this electron bunch does not affect the fact that it is expelled from the wakefields before it reaches the plasma entrance, as can be confirmed in Fig. 5.10, where the charge evolution for electron bunches with $z_w = -0.5$ and +0.5 m is displayed. This occurs because the effect of the defocusing force is larger than the convergence of the beam to the axis.

The positron bunch propagating within the proton bunch is focused by the fields sustained by the filament, as expected, and the charge within c/ω_{pe} increases with z. The positron bunch reaches the plasma entrance where it can also drives seed wakefields. This indicates that positron bunch seeding from within the proton bunch (e+SSM) is possible, if there were any available positron bunches with the same properties as the seed electron bunch. With this configuration, the evolution of the SM starting from two seeds (RIF and e+SSM) could be investigated.

A shorter ramp is beneficial for the injection of charged bunches. The lower n_{pe} at any given z means less charge in the plasma electron filament, and thus, lower amplitude of the defocusing fields sustained. This can be obtained in the experiment by shrinking the size of the orifice between the vapor source and the expansion volume. The minimum practical aperture size is 3 mm [106]. An additional simulation was performed using this value. Figure 5.11 shows that the electron bunch charge was expelled from the wakefields before reaching the plasma entrance. The focusing wakefields driven by the off-axis electron bunch charge bring back a small amount of charge within $|x| = c/\omega_{pe}$, but the defocusing wakefields driven by the proton bunch quickly expel it. Therefore, reducing the aperture size from 5 to 3 mm is not sufficient to overcome the detrimental effects of the ramp.

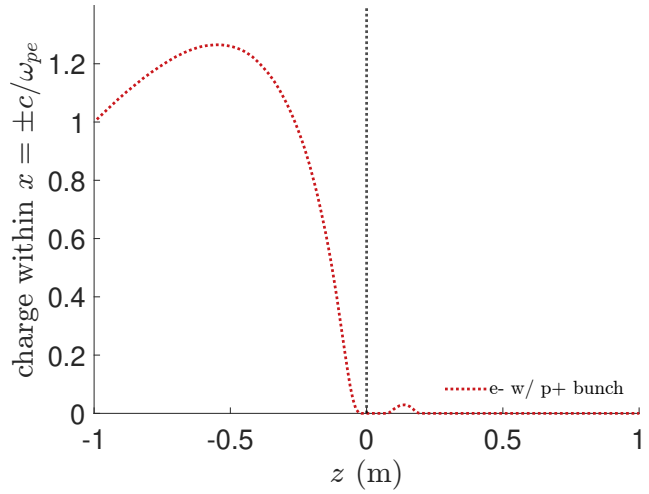

Figure 5.11: Charge evolution of seed electron bunches while propagating through a shorter plasma ramp. Charge is calculated by integrating the density given by LCODE in $|x| < c/\omega_{pe} = 0.376$ mm. A value of 1 indicates the amount of charge within $|x| < c/\omega_{pe}$ at $z = -1$ m. The gray vertical line indicates the position of the plasma entrance. The electron bunch charge leaves the wakefields before the plasma entrance.

5.5 Plasma electron filament in the second plasma

The future plan for AWAKE will follow what I mentioned in Sec. 5.1: two plasmas, the first one for SM and the second one for acceleration. Although currently not the case in AWAKE, there could be a plasma ramp leading to the entrance to the second plasma, described also by Eq. 5.2 and with the same orifice size as the ramp leading to the first plasma ($r_o = 5$ mm).

Considering $n_{pe} = 2 \times 10^{14}\text{cm}^{-3}$ in the constant-density plasma, at the ramp start $\lambda_{pe}(n_{pe} = 1.25 \times 10^{9}\,\text{cm}^{-3}) = 94$ cm is long compared to σ_z and to $\lambda_{pe}(n_{pe} = 2 \times 10^{14}\,\text{cm}^{-3}) \approx 2.3$ mm. The

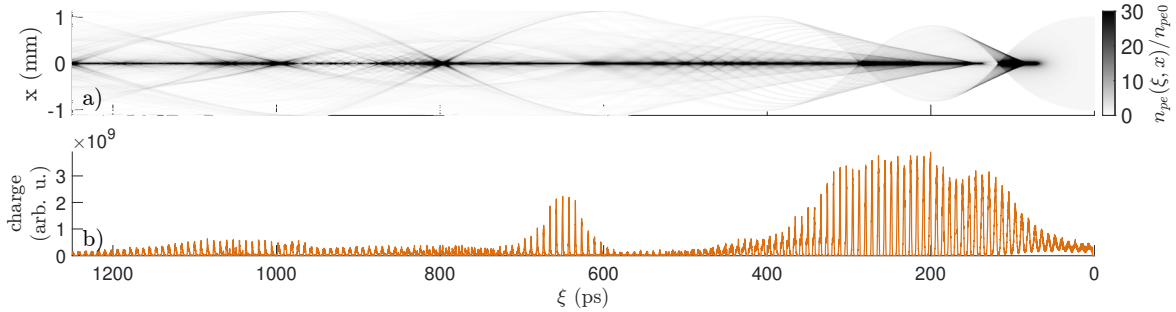

Figure 5.12: With $n_{pe} = 2 \times 10^{14}\,\mathrm{cm}^{-3}$: (a) Density distribution of the plasma electrons at the start of the plasma ramp of the second plasma $z = 10\,\mathrm{m}$, saturated at $30n_{pe}(z)$ at $z = 10\,\mathrm{m}$ to observe the fine structure away from the axis, and mirrored about the axis (2D axisymmetric geometry). (b) Charge profile of the microbunch train, integrated in $|x| < 0.2\,\mathrm{mm}$, propagating to the right.

plasma electrons do not have a periodic movement with a λ_{pe} similar to the length between microbunches. Since the proton bunch has lost at least half of its charge by the time it is transformed into a microbunch train due to the spacing of the microbunches, its overall density within $|x| < 0.2\,\mathrm{mm}$ is at most half of that of the proton bunch at $z = 0\,\mathrm{m}$.

To compare directly with the filament shown in Fig. 5.2, I let the proton bunch from the previous section (Sec. 5.4) described in Table 5.3 propagate in a constant-density plasma with $n_{pe0} = 2 \times 10^{14}\,\mathrm{cm}^{-3}$ for 10 m, where it self-modulates and transforms into the microbunch train shown in Fig. 5.12. After the plasma, it enters into a second plasma ramp with the same properties as the one leading to the first plasma entrance, shown in Fig. 5.12. I do not include an exit ramp in the first plasma.

Figure 5.12(a) shows that a filament is also formed, with properties corresponding to a lower-density unmodulated bunch. The charge of the microbunch train, in Fig. 5.12(b), decreases drastically after $\xi = 350\,\mathrm{ps}$. The caustic arcs are only increasing in size, and are much longer and wider than in Fig. 5.12. This is a consequence of the plasma electrons having a weaker attraction to the axis when compared to the case with the unmodulated proton bunch, due to the lower overall density of the microbunch train.

5.6 Effect on injected bunches for acceleration in the second plasma

To study the effect of the fields sustained by the filament on an electron and positron bunch injected for acceleration in the second plasma, I use $n_{pe0} = 7 \times 10^{14}\,\mathrm{cm}^{-3}$, and a density step [54] in the first plasma. By including a density step, a microbunch train that drives wakefields with a

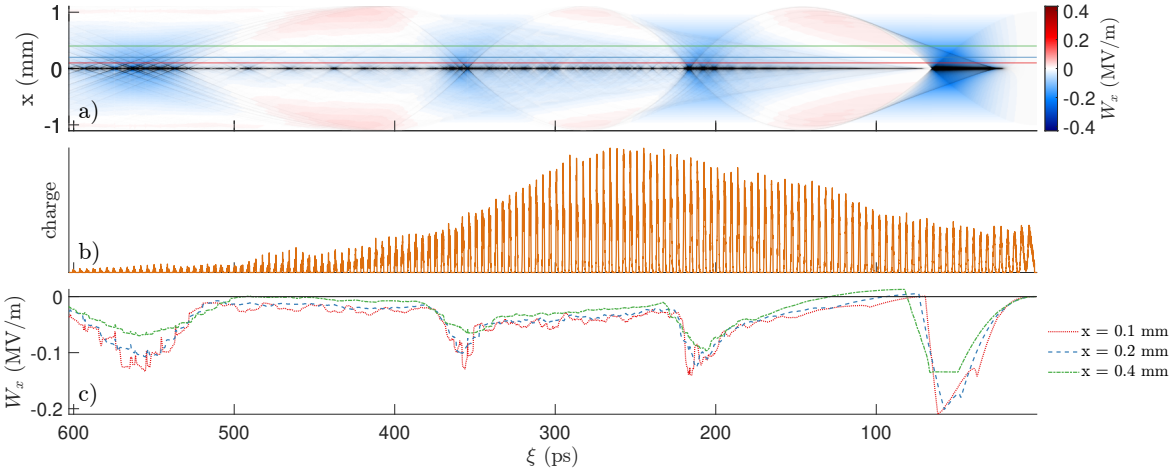

Figure 5.13: $n_{pe} = 7 \times 10^{14}\,\mathrm{cm}^{-3}$: (a) Density distribution of the plasma electrons forming a high-density filament on axis as a response to the microbunch train at $z = 10.4\,\mathrm{m}$, which is the injection position of the electron bunch for acceleration, together with the transverse fields, where fields with negative amplitude attract positively charged particles to the axis. Both mirrored about the axis (2D axisymmetric geometry). (b) Charge profile of the microbunch train, integrated in $|x| < c/\omega_{pe}$, propagating to the right. (c) Lineouts of the transverse fields at various transverse distances.

higher amplitude and constant phase[4] is formed. This microbunch train propagates into a second plasma, also separated from the first plasma by a 1 m vacuum gap. The electron bunch to be accelerated, injected at $z = 10.4\,\mathrm{m}$ [107], propagates collinearly with the microbunch train. The second plasma entrance is at $z = 11\,\mathrm{m}$.

The longer microbunch train, compared to the train that self-modulated in a constant-density plasma, also attracts plasma electrons to form a filament on axis, as seen in Fig. 5.13. The increased $n_{pe}(z)$ leads to wider caustic arcs with more charge that sustain some off-axis regions with focusing fields for negatively charged bunches, e.g., around $\xi \approx 100$, 270, and 450 ps. In contrast to the case with the unmodulated proton bunch, the amplitude of the fields is not approximately constant along ξ. There are peaks around $\xi = 60, 220, 360$, and 560 ps, surrounded by regions along ξ, e.g. $380 < \xi < 500\,\mathrm{ps}$, that have defocusing fields with lower amplitude.

I inject bunches at two different time delays along ξ. One close to the second peak in the defocusing fields $\xi = 201.5\,\mathrm{ps}$, and one behind it, where the amplitude is lower $\xi = 260\,\mathrm{ps}$. All bunches are placed so that they are in focusing wakefields once inside the long plasma. The fields in Fig. 5.13 evolve with z as $n_{pe}(z)$ increases and as the microbunches expand transversely in the ramp. They have the largest variation around the second plasma entrance, where the plasma density changes

[4] Or at least a phase with changes small enough for acceleration of charged particle bunches for applications.

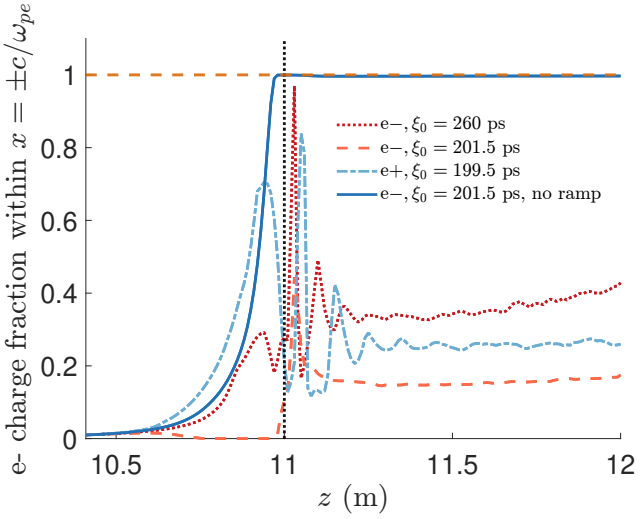

Figure 5.14: Charge evolution of injected electron or positron bunches for acceleration while propagating through the plasma ramp (red, orange, and light blue lines) and through vacuum and plasma with a sudden start of the plasma at the plasma entrance (blue continuous line). Bunch charge is calculated by summing the charge of each macroparticle within $|x| < c/\omega_{pe} = 0.2\,\mathrm{mm}$. A value of 1 indicates the total amount of charge in the bunch (horizontal yellow slashed line). The legend indicates injection time delay. The gray vertical line indicates the position of the plasma entrance. All bunches lose more than half of the initial charge when propagating through the plasma ramp within the microbunch train.

rapidly. For comparison, I also include the case of an injected electron bunch propagating within the microbunch train in vacuum, i.e., without a plasma ramp.

Figure 5.14 shows that the focusing to the plasma entrance of the electron bunch placed at $\xi = 201.5\,\mathrm{ps}$ (slashed orange line) is hindered by the defocusing fields from the filament and its charge is completely out of the region $|x| = c/\omega_{pe}$ before reaching the plasma entrance, although it remains within the plasma. Upon entering it, the off-axis electron bunch charge drives its own focusing wakefields and come back to the axis. About 20 % of the charge remains within $|x| = c/\omega_{pe}$. The bunch at $\xi = 260\,\mathrm{ps}$ (dotted red line) follows a similar course but due to the lower amplitude of the fields, a larger fraction reaches the plasma entrance. At $z = 12\,\mathrm{m}$, approximately 40 % of the charge remains within $|x| = c/\omega_{pe}$.

The positron bunch (dashed blue line) is initially focused by the fields sustained by the filament, and the charge within c/ω_{pe} grows faster along z than in the case of the bunch propagating in vacuum. Nevertheless, as seen in Fig. 5.17 with the periodicity of the wakefields and the absence of a filament, at the plasma entrance, $n_{pe}(z) > n_{b0}$ and the plasma response starts to become more linear. Together with n_{pe}, $\omega_{pe} \propto \sqrt{n_{pe}}$ also changes rapidly, and, therefore, also the amplitude of the wakefields at a fixed ξ. There, the positron bunch is briefly subject to defocusing fields of 9 MV/m, as observed in Fig. 5.15. Two centimeters afterwards, the average amplitude has a

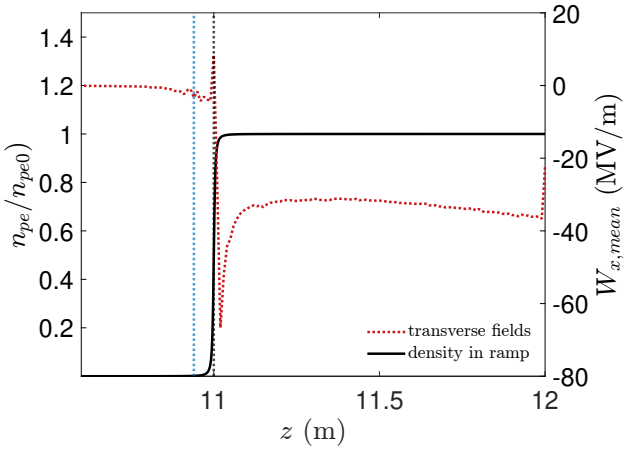

Figure 5.15: Average amplitude of the transverse fields in $198.6 < \xi < 199.9$ ps, the region where the positron bunch is injected, when a microbunch train propagates through the plasma ramp leading to the second plasma. Local plasma density (black line), position where $n_{pe}(z) = n_{b0}$ (blue vertical line) and position of the second plasma entrance (gray vertical line). The fields change rapidly around the plasma entrance, becoming defocusing for positively charged particles for a few centimeters.

maximum of 67 MV/m, which focuses the positron bunch. Thereafter, the amplitude decreases to under 36 MV/m, and a fraction of the positrons escapes the wakefields, as the focusing fields cannot counteract their outward momentum gained in the large amplitude fields just after the plasma entrance. At $z = 12$ m, 25 % of the charge remains within $|x| = c/\omega_{pe}$.

The normalized emittance ϵ_N of the injected bunches increases during the ramp because the transverse fields are not linear in x. Figure 5.16 shows ϵ_N of both electron and positron bunches considering a transverse extent of whichever is largest between their rms width $\sigma_{re}(z)$ when propagating in vacuum and $c/\omega_{pe} = 0.2$ mm, $|x| < \max(\sigma_{re}(z), c/\omega_{pe})$. It is calculated in LCODE (using normalized PIC units) as

$$\epsilon_N^2 = \langle x^2 \rangle \left(\langle p_x^2 \rangle + \langle p_\theta^2 \rangle \right) - \langle x p_x \rangle^2, \tag{5.5}$$

where p_x and p_θ are the transverse and azimuthal components of the momentum of the electron macroparticles, respectively. By the time the bunch reaches the plasma entrance, ϵ_N grows by approximately one order of magnitude, and further increases afterwards since what remains of the bunch is not matched to the focusing wakefields in the long plasma, reaching a value of $\epsilon_N \approx 250$ mm mrad at $z = 12$ m. The emittance of the electron at $\xi_0 = 201.5$ ps appears discontinuous because all charge left momentarily the region around the axis before the plasma entrance, so that there was no emittance to measure in that region. Nevertheless, a fraction still in the plasma comes back to axis due to focusing fields as the bunches propagate trough the plasma entrance. For

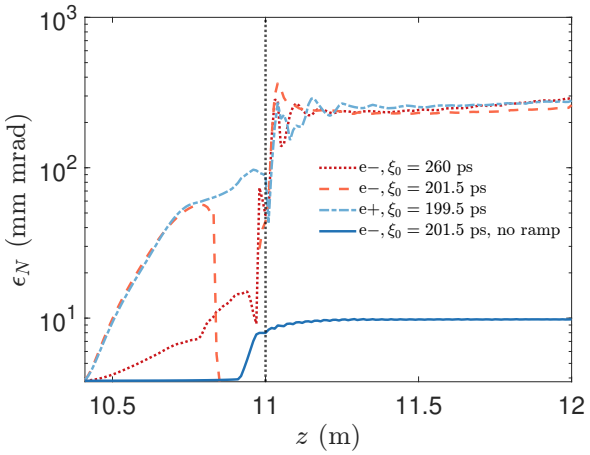

Figure 5.16: Normalized emittance evolution of injected bunches for acceleration while propagating through the plasma ramp (red, orange, and light blue lines) and with a sudden start of the plasma at the plasma entrance (blue continuous line). In all cases they are propagating within a microbunch train. The legend indicates injection time delay. The gray vertical line indicates the position of the plasma entrance.

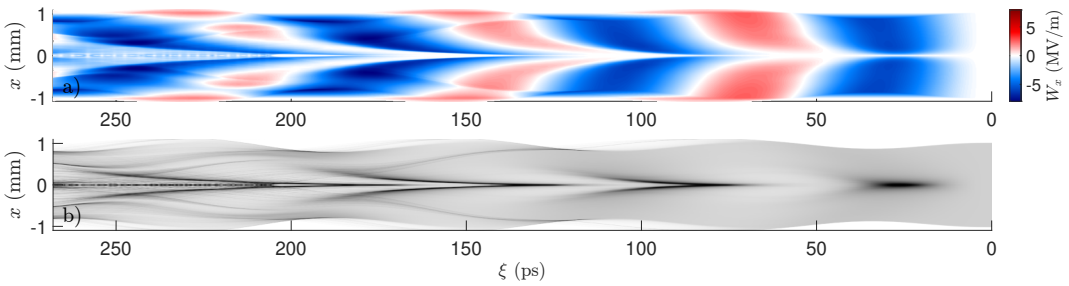

Figure 5.17: (a) Transverse fields driven by the microbunch train (not in image) at $z = 11$ m, propagating to the right. Wakefields with negative amplitude attract positively charged particles to the axis. (b) Plasma electron density distribution.

comparison, ϵ_N of the electron bunch propagating in vacuum remains constant until the plasma entrance, as expected, and increases slightly to 9.8 mm mrad. The emittance remains constant until $z = 12$ m, which is the end of the simulation.

Even though the parameters of the electron bunch were calculated considering the matching condition in a blow-out, Fig. 5.18 shows that the electron bunch is only partially in a blow-out. There was no optimization of the electron bunch parameters to match the focusing force in the long plasma and no optimization in beam loading either. Thus, in these simulations, matching should be not expected. Disregarding the charge loss, the emittance increase due to the ramp makes the charged particle bunches not suitable for applications in particle physics, as larger emittance leads to less charge on target [108].

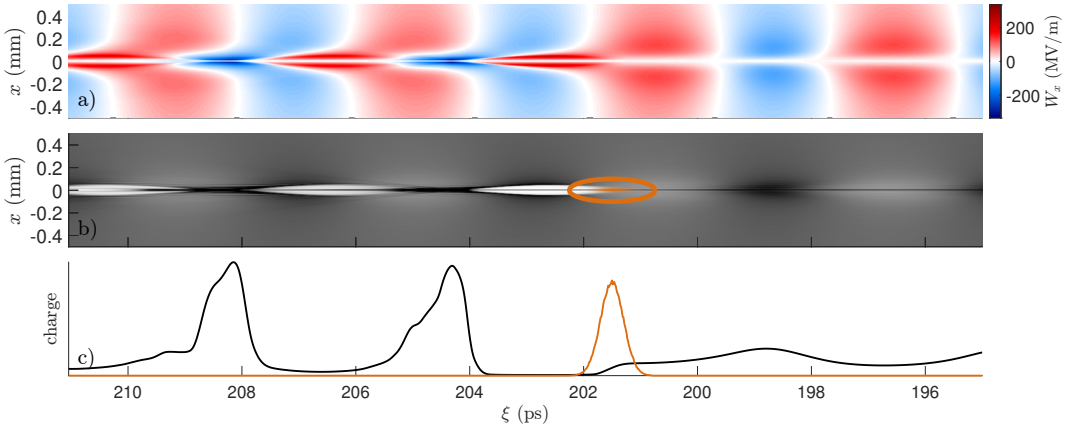

Figure 5.18: (a) Transverse wakefields driven by the microbunch train (not in image) at $z = 11$ m (no ramp), wakefields with negative amplitude attract positively charged particles to the axis. (b) Density distribution of the plasma electrons (gray), together with the density distribution of the electron bunch (orange). A thick orange ellipse has been drawn to facilitate finding the electron bunch. Both (a) and (b) mirrored about the axis (2D axisymmetric geometry) and the bunches are propagating to the right. (c) Charge profile of the plasma electrons (black) and the electron bunch (orange), integrated in the region close to the axis $|x| < 20\,\mu$m.

5.7 Effect on injected bunches for acceleration in the first plasma

In the experiment, a witness electron bunch can be injected on axis to study indirectly the amplitude of the wakefields by measuring its energy gain. As explained previously in Sec. 5.4, a low-energy electron bunch, as the one available at AWAKE, is expelled from the wakefield when propagating through the plasma ramp and within the proton bunch. Nevertheless, behind the proton bunch, the transverse momentum gained by the plasma electrons in the more dense proton bunch center is not counteracted by E_r of the ion background and less dense bunch rear. The plasma electrons are then expelled from the radially bound plasma. The plasma behind the bunch is then not neutral, and sustains off-axis focusing fields for negatively charged bunches, since the remaining plasma electrons stay close to the axis. This is already seen in Fig. 5.5 but is more clearly seen in Fig. 5.19(a), which is made by averaging the transverse fields in the range $-1 < z < -0.1$ m. In this range there is only a non-linear plasma response. Data is taken every 1 cm. Starting at $\xi = 567$ ps, off-axis focusing fields for negatively charged particles appear.

The black line in Fig. 5.19(b), shows the amount of plasma electrons within the plasma radius (1 mm), obtained with Eq. 5.3 at each data point, followed by a weighted average of the plasma electron charge from all data points. The weight at each frame is the maximum value of the plasma electron charge. The plot shows that, on average, the plasma electrons start leaving the plasma at $\xi = 567$ ps, coinciding, as expected, with the appearance of focusing fields.

An electron bunch that is injected on axis behind the proton bunch is subject to defocusing fields of lower amplitude [Fig. 5.19(c)] when compared to the case of injecting at the front or center of the proton bunch. The focusing fields off axis can bring back to the axis the electron bunch charge that could have been previously expelled. Nevertheless, it should be noted that behind the bunch, it is more likely that particle trajectory crossing [83] of plasma electrons has occurred and the fields are not at their maximum along ξ. This could be mitigated by seeding behind the bunch center. Considering this, even with the plasma ramp, an electron bunch injected on axis could be used to indirectly measure the amplitude of the wakefields through its energy gain. For this objective, the electron bunch emittance and the amount of charge remaining in the plasma are expected to be acceptable as long as the bunch energy can be measured in the experiment.

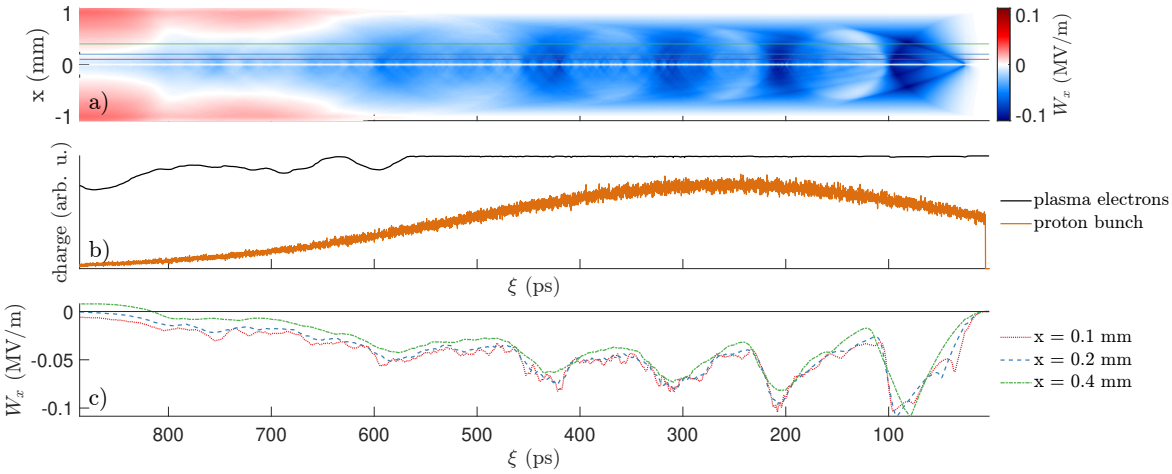

Figure 5.19: (a) Average transverse fields sustained by the plasma electrons (see text), mirrored about the axis (2D axisymmetric geometry). Fields with negative amplitude attract positively charged particles to the axis. (b) Proton bunch charge profile (orange line) and weighted average plasma electron charge profile (black line, see text). Charge obtained by integrating within $x = \pm 1$ mm (plasma radius). (c) Lineouts of the transverse fields in (a) at various transverse distances.

5.8 Conclusion

I showed that the non-linear plasma response to a long proton bunch where $n_{b0} >> n_{pe}$ is to create a high-density filament on axis due to the flow-in of plasma electrons. The fields sustained by this filament do not increase linearly with the distance to the axis, but rather have a complex structure that changes along and across the bunch. This phenomenon can occur, e.g., in a plasma ramp leading to a long constant-density plasma.

The fields sustained by the filament are defocusing and detrimental for an injected charged particle bunch. Simulations results show that they may expel an electron bunch out of the wakefields

and increase the emittance of electron and positron bunches. An electron bunch with an energy of 19 MeV placed within the proton bunch, which may be use to seed the self-modulation when placed in front of it, is completely expelled from the wakefields before reaching the plasma entrance, irrespective of its waist position within 0.5 m and irrespective of the length of the ramp within practical experimental limits (with a minimum orifice radius of 3 mm). On the contrary, a seed positron bunch is focused to the axis and reaches the plasma entrance, without losing charge.

A plasma electron filament is also formed when the modulated proton bunch, transformed into a microbunch train by self-modulation, propagates through the ramp. Nevertheless, the reduced charged of the microbunch train compared to the unmodulated bunch leads to a filament with wider and longer caustics arcs. A charged particle bunch injected for acceleration within the microbunch train is, thus, also affected by the ramp.

A 150 MeV electron or positron bunch is partially expelled before reaching the plasma entrance, and its normalized emittance increases between one and two orders of magnitude. Once inside the plasma, the bunch has a complex evolution and the charge remaining is between 20 % and 40 % of the initial charge. The charge and emittance of the bunch are no longer suitable for applications. For comparison, an electron bunch propagating within the microbunch train in vacuum with a sudden start of the long plasma (no plasma ramp) loses no charge and its emittance increases slightly, for example from 8.0 to 9.8 mm mrad, only once inside of the plasma, due to the bunch properties not being optimized for emittance preservation.

The results therefore show that a plasma ramp should be avoided for the acceleration of electrons or positrons in a proton-driven plasma wakefield accelerator relying on self-modulation. The future plan for AWAKE includes a counter-propagating laser pulse to create the plasma, which meets with the electron bunch at the plasma entrance, avoiding the detrimental effects of the ramp (see chapter 1).

Witness bunches can be used in the experiment to assess the amplitude of the wakefields by measuring their energy gain. The plasma electrons of the filament leave the plasma transversely after the proton bunch, because the focusing fields of the back of the bunch do not stop the plasma electrons that have gained transverse momentum from the fields in the bunch center. This leads to lower defocusing fields and off-axis focusing fields for negatively charged particles after the proton bunch.

6 Conclusions and Outlook

> "There is no royal road to science, and only those who do not dread the fatiguing climb of its steep paths have a chance of gaining its luminous summits" - Karl Marx

Plasma wakefield acceleration promises a great improvement over current acceleration technology. This includes accelerating gradients up to hundreds of GeV/m, or even TeV/m, much larger than the one given by the limit of current technology of 100 MV/m. This increase in the accelerating gradient allows for the accelerators to be much smaller and cheaper to produce for a given energy of the accelerated particles. This, in turn, democratizes accelerator technology to be used, e.g., for cancer treatment or to study particle physics, including physics beyond the Standard Model.

The Advanced Wakefield Experiment (AWAKE) aims to build an accelerator using the long proton bunch from CERN. Through self-modulation, the long bunch is transformed into a microbunch train that resonantly drives wakefields. The goal of AWAKE is to produce wakefields with an amplitude of 1 GV/m and accelerate electron bunches up to 200 GeV per electron, in a bunch with a mm mrad emittance and percent level energy spread, to use in applications for particle physics.

Particle-in-cell simulations aim to reproduce the physics in plasmas, especially when measurements cannot be done. They are also used to predict the outcome of experimental setups, which is a crucial step in the design of experiments.

In this work, I show how particle-in-cell simulations confirm and go beyond theoretical predictions and reproduce experimental results. Simulations reveal details of the plasma response not included in the simplified linear theory. They also reveal the detrimental effects of a plasma density ramp leading to a long plasma.

I show with simulations the effects of charge neutralization by the plasma electrons of proton and antiproton bunches propagating in plasma, effects that are not considered in linear theory. In the case of a charged bunch longer than the plasma wavelength, the charge neutralization leads to an effective plasma density variation in the longitudinal and transverse directions, following the density distribution of the bunch. This spatial dependence thus affects the plasma frequency, since the plasma frequency is proportional to the square root of the effective plasma density. A simple model can be used to approximate the local plasma frequency:

$$f_{pe,osc} = \frac{1}{2\pi}\sqrt{\frac{(n_{pe} \pm n_b(\xi, r))e^2}{m_e \epsilon_0}}. \tag{6.1}$$

The initial frequency of the wakefields is imprinted on the initial modulation frequency of the proton bunch. In order to produce long microbunch trains that drive high-amplitude wakefields, e.g., by the use of a density step, the relation between the frequency of the wakefields and modulation frequency must be well understood. Future work can look into whether the plasma frequency given by the plasma density after the optimum density step is related to the initial modulation frequency.

Furthermore, the transverse spatial dependence of the plasma electron oscillation frequency leads to two consequences: the plasma electrons do not oscillate resonantly and there is eventually particle trajectory crossing. I show for the first time that the plasma electrons not oscillating resonantly leads to a decreases in the amplitude of the wakefields along the bunch. This effect must be considered to correctly analyze measurements depending on the energy deposited in the plasma, such as plasma light or shadowgraphy. Future research will be performed to determine the flow of energy among the drive bunch, plasma electrons, and wakefields.

I show for the first time that there is good agreement between simulation and experimental results at the plasma end regarding the microbunch train density profile, modulation frequency, and the energy gain of test electrons, in the case of proton bunches propagating and self-modulating in plasmas with linear density gradients. The experimental results show the expected effects of a slowing phase velocity of the wakefields during self-modulation growth, predicted by theory, which are reproduced in simulations. Among these effects are the longer microbunch trains created with positive gradients, and shorter microbunch trains for negative gradients. Simulation results confirm that this is the result of the additional positive phase velocity generated with positive gradients, counteracting the slowdown due to self-modulation growth. Likewise, negative gradients enhance that slowdown.

The modulation frequency of the microbunch trains also shows the asymmetry in the effects between applying negative and positive gradients: in the cases with negative gradients, the modulation frequency is similar to the plasma frequency at the end of the plasma, whereas the modulation frequency with positive gradients is closer to the frequency at the plasma beginning. With negative gradients, where the charge is continuously expelled from the modulated proton bunch, after the end of the plasma, the transverse dependence of the modulation frequency reflects the expected plasma frequency along the plasma due to the density gradient. This does not occur with positive gradients, since the compensation of both effects, slowdown of phase velocity from SM and speedup of phase velocity due to the gradient, leads to a relatively constant phase of the wakefields and less change in the frequency, together with less charge loss. Both transverse frequency

dependence and charge loss were measured in the experiment and are confirmed by simulation results.

The maximum amplitude of the wakefields is reached with a gradient of 0.5 %/m, where there is an optimum combination of microbunch train length, microbunch charge, and microbunches being in the decelerating phase of the wakefields. This gradient leads to the maximum possible energy gain to externally side-injected test electrons. This is confirmed in experiments, in which this gradient value leads to electrons with the largest energy gain. It has been shown that a positive plasma density gradient with a limited extent can have the same effect as a plasma density step, thus, further studies can be done to understand how the compensation of both effects also leads to large amplitude wakefields (> 1 GV/m) with constant phase for a long distance (> 100 m).

I propose an experimental setup in which the effect of the self-modulation from the bunch front on the bunch rear is measured. By using both the relativistic ionization front and an electron bunch two different parts of the bunch self-modulate with different growth rates. I show that when the electron bunch charge is high enough, even if it is expelled from the wakefields before the proton bunch modulation starts, the momentum imprint given by the seed wakefields can set the phase of the modulation. Furthermore, I show that an interesting effect occurs in the transition between seeding with the relativistic ionization front and the electron bunch: when the modulation growth rate in the rear is faster than in the front and the modulations are out of phase, there is charge loss in the microbunch train formed earlier in the rear, effect which could be measured in the experiment. Unfortunately this effect cannot be measured currently in the experiment as explained in what follows.

I show with simulations for the first time that the response of the plasma to a long proton bunch propagating through a plasma density ramp has detrimental effects on a co-propagating electron bunch. The charge loss of an injected electron bunch predicted in simulations was confirmed by experimental results. In the low-density region of the ramp, where the local plasma density is much lower than the bunch density, the non-linear response of the plasma to the proton bunch is to form a high-density plasma electron filament on axis. This filament sustains defocusing fields for negatively charged particles. Those fields, contrary to the fields in a blow-out of plasma electrons, have a complex dependence on the transverse position, thus, the matching condition is not met.

An electron bunch injected within the proton bunch might be completely expelled from the axis before reaching the plasma with constant density, such as is the case for the 19 MeV electron bunch used for seeding self-modulation. On the contrary, a positron bunch with the same properties as the seed electron bunch, is focused and reaches the constant-density plasma without charge loss.

A microbunch train propagating through the plasma ramp also produces a non-linear plasma response and leads to the formation of a high-density filament on axis, although with properties corresponding to the response to an unmodulated bunch with lower initial density. The emittance of a 150 MeV bunch injected for acceleration increases by at least one order of magnitude and the bunch loses more than half of its initial charge. This is true for both positron and electron bunches. A plasma ramp leading to the long accelerating plasma must be avoided in a plasma wakefield accelerator relying on a positively charged microbunch train as driver. AWAKE avoids this in the accelerator plasma with the choice of a counter-propagating laser pulse to ionize the Rb vapor. This thesis discusses only up-ramps, thus, further work can be done on down-ramps existing at the plasma exit, which may also have detrimental effects on accelerated bunches, despite their expected large energy (GeV). This topic must be addressed to ensure that accelerated bunches have low emittance, so that they are suitable for applications. Furthermore, future work can also study the transverse dependence on the density in the plasma ramp.

The results shown in this thesis contribute to the understanding of the physics of a plasma wakefield accelerator relying on the self-modulation of a relativistic long bunch that is used as driver. Modifying the plasma density makes it possible to study different aspects of the plasma response and of self-modulation. The understanding of the details behind self-modulation allows for its control. Controlling self-modulation leads to the goal of producing high-quality electron bunches with TeV of energy per electron, by accelerating them for a long distance in high-amplitude wakefields with constant phase velocity.

Appendices

A Convergence and Validity Tests

Convergence tests are done to ensure that the results are independent of the simulation parameters. Since the parameters for the simulations I perform were based on previous simulations and published work (e.g., [80]), a resolution test in space and time and macroparticle number is enough to confirm the validity of the results. The parameters I test are the spatial resolution of the grid (longitudinal $d\xi$ and transverse dx), the time step resolution (dt), and the number of bunch (N_b) or plasma electron (N_e) macroparticles. The baseline parameters for each of the next sections are found in their respective chapter.

A.1 Frequency and amplitude of the seed wakefields

For the LCODE simulations in chapter 2 (Table 2.1), I test $d\xi$ and dx simultaneously (Fig. A.1), N_b and N_e (Fig. A.2). Convergence of dt is not needed since the simulations were obtain only at $z = 0$ m with LCODE, which means that I simulate just one time. I measure the frequency of the transverse wakefields. For all parameters, the maximum relative difference between the baseline and doubling the parameters is < 1 %. The baseline parameters are sufficient to reproduce the change in f_s according to n_{b0}.

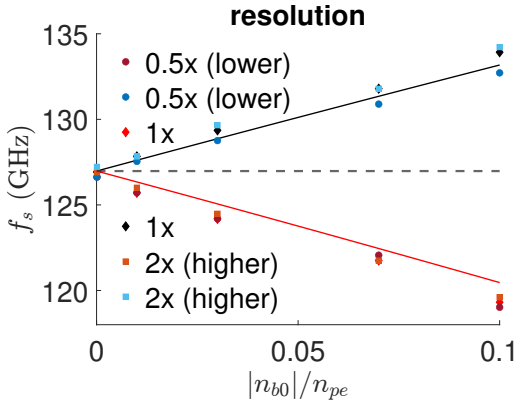

Figure A.1: Frequency of the initial transverse wakefields f_s (peak of the power spectrum) considering a lineout at $x = 0.1$ mm in the range $\xi = 0$ to 250 ps for various proton (black) and antiproton (red) bunch densities n_{b0}. Results of halving and doubling $d\xi$ and dx simultaneously.

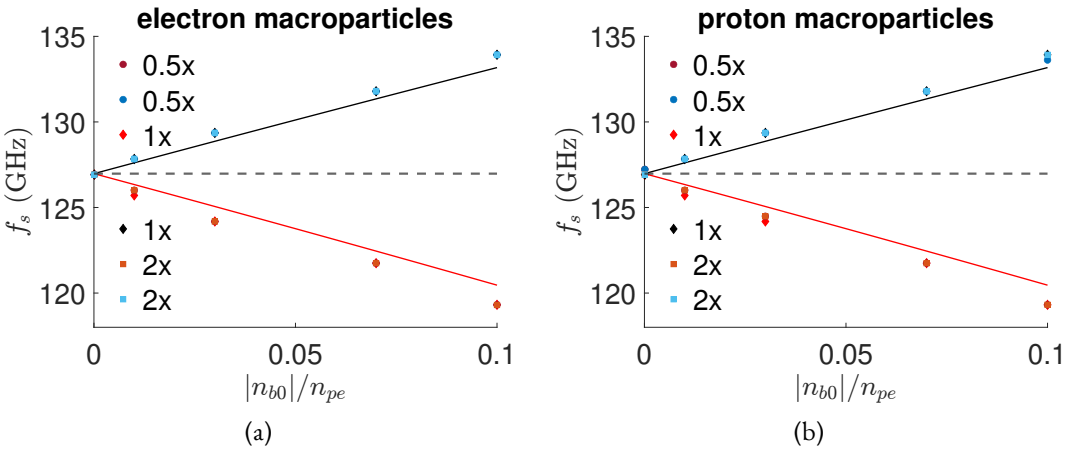

Figure A.2: Frequency of the initial transverse wakefields f_s (peak of the power spectrum) considering a lineout at $x = 0.1$ mm in the range $\xi = 0$ to 250 ps for various proton (black) and antiproton (red) bunch densities n_{b0}. Results of halving and doubling (a) N_e and (b) N_b.

A.2 Self-modulation in plasma with density gradients

For the OSIRIS simulations in chapter 3 (Table 3.1), I test $d\xi$, dx, N_e, and N_b. I measure the modulation frequency f_{mod} across the bunch, the mean amplitude of the transverse wakefields along the plasma, and the microbunch train profile at the plasma end $z = 0$ m. The first and last points are compared with experimental data in chapter 3, where they show good agreement. The time step satisfies the Courant condition (Eq. 1.29).

In Fig. A.3, the maximum relative difference in f_{mod} between the baseline and doubling the values is $< 0.3\,\%$. The points that show a larger difference belong to the case where the parameters are halved. In Fig. A.4, the amplitude of the transverse wakefields along the plasma is in agreement among all the parameters.

The microbunches are in the same positions in ξ and have a similar amount of charge both by changing the spatial resolution (Fig. A.5) and number of macroparticles (Fig. A.6).

The parameters are sufficient to reproduce the results in chapter 3.

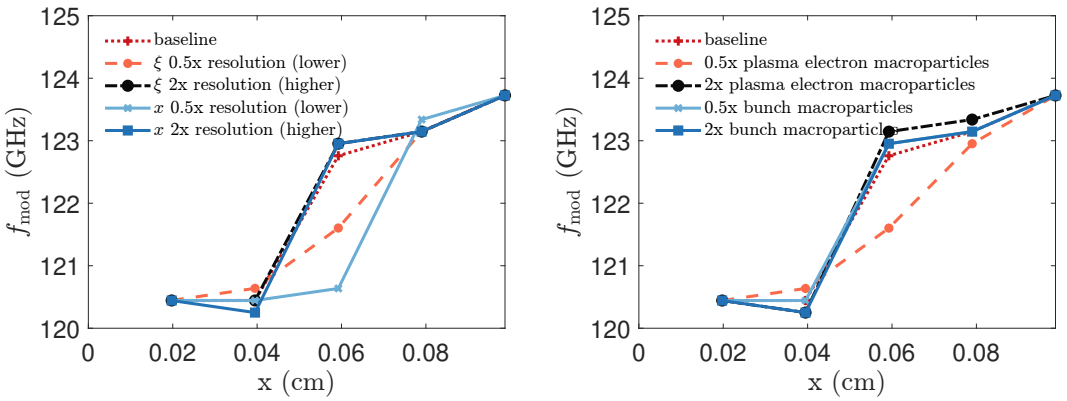

Figure A.3: Modulation frequency f_{mod} in $c/\omega_{pe} = 0.395$ mm-wide slices across the bunch for $g = 0$ %/m. Results of halving and doubling (a) $d\xi$ and dx and (b) N_e and N_b.

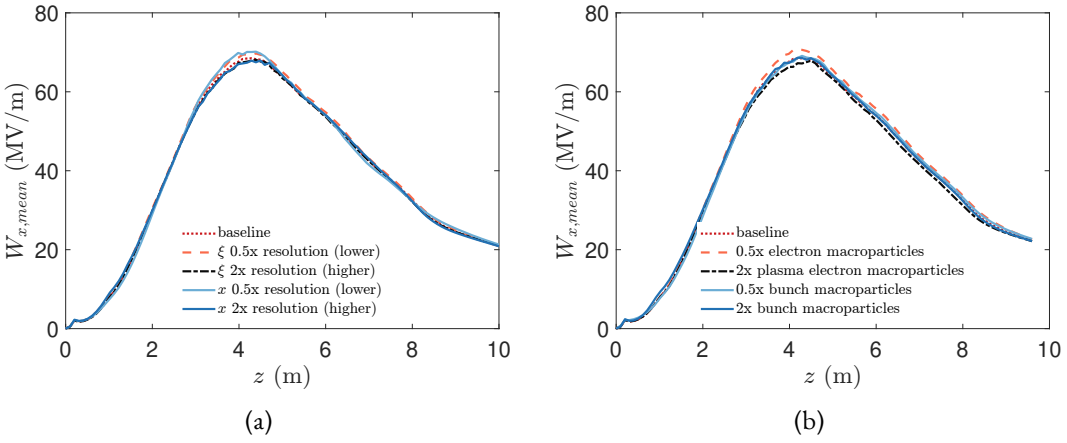

Figure A.4: Mean amplitude of the defocusing wakefields, averaged over the whole simulation window, along z for $g = 0$ %/m. Results of halving and doubling (a) $d\xi$ and dx and (b) N_e and N_b.

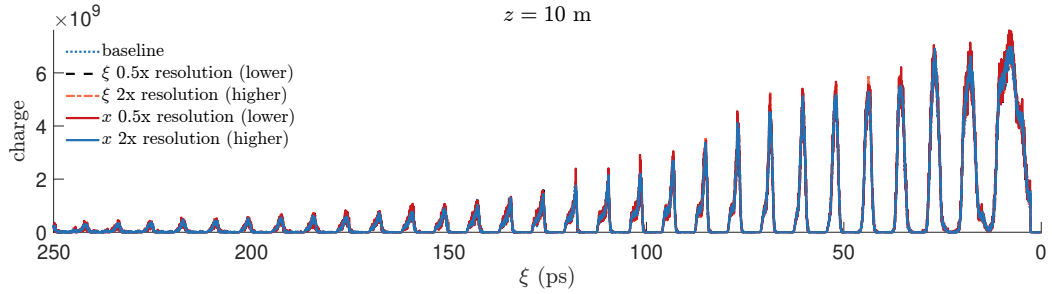

Figure A.5: Profiles of the modulated bunch with $g = 0\,\%/\mathrm{m}$, obtained by integrating the bunch density within $x < \sigma_{r,\mathrm{screen}} = 0.536\,\mathrm{mm}$. Results of halving and doubling $d\xi$ and dx.

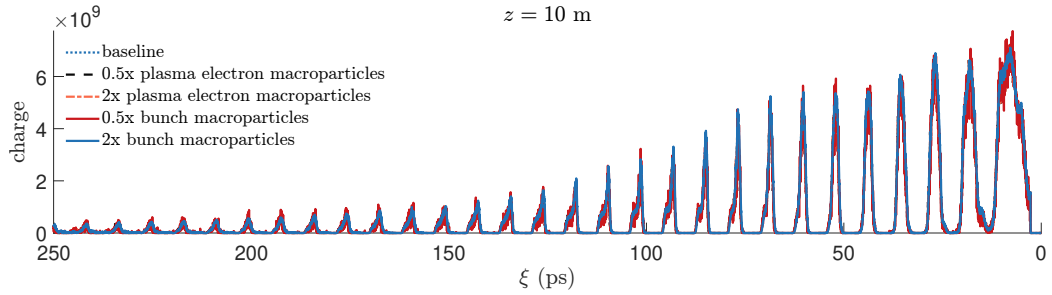

Figure A.6: Profiles of the modulated bunch with $g = 0\,\%/\mathrm{m}$, obtained by integrating the bunch density within $x < \sigma_{r,\mathrm{screen}} = 0.536\,\mathrm{mm}$. Results of halving and doubling N_e and N_b.

A.3 Self-modulation with two seeds: electron bunch and density cut

For the LCODE simulations in chapter 4 (Table 4.1), I test $d\xi$ and dx simultaneously, dt, N_e, and N_b. I measure the profile of the microbunch train and a lineout of the wakefields by the end of the plasma $z = 10\,\mathrm{m}$. The main features are reproduced also with the higher transverse resolution (continuous blue and red lines in Figs. A.7 and A.9). Changing the temporal resolution (orange and black lines in Figs. A.7 and A.9) and the number of macroparticles (Figs. A.8 and A.10) has no effect on the microbunch train profile and lineout of the wakefields. The parameters are sufficient to reproduce the bunch modulation.

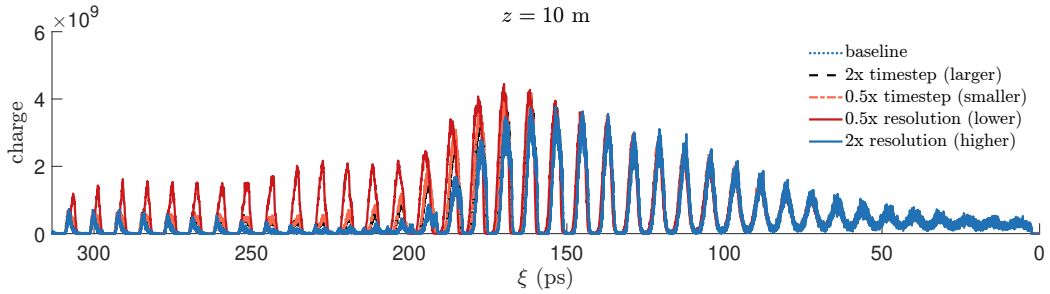

Figure A.7: Profiles of the modulated bunch, obtained by integrating density values in simulations, within $x < \sigma_r = 0.02$ mm. Results of halving and doubling $d\xi$ and dx simultaneously and dt.

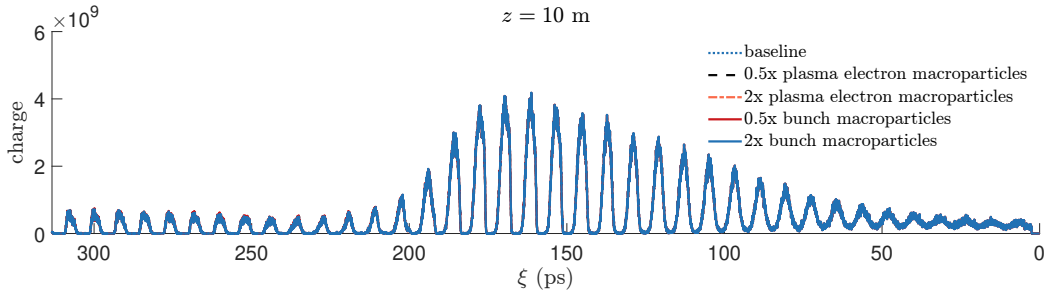

Figure A.8: Profiles of the modulated bunch, obtained by integrating density values in simulations, within $x < \sigma_r = 0.02$ mm. Results of halving and doubling N_e and N_b.

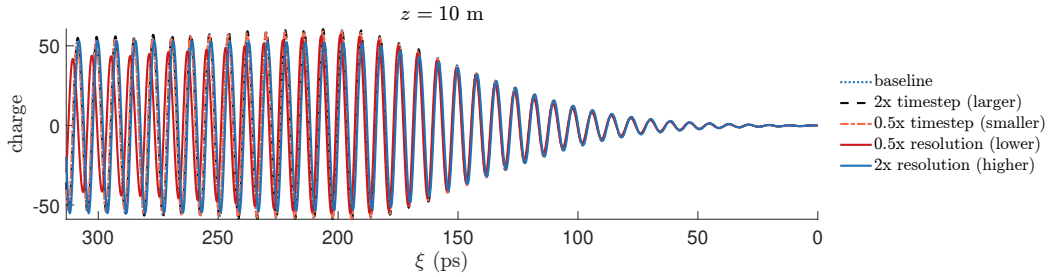

Figure A.9: Profiles of a lineout of the transverse wakefields at $x = \sigma_r = 0.02$ mm. Results of halving and doubling $d\xi$ and dx simultaneously and dt.

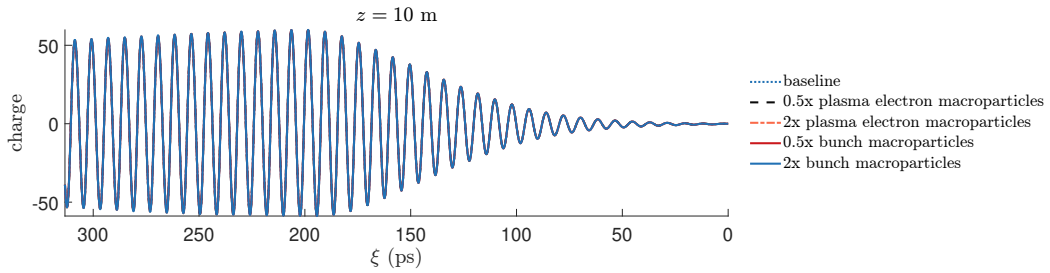

Figure A.10: Profiles of a lineout of the transverse wakefields at $x = \sigma_r = 0.02$ mm. Results of halving and doubling N_e and N_b.

A.4 Influence of a plasma density ramp on electron bunch injection

For the LCODE simulations in chapter 5, I use different densities. In all cases, I test $d\xi$ and dx simultaneously, dt, N_e, and N_b. For $n_{pe} = 2 \times 10^{14}\,\mathrm{cm}^{-3}$ (Tables 5.1 and 5.2), I measure the charge loss of the seed electron bunch and the mean amplitude of the transverse wakefields along the plasma ramp up to 1 m into the plasma ($z = -1$ to 1 m). For $n_{pe} = 7 \times 10^{14}\,\mathrm{cm}^{-3}$ (Tables 5.1 and 5.3), I first measure the formation of the microbunch train in the first plasma by looking at the charge profile of the microbunch train at $z = 10$ m. Then I measure the charge loss and normalized emittance growth of the injected bunches for acceleration. I finally measure for $n_{pe} = 1{\times}10^{14}\,\mathrm{cm}^{-3}$ (Table 5.4) the mean transverse fields.

A.4.1 First plasma, low density

Figures A.11 and A.12 show that for $n_{pe} = 2{\times}10^{14}\,\mathrm{cm}^{-3}$ all charge is lost before the plasma entrance in all cases and the amplitude of the fields is approximately the same in all cases. Therefore, the baseline parameters are sufficient to reproduce the charge loss and fields.

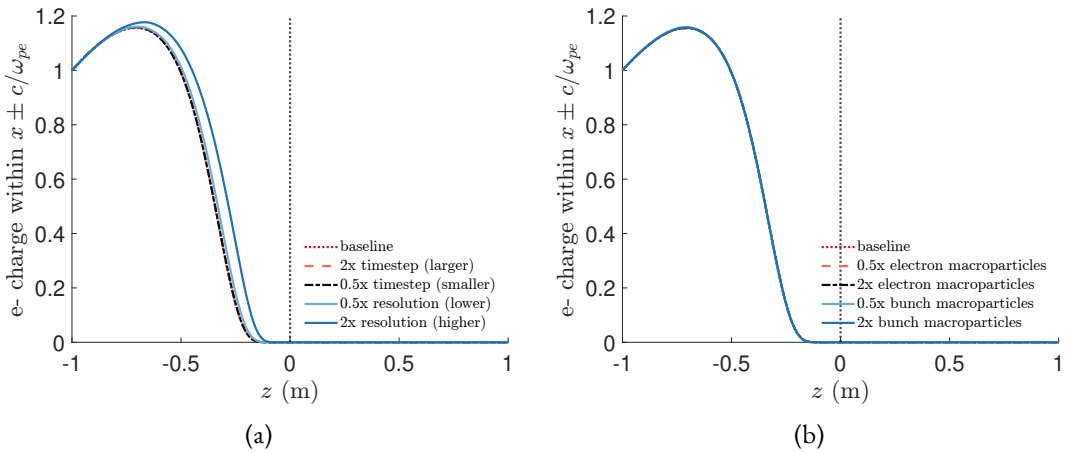

Figure A.11: Charge evolution of a seed electron bunch propagating through the plasma ramp. Charge is calculated by integrating the density in $|x| < c/\omega_{pe} = 0.376\,\text{mm}$. A value of 1 indicates the amount of charge within $|x| < c/\omega_{pe}$ at $z = -1\,\text{m}$. The gray vertical line indicates the position of the plasma entrance. Results of halving and doubling (a) $d\xi$ and dx simultaneously and dt and (b) N_e and N_b.

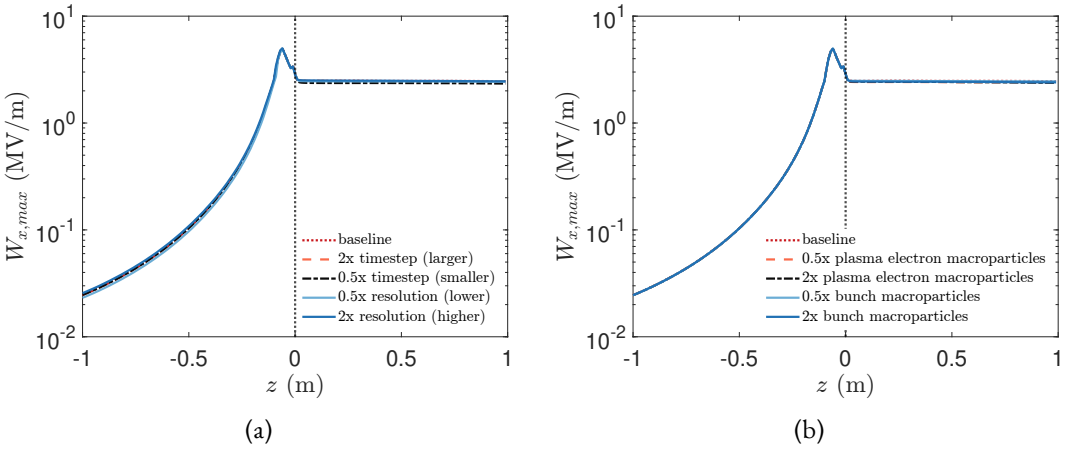

Figure A.12: Maximum amplitude of the transverse wakefields in $\xi < 67$ ps for a proton and a seed electron bunch propagating co-axially. The gray vertical line indicates the position of the plasma entrance. Results of halving and doubling (a) $d\xi$ and dx simultaneously and dt and (b) N_e and N_b.

A.4.2 Plasma with density step, high density

Figures A.13 and A.14 show that for $n_{pe} = 7 \times 10^{14}\,\mathrm{cm}^{-3}$, the proton bunch that propagated through 10 m of plasma with a density step transformed into a microbunch train. The microbunches are in the same positions along ξ and have approximately the same charge, therefore the baseline parameters are sufficient.

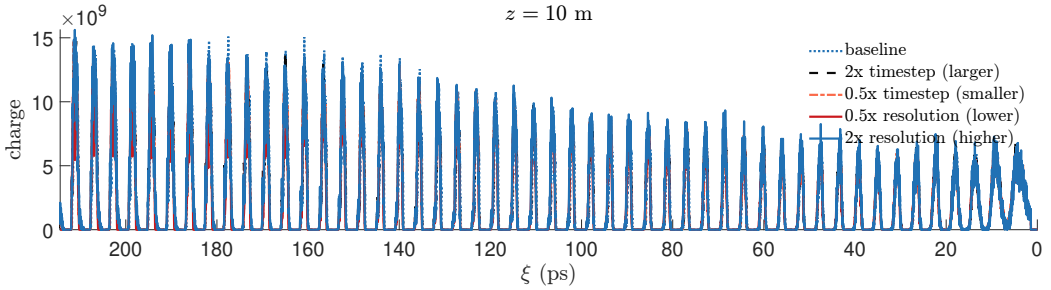

Figure A.13: Profiles of the modulated bunch after propagating through a plasma with density step, obtained by integrating density values within $x < \sigma_r = 0.02\,\mathrm{mm}$. Results of halving and doubling $d\xi$ and dx simultaneously and dt.

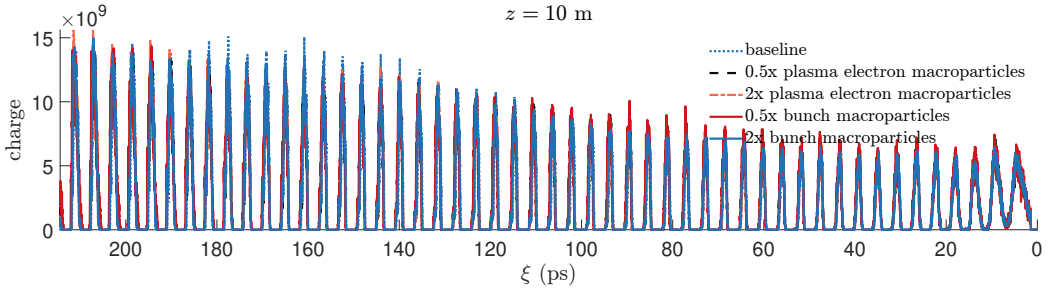

Figure A.14: Profiles of the modulated bunch after propagating through a plasma with density step, obtained by integrating density values within $x < \sigma_r = 0.02\,\mathrm{mm}$. Results of halving and doubling N_e and N_b.

A.4.3 Second plasma, high density

Figure A.15(a) shows that the charge loss of an electron bunch for acceleration in the second plasma, where $n_{pe} = 7 \times 10^{14}\,\mathrm{cm}^{-3}$, is independent of $d\xi$, dx, and dt. Figure A.15(b) shows that it varies slightly with N_e and N_b. In all cases there is a large charge loss and the fraction remaining is < 0.18. Therefore, the baseline parameters are sufficient to show the charge loss.

Figure A.16(a) shows that the normalized emittance is also unaffected by $d\xi$, dx, and dt. Here it is important to note that the line appears broken because all charge left the region around the axis before the plasma entrance, so that there was no emittance to measure in that region. Nevertheless,

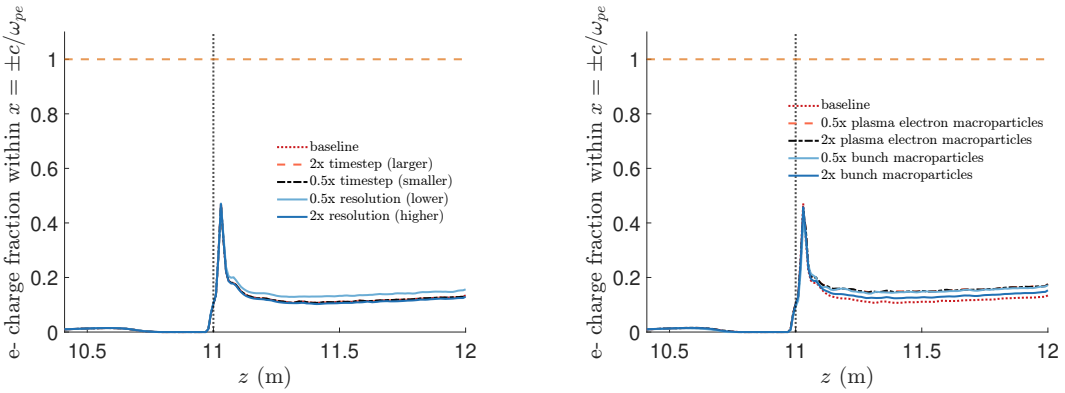

Figure A.15: Charge evolution of an electron bunch for acceleration propagating through the plasma ramp. Charge is calculated by integrating the density in $|x| < c/\omega_{pe} = 0.376\,\mathrm{mm}$. A value of 1 indicates the total amount of charge. The gray vertical line indicates the position of the plasma entrance. Results of halving and doubling (a) $d\xi$ and dx simultaneously and dt and (b) N_e and N_b.

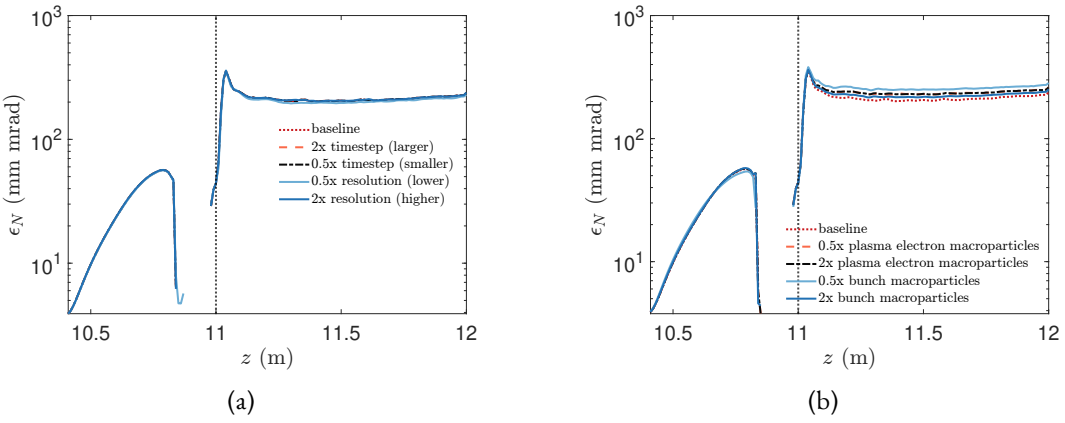

Figure A.16: Normalized emittance evolution of an injected electron bunch for acceleration propagating through the plasma ramp. The gray vertical line indicates the position of the plasma entrance. Results of halving and doubling (a) $d\xi$ and dx simultaneously and dt and (b) N_e and N_b.

a fraction still in the plasma comes back to axis due to focusing fields just as the bunches propagate trough the plasma entrance. The emittance varies slightly with N_e and N_b, although in all cases it is > 100 mm mrad, an increase of more than one order of magnitude. Therefore, the baseline parameters are sufficient to show the large emittance increase.

A.4.4 First plasma, Run 2b

The next tests are related to AWAKE run 2b, in which an injected electron bunch in the first plasma will be used to probe the amplitude of the wakefields. The average of the fields along the ramp, obtained as explained in section 5.7, show that there are focusing fields at the back of the bunch. For these tests I only decrease the values of the parameters, since the results do not change. Figures A.17, A.18, A.19, A.20, and A.21 show that the average fields and the lineout are independent to a decrease in the parameters. All cases agree with each other, and show the focusing fields at the same position in the bunch rear (visible in the green lineouts at $\xi > 800$ ps). Therefore, the baseline parameters are sufficient.

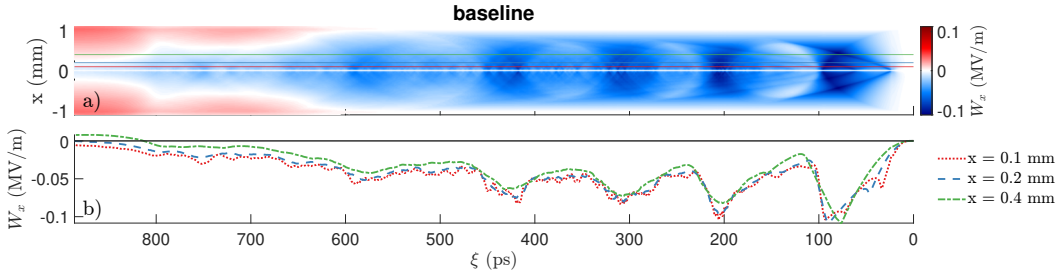

Figure A.17: Baseline. (a) Average transverse fields sustained by the plasma electrons (see Sec. 5.7), mirrored about the axis (2D axisymmetric geometry). Fields with negative amplitude attract positively charged particles to the axis. (b) Lineouts of the transverse fields in (a) at various transverse distances.

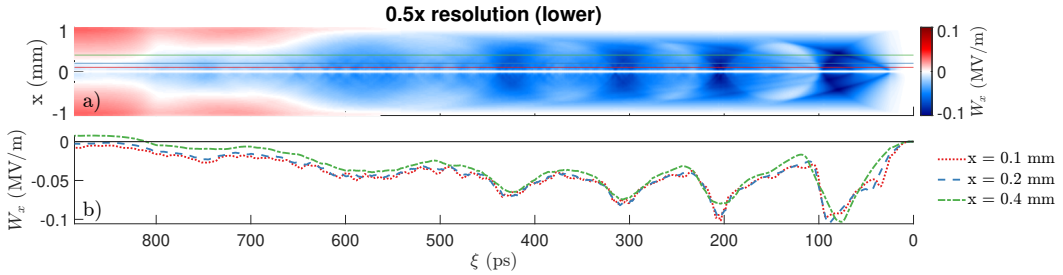

Figure A.18: Low resolution (a) Average transverse fields sustained by the plasma electrons (see Sec. 5.7), mirrored about the axis (2D axisymmetric geometry). Fields with negative amplitude attract positively charged particles to the axis. (b) Lineouts of the transverse fields in (a) at various transverse distances.

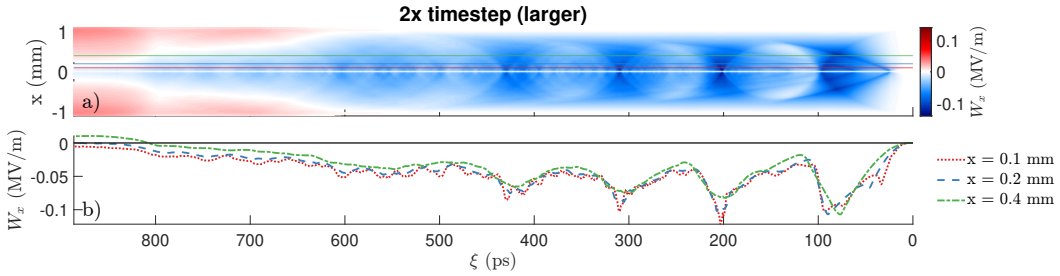

Figure A.19: Long time step. (a) Average transverse fields sustained by the plasma electrons (see Sec. 5.7), mirrored about the axis (2D axisymmetric geometry). Fields with negative amplitude attract positively charged particles to the axis. (b) Lineouts of the transverse fields in (a) at various transverse distances.

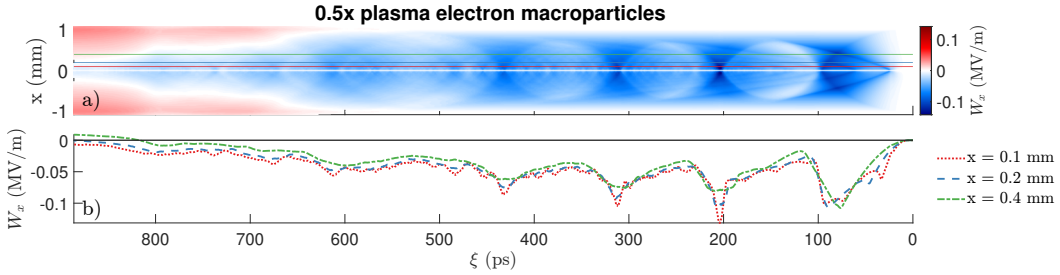

Figure A.20: Fewer plasma electron macroparticles. (a) Average transverse fields sustained by the plasma electrons (see Sec. 5.7), mirrored about the axis (2D axisymmetric geometry). Fields with negative amplitude attract positively charged particles to the axis. (b) Lineouts of the transverse fields in (a) at various transverse distances.

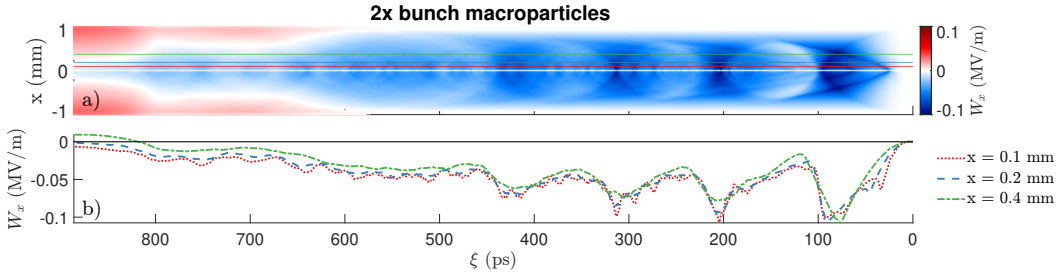

Figure A.21: Fewer bunch macroparticles. (a) Average transverse fields sustained by the plasma electrons (see Sec. 5.7), mirrored about the axis (2D axisymmetric geometry). Fields with negative amplitude attract positively charged particles to the axis. (b) Lineouts of the transverse fields in (a) at various transverse distances.

B Self-Modulation in Plasma with Density Gradients

The figures in this appendix were obtained with the method and parameters from chapter 3. Figures B.1, B.2, and B.2 show waterfall plots of the microbunch trains, calculated by integrating the density of the proton bunch in $|x| < \sigma_r = 0.2\,\text{mm}$.

The progressive increase of the size among microbunches from positive to negative gradients is seen in (c)(f)(i) of Figs. B.1, B.2, and B.2. Figures B.1(b)(e)(h); B.2(b)(e)(h); and B.2(b)(e)(h) show how the charge of the microbunches is lost at progressively larger distances along the plasma as the gradient goes from negative to positive. A maximum amount of charge for each microbunch reaches the plasma end with $g = +0.5\,\%/\text{m}$ that is displayed in Figs. B.2(d)-(f).

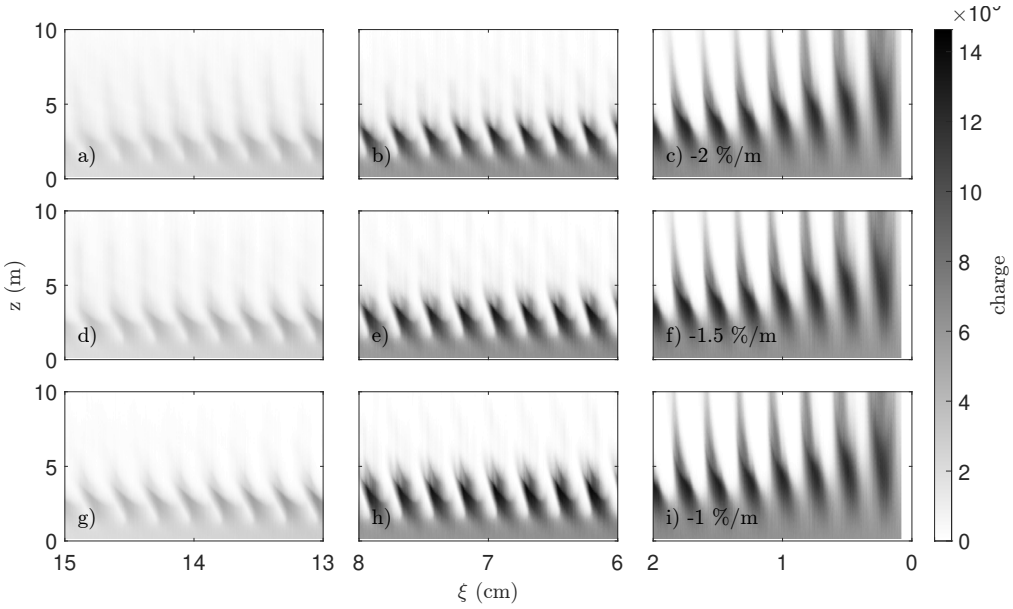

Figure B.1: Waterfall plots of the microbunch train by integrating the density in $|x| < 0.2\,\text{mm}$ around $\xi_0 =$ 1, 7, and 14 cm for $g = -2\,\%/\text{m}$ (a-c), $g = -1.5\,\%/\text{m}$ (d-f), and $g = -1\,\%/\text{m}$ (g-i).

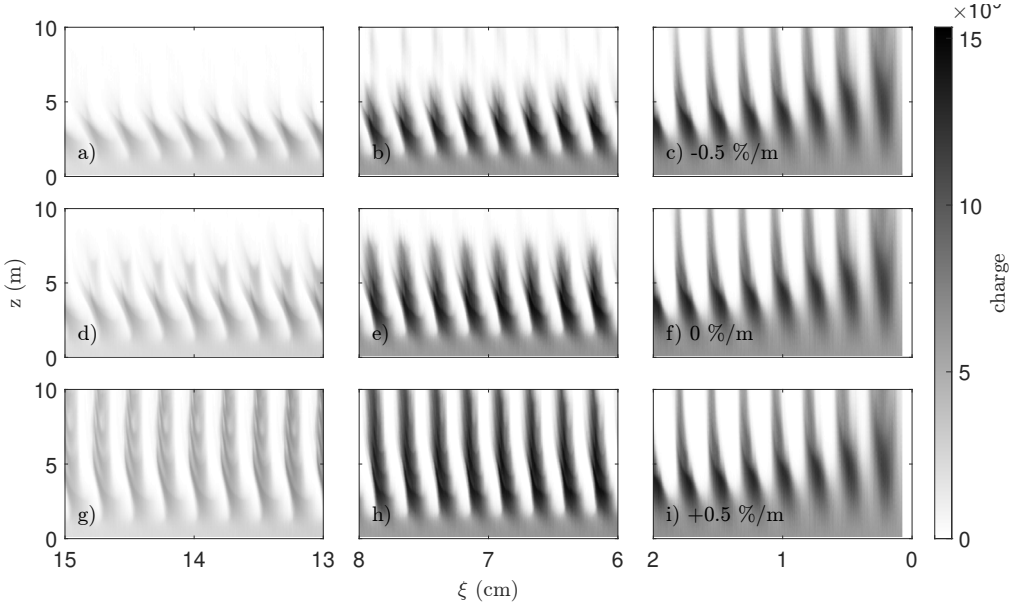

Figure B.2: Waterfall plots of the microbunch train by integrating the density in $|x| < 0.2$ mm around $\xi_0 =$ 1, 7, and 14 cm for $g = -0.5$ %/m (a-c), $g = 0$ %/m (d-f), and $g = +0.5$ %/m (g-i).

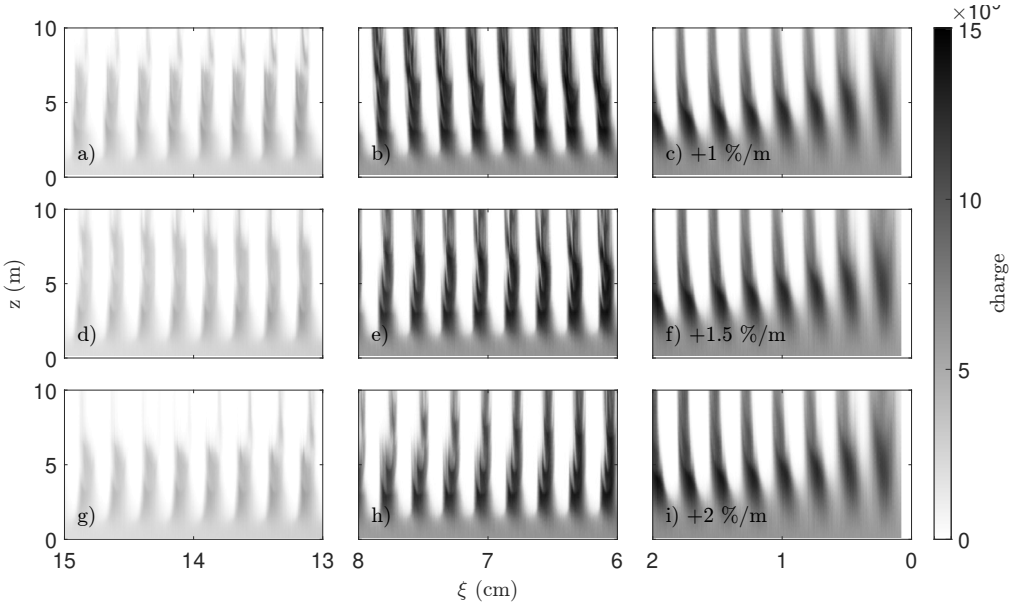

Figure B.3: Waterfall plots of the microbunch train by integrating the density in $|x| < 0.2$ mm around $\xi_0 =$ 1, 7, and 14 cm for $g = +1$ %/m (a-c), $g = +1.5$ %/m (d-f), and $g = +2$ %/m (g-i).

Figure B.4 shows an alternative display of the information in Figs. 3.3, 3.4, and 3.5 in chapter 3 that includes the dephasing and amplitude of the fields and the charge of the microbunch at each ξ_0.

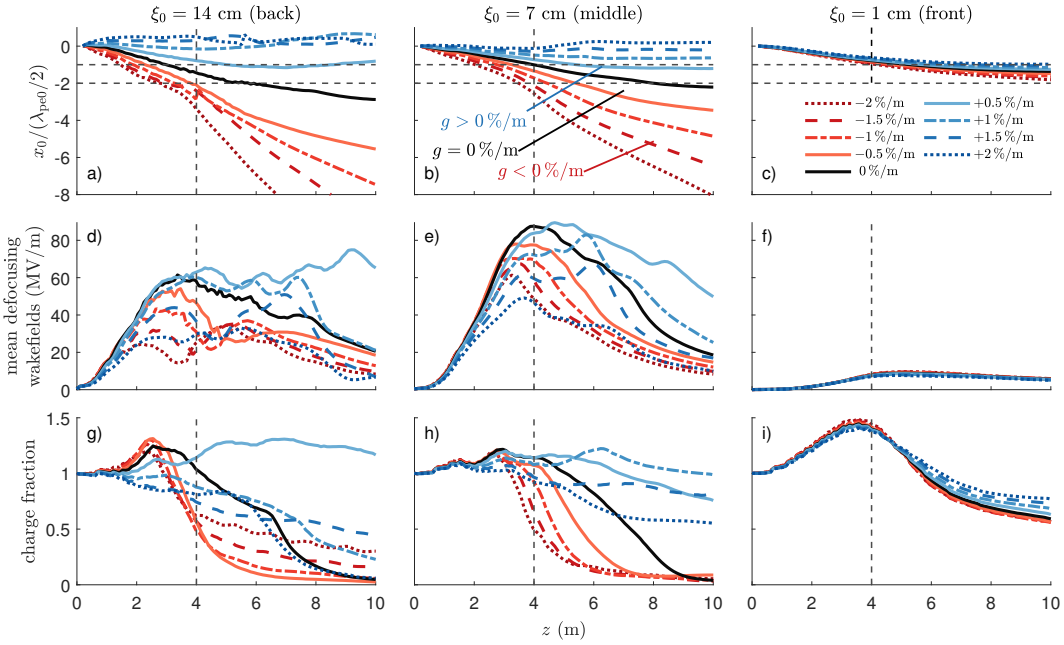

Figure B.4: (a)-(c) Position x_0 of the zero-crossing of the longitudinal wakefields on axis, normalized to half the initial plasma wavelength $\lambda_{pe0}/2$. (d)-(f) Mean amplitude of the defocusing wakefields within $\xi_0 \pm \lambda_{pe}(z)/2$. (f)-(i) Charge fraction within $\xi_0 \pm \lambda_{pe}(z)/2$ and within one $\sigma_r(z)$. All quantities plotted as a function of z starting at three positions along the bunch: $\xi_0 = 1$ cm, $\xi_0 = 7$ cm, and $\xi_0 = 14$ cm. Horizontal dashed lines: $-1(\lambda_{pe0}/2)$ and $-2(\lambda_{pe0}/2)$. Vertical dashed lines: position of the peak in the mean defocusing wakefields for $g = 0$ %/m (see Fig. 3.7 in chapter 3). Each set of curves in (g)-(i) is normalized to the charge within $\pm\lambda_{pe}(z)/2$ and $\sigma_r(z)$ of the unmodulated proton bunch. The initial charge values ($z = 0$ m) are: 235, 608, and 617 pC respectively. I published this figure previously in [49].

Figure B.5 shows the evolution of the longitudinal wakefields, both along ξ and z, around three positions ξ_0 along the bunch: one close to the seeding position $\xi_0 = 1$ cm, i.e., very early in the wakefields, and then at $\xi_0 = \sigma_z$ and $\xi_0 = 2\sigma_z$, i.e., late in the wakefields. From these waterfall plots one can follow the phase of the wakefields. The plots are built by taking a lineout of the wakefields on axis and stacking them from the bottom ($z = 0$ m) to the top ($z = 10$ m). The zero-crossing of the fields is taken as the phase of the wakefields around that position in ξ. Together with the longitudinal wakefields, I include the position of the microbunch formed closest to each ξ_0 in each plot, marked by the green line. The opacity of the line is proportional to the peak value of the charge profile of each microbunch, calculated by integrating the density profile in $|x| < 0.2$ mm, normalized to its maximum value along z. When the line is fully transparent, the microbunch charge has been completely expelled from the region $|x| < 0.2$ mm around the axis.

In Fig. B.5, $v_b \approx c$ is a vertical line. Zero-crossing lines with a negative slope have a subluminal v_{ph}, and lines with positive slope have a superluminal v_{ph}. When green lines are not vertical,

it means that charge is being expelled from the front/back of the microbunch and brought towards the axis to the back/front by the transverse wakefields, so that the microbunch position (the position with the largest amount of charge) changes.

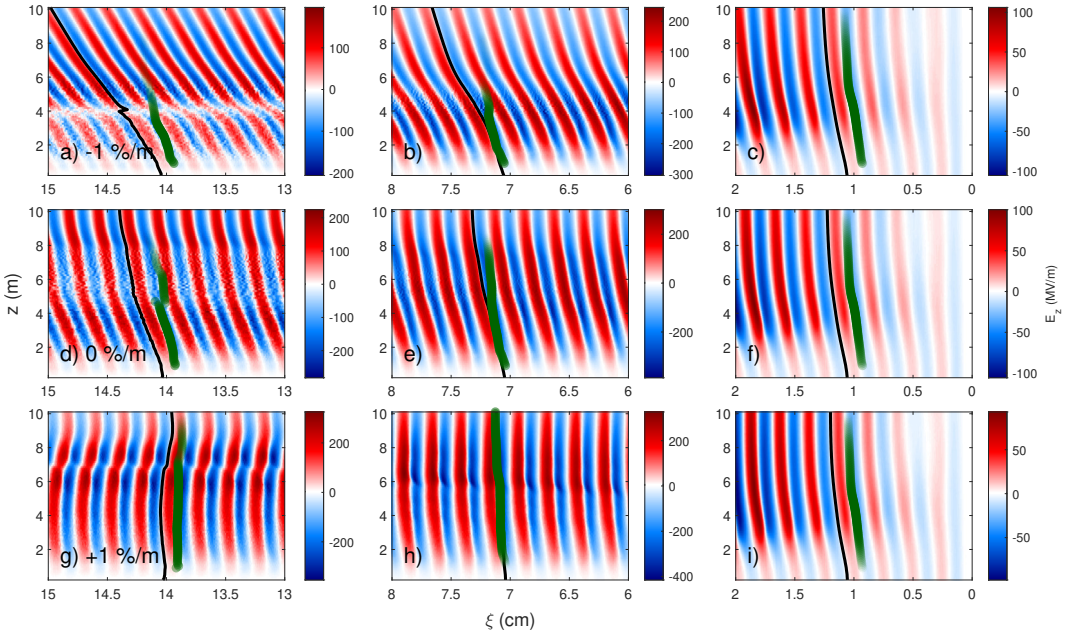

Figure B.5: Waterfall plots of the longitudinal wakefields on axis around three positions along the bunch: $\xi_0 = 1$, 7, and 14 cm for three g: $g = -1$ %/m (a)-(c), $g = 0$ %/m (d)-(f), and $g = +1$ %/m (g)-(i). Black lines: a zero-crossing of the fields. Green lines are located at the position of the peak of the charge profile of the microbunch formed closest to each ξ_0. The opacity of the green line corresponds to the value of the peak, normalized to its maximum value along z. I published this figure previously in [91].

C Lists of Publications and Conferences

C.1 List of publications

P. Muggli, P. I. Morales Guzmán, A. Bachmann, M. Hüther, M. Moreira, M. Turner, J. Vieira, *Seeding self-modulation of a long proton bunch with a short electron bunch*, IOP Publishing Ltd, 4th European Advanced Accelerator Concepts Workshop (2020)

P. I. Morales Guzmán, J. Vieira, P. Muggli, AWAKE Collaboration, *PIC Simulations of the Seeded Self-Modulation of a Long Proton Bunch in Plasma Density Gradients*, European Physical Society, 47th EPS Conference on Plasma Physics (2020)

P. I. Morales Guzmán, P. Muggli, AWAKE Collaboration, *Simulation and experimental study of proton bunch self-modulation in plasma with linear density gradients*, Phys. Rev. Accel. Beams 24 101301 (2021)

P. I. Morales Guzmán, P. Muggli, *PIC Simulations of the Interaction between Self-Modulation in the Front and Rear of a relativistic Proton Bunch in Plasma*, European Physical Society, 48th EPS Conference on Plasma Physics (2022)

C.2 List of conference talks

Numerical Study of Self-Modulation with Plasma Density Gradients, 62nd Annual Meeting APS Plasma, online (2020)

Modulation Frequency of a Proton Bunch in Plasmas With Density Gradients, IPAC 21, online (2021)

Numerical simulation study of the propagation of a short electron bunch and a long proton bunch in a plasma ramp, EuroNNAc Special Topics Workshop, Italy (2022)

Influence of plasma profile on injection dynamics in a proton-driven wakefield accelerator, Deutsche Physikalische Gesellschaft Sektion Materie und Kosmos, Germany (2023)

C.3 List of conference posters

Numerical Study of Self-Modulation with Plasma Density Gradients, AAC Seminar Series, online (2020)

PIC Simulations of the Seeded Self-Modulation of a Long Proton Bunch in Plasma Density Gradients, 47th EPS Conference on Plasma Physics, online (2021)

PIC Simulations of the Self-Modulation of a Long Proton Bunch using two seeds: an Electron Bunch and a Density Cut, Science and Applications of Plasma-Based Accelerators 767. WE-Heraeus-Seminar, Germany (2022)

PIC Simulations of the Interaction between Self-Modulation in the Front and Rear of a relativistic Proton Bunch in Plasma, 48th EPS Conference on Plasma Physics, online (2022)

Numerical simulation study of the propagation of a short electron bunch and a long proton bunch in a plasma ramp, EuroNNAc Special Topics Workshop, Italy (2022)

Numerical study of non-linear plasma response to a long proton bunch and its effect on an electron bunch, Laser and Plasma Accelerator Workshop, Portugal (2023)

C.4 List of internal talks

AWAKE Run 2 and Density Gradient Studies, Collaboration Meeting, CERN, Switzerland (2019)

Simulations of the Self-Modulation of a Long Proton Bunch using Plasmas with Linear Density Gradients, Collaboration Meeting, online (2020)

Proton Bunch Modulation Frequency in Plasmas with Linear Density Gradients, Collaboration Meeting, online (2021)

Advanced Proton Driven Plasma Wakefield Acceleration Experiment (AWAKE), IMPRS Colloquium, Max Planck Institute for Physics, Germany (2021)

Electron Bunch Seeding from Inside the Proton Bunch, Collaboration Meeting, online (2022)

The AWAKE Experiment and Simulations of Self-Modulation, Ringberg Workshop, Germany (2022)

Numerical simulation study of the propagation of an electron bunch and proton bunch in a plasma ramp, Collaboration Meeting, CERN, Switzerland (2022)

Proton-driven plasma-based acceleration in AWAKE, IMPRS Colloquium, Max Planck Institute for Physics, Germany (2023)

Acronyms

AWAKE	Advanced Wakefield Experiment
CERN	Conseil Européen pour la Recherche Nucléaire
CLIC	Compact Linear Collider
DESY	Deutsches Elektronen-Synchrotron
DFT	discrete Fourier transform
e+SSM	positron bunch seeded self-modulation
eSSM	electron bunch seeded self-modulation
FEL	free electron laser
ILC	International Linear Collider
LHC	Large Hadron Collider
LWFA	laser wakefield accelerator
OTR	optical transition radiation
PIC	particle-in-cell
PWFA	plasma wakefield accelerator
RIF	relativistic ionization front
rms	root mean square
SM	self-modulation
SMI	self-modulation instability
SPS	Super Proton Synchrotron
SSM	seeded self-modulation

Acknowledgements

Since a very young age, I always had the goal of being a PhD, in this field that I enjoyed the most since then: physics, and to expand the frontier of knowledge. The road to reach that goal has not been easy, and I had to make sacrifices, but I am glad I have reached it and I am excited to see what follows. This work concludes my four-ish year journey as a doctoral researcher. In the studies here presented, I distilled countless hours in front of the computer and discussing with colleagues at the Max Planck Institute, CERN, or from home. I received help and guidance from various sources, which improved both my research and my ability to do it. Here I want to express my gratitude to those people who have accompanied me through the ups and downs of my PhD campaign.

I would like to thank my supervisor Patric Muggli for giving me the chance of achieving my goals and for the feedback he has given to my published work, which ultimately lead to improvement. I thank Patric also for showing me the many facets of science.

I want to express my gratitude to my university supervisor Allen Caldwell for supervising and supporting me, making it possible to do my work, in particular by providing funding especially after my scholarship ended, a critical element for a foreigner in Germany like me.

I thank John "Plasma" Farmer for his many advices in the use of particle-in-cell codes and academic life and for his eagerness to go grab a beer on occasion.

I thank Mariana for introducing me to OSIRIS and enabling my first steps in plasma wakefield simulations.

I thank Jan and Tatiana, with whom I could share the struggles and fortunes of doing a PhD, for being by my side whenever we could meet. I thank Fabian, Kookjin, and Erwin for also providing a listening ear and bringing good times. I would also like to thank everyone involved in the AWAKE Experiment for enabling the data taking that has given much support and validation to my simulation studies.

Quiero agradecer también a mi familia por estar conmigo durante el doctorado y durante el proceso de escribir mi tesis. Agradezco a mi mamá y mi papá, a mis hermanas Inti e Itzel y mi hermano Emmanuel por apoyarme siempre sin importar el resultado.

I am also grateful to my friends outside of AWAKE, for bringing life into the work-life balance equation and for patiently giving me the support that replenished my motivation to finish my

thesis. Special thanks go to the "Mexican Rim", Litty, Diego, and Toño, for the endless stream of memes and for being prepared to hold me accountable. Thanks to Ricardo for his comprehension about life in academia and in general. Thanks also to my flatmates for keeping track of my PhD over dinner time or over specially brewed coffee. Thanks to the latino community in Munich for bringing me out of the house into the wild every once in a while (hopefully more to come) and special thanks to Elaine for the mostly weekly updates in the Munich café tour.

This work was partially sponsored by the DAAD-CONACyT joint scholarship: Länderbezogenes Kooperationsprogramm mit Mexiko: CONACYT Master, 2016 (57265508), CVU 685109, REGISTRO 600718, SOLICITUD 428642.

Bibliography

1. L. Evans and P. Bryant. "LHC Machine". *Journal of Instrumentation* 3:08, 2008, S08001. DOI: 10.1088/1748-0221/3/08/S08001. URL: https://dx.doi.org/10.1088/1748-0221/3/08/S08001.
2. F.-A. Vincent. *Democritus Among the Abderitans*. [Online; accessed April 16, 2023]. 1790. URL: https://www.britannica.com/biography/Democritus/media/1/157313/227297.
3. V. Shiltsev. "Particle beams behind physics discoveries". *Physics Today* 73:FERMILAB-PUB-20-105-AD-APC, 2020.
4. C. of the Organization. *Convention for the Establishment of a European Organization for Nuclear Research*. [Online; accessed April 17, 2023]. 1953. URL: https://council.web.cern.ch/en/content/convention-establishment-european-organization-nuclear-research.
5. L. Evans and P. Bryant. "LHC Machine. journal of instrumentation, 3". *S08001*, 2008.
6. H. A. Kramers. "XCIII. On the theory of X-ray absorption and of the continuous X-ray spectrum". *The London, Edinburgh, and Dublin Philosophical Magazine and Journal of Science* 46:275, 1923, pp. 836–871.
7. J. M. J. Madey. "Stimulated Emission of Bremsstrahlung in a Periodic Magnetic Field". *Journal of Applied Physics* 42:5, 1971, pp. 1906–1913. DOI: 10.1063/1.1660466. eprint: https://doi.org/10.1063/1.1660466. URL: https://doi.org/10.1063/1.1660466.
8. S. Grundmann, D. Trabert, K. Fehre, N. Strenger, A. Pier, L. Kaiser, M. Kircher, M. Weller, S. Eckart, L. P. H. Schmidt, F. Trinter, T. Jahnke, M. S. Schöffler, and R. Dörner. "Zeptosecond birth time delay in molecular photoionization". *Science* 370:6514, 2020, pp. 339–341. DOI: 10.1126/science.abb9318. eprint: https://www.science.org/doi/pdf/10.1126/science.abb9318. URL: https://www.science.org/doi/abs/10.1126/science.abb9318.

9. R. Mohan. "A review of proton therapy – Current status and future directions". *Precision Radiation Oncology* 6:2, 2022, pp. 164–176. DOI: https://doi.org/10.1002/pro6.1149. eprint: https://onlinelibrary.wiley.com/doi/pdf/10.1002/pro6.1149. URL: https://onlinelibrary.wiley.com/doi/abs/10.1002/pro6.1149.

10. P. Chen, J. M. Dawson, R. W. Huff, and T. Katsouleas. "Acceleration of Electrons by the Interaction of a Bunched Electron Beam with a Plasma". *Phys. Rev. Lett.* 54, 7 1985, pp. 693–696. DOI: 10.1103/PhysRevLett.54.693. URL: https://link.aps.org/doi/10.1103/PhysRevLett.54.693.

11. A. Collaboration. "Experimental Observation of Proton Bunch Modulation in a Plasma at Varying Plasma Densities". *Phys. Rev. Lett.* 122, 5 2019, p. 054802. DOI: 10.1103/PhysRevLett.122.054802. URL: https://link.aps.org/doi/10.1103/PhysRevLett.122.054802.

12. A. Caldwell et al. "Path to AWAKE: Evolution of the concept". *Nuclear Instruments and Methods in Physics Research Section A: Accelerators, Spectrometers, Detectors and Associated Equipment* 829, 2016. 2nd European Advanced Accelerator Concepts Workshop - EAAC 2015, pp. 3–16. ISSN: 0168-9002. DOI: https://doi.org/10.1016/j.nima.2015.12.050. URL: https://www.sciencedirect.com/science/article/pii/S0168900215016307.

13. A. Pukhov, N. Kumar, T. Tückmantel, A. Upadhyay, K. Lotov, P. Muggli, V. Khudik, C. Siemon, and G. Shvets. "Phase Velocity and Particle Injection in a Self-Modulated Proton-Driven Plasma Wakefield Accelerator". *Phys. Rev. Lett.* 107, 14 2011, p. 145003. DOI: 10.1103/PhysRevLett.107.145003. URL: https://link.aps.org/doi/10.1103/PhysRevLett.107.145003.

14. C. B. Schroeder, C. Benedetti, E. Esarey, F. J. Grüner, and W. P. Leemans. "Growth and Phase Velocity of Self-Modulated Beam-Driven Plasma Waves". *Phys. Rev. Lett.* 107, 14 2011, p. 145002. DOI: 10.1103/PhysRevLett.107.145002. URL: https://link.aps.org/doi/10.1103/PhysRevLett.107.145002.

15. M. Brice/CERN. [Online; accessed April 16, 2023]. 2018. URL: https://www.swissinfo.ch/ger/wissen-technik/teilchenbeschleuniger_large-hadron-collider-feiert-10--geburtstag/44386312.

16. D. Mendeleev. "The relation between the properties and atomic weights of the elements". *Journal of the Russian Chemical Society* 1, 1869, pp. 60–77.

17. J. J. T. M. F.R.S. "XL. Cathode Rays". *The London, Edinburgh, and Dublin Philosophical Magazine and Journal of Science* 44:269, 1897, pp. 293–316. DOI: 10.1080/14786449708621070. eprint: https://doi.org/10.1080/14786449708621070. URL: https://doi.org/10.1080/14786449708621070.

18. S. Weinberg. "A Model of Leptons". *Phys. Rev. Lett.* 19, 21 1967, pp. 1264–1266. DOI: 10.1103/PhysRevLett.19.1264. URL: https://link.aps.org/doi/10.1103/PhysRevLett.19.1264.

19. H. Poincaré. "La Voie lactée et la théorie des gaz". *Bulletin de la société astronomique de France* 20, 1906, pp. 153–165.

20. D. Huterer and M. S. Turner. "Prospects for probing the dark energy via supernova distance measurements". *Phys. Rev. D* 60, 8 1999, p. 081301. DOI: 10.1103/PhysRevD.60.081301. URL: https://link.aps.org/doi/10.1103/PhysRevD.60.081301.

21. *Planck reveals an almost perfect Universe*. 2013. URL: https://www.esa.int/Science_Exploration/Space_Science/Planck/Planck_reveals_an_almost_perfect_Universe (visited on 2023).

22. K. von Meyenn. "Ist die Trägheit eines Körpers von seinem Energieinhalt abhängig?" *Albert Einsteins Relativitätstheorie: Die grundlegenden Arbeiten*, 1990, pp. 156–159.

23. P. D. Group et al. "Review of Particle Physics". *Progress of Theoretical and Experimental Physics* 2020:8, 2020. 083C01. ISSN: 2050-3911. DOI: 10.1093/ptep/ptaa104. eprint: https://academic.oup.com/ptep/article-pdf/2020/8/083C01/34673740/rpp2020-vol2-2015-2092_18.pdf. URL: https://doi.org/10.1093/ptep/ptaa104.

24. O. Heaviside. "XXXIX. On the electromagnetic effects due to the motion of electrification through a dielectric". *The London, Edinburgh, and Dublin Philosophical Magazine and Journal of Science* 27:167, 1889, pp. 324–339. DOI: 10.1080/14786448908628362. eprint: https://doi.org/10.1080/14786448908628362. URL: https://doi.org/10.1080/14786448908628362.

25. H. A. Lorentz. "Versuch Einer Theorie der Electrischen und Optischen Erscheinungen in Bewegten Körpern". In: *Collected Papers: Volume V*. Springer Netherlands, Dordrecht, 1937, pp. 1–138. ISBN: 978-94-015-3445-1. DOI: 10.1007/978-94-015-3445-1_1. URL: https://doi.org/10.1007/978-94-015-3445-1_1.

26. M. Altarelli, R. Brinkmann, and M. Chergui. *The European X-ray free-electron laser. Technical design report*. 2007.

27. A. Liénard. *Champ électrique et magnétique produit par une charge électrique concentrée en un point et animée d'un mouvement quelconque*. G. Carré et C. Naud, 1898.

28. C. O'Luanaigh. "First successful beam at record energy of 6.5 TeV", 2015.

29. M. Aicheler, P. Burrows, M. Draper, T. Garvey, P. Lebrun, K. Peach, N. Phinney, H. Schmickler, D. Schulte, and N. Toge. "A Multi-TeV Linear Collider Based on CLIC Technology : CLIC Conceptual Design Report", 2014. DOI: 10.2172/1120127. URL: https://www.osti.gov/biblio/1120127.

30. C. Adolphsen. "The International Linear Collider Technical Design Report - Volume 3.II: Accelerator Baseline Design", 2013. DOI: 10.2172/1347940. URL: https://www.osti.gov/biblio/1347940.

31. A. D. Cahill, J. B. Rosenzweig, V. A. Dolgashev, S. G. Tantawi, and S. Weathersby. "High gradient experiments with *X*-band cryogenic copper accelerating cavities". *Phys. Rev. Accel. Beams* 21, 10 2018, p. 102002. DOI: 10.1103/PhysRevAccelBeams.21.102002. URL: https://link.aps.org/doi/10.1103/PhysRevAccelBeams.21.102002.

32. M. Zuboraj, S. Baryshev, V. Dolgashev, R. Fleming, V. Gorelov, E. Jevarjian, J. Lewellen, M. Middendorf, E. Nanni, M. Schneider, et al. *High Gradient Conditioning and Performance of C-Band = 0.5 Proton Normal-Conducting Copper and Copper-Silver Radio-Frequency Accelerating Cavities*. Technical report. SLAC National Accelerator Lab., Menlo Park, CA (United States), 2022.

33. S. Corde, E. Adli, J. M. Allen, W. An, C. I. Clarke, B. Clausse, C. E. Clayton, J. P. Delahaye, J. Frederico, S. Gessner, S. Z. Green, M. J. Hogan, C. Joshi, M. Litos, W. Lu, K. A. Marsh, W. B. Mori, N. Vafaei-Najafabadi, D. Walz, and V. Yakimenko. "High-field plasma acceleration in a high-ionization-potential gas". *Nature Communications* 7:1, 2016, pp. 1–6. ISSN: 2041-1723. DOI: 10.1038/ncomms11898. URL: https://www.nature.com/articles/ncomms11898.

34. N. Kumar, A. Pukhov, and K. Lotov. "Self-Modulation Instability of a Long Proton Bunch in Plasmas". *Phys. Rev. Lett.* 104, 25 2010, p. 255003. DOI: 10.1103/PhysRevLett.104.255003. URL: https://link.aps.org/doi/10.1103/PhysRevLett.104.255003.

35. R. O. Dendy. *Plasma dynamics*. Oxford University Press, 1990.

36. E. Huckel and P. Debye. "Zur theorie der elektrolyte. i. gefrierpunktserniedrigung und verwandte erscheinungen". *Phys. Z* 24, 1923, pp. 185–206.

37. L. Tonks and I. Langmuir. "Note on "Oscillations in Ionized Gases"". *Phys. Rev.* 33, 6 1929, pp. 990–990. DOI: 10.1103/PhysRev.33.990. URL: https://link.aps.org/doi/10.1103/PhysRev.33.990.

38. V. I. Veksler. "Coherent principle of acceleration of charged particles", 1956.

39. G. Budker and A. Naumov. "Relativistic stabilized electron beam: II. Brief review of experimental work", 1956.

40. T. Tajima and J. M. Dawson. "Laser Electron Accelerator". *Phys. Rev. Lett.* 43, 4 1979, pp. 267–270. DOI: 10.1103/PhysRevLett.43.267. URL: https://link.aps.org/doi/10.1103/PhysRevLett.43.267.

41. C. Joshi, T. Tajima, J. M. Dawson, H. A. Baldis, and N. A. Ebrahim. "Forward Raman Instability and Electron Acceleration". *Phys. Rev. Lett.* 47, 18 1981, pp. 1285–1288. DOI: 10.1103/PhysRevLett.47.1285. URL: https://link.aps.org/doi/10.1103/PhysRevLett.47.1285.

42. P. Chen, J. M. Dawson, R. W. Huff, and T. Katsouleas. "Acceleration of Electrons by the Interaction of a Bunched Electron Beam with a Plasma". *Phys. Rev. Lett.* 54, 7 1985, pp. 693–696. DOI: 10.1103/PhysRevLett.54.693. URL: https://link.aps.org/doi/10.1103/PhysRevLett.54.693.

43. J. B. Rosenzweig, D. B. Cline, B. Cole, H. Figueroa, W. Gai, R. Konecny, J. Norem, P. Schoessow, and J. Simpson. "Experimental Observation of Plasma Wake-Field Acceleration". *Phys. Rev. Lett.* 61, 1 1988, pp. 98–101. DOI: 10.1103/PhysRevLett.61.98. URL: https://link.aps.org/doi/10.1103/PhysRevLett.61.98.

44. J. M. Dawson. "Nonlinear Electron Oscillations in a Cold Plasma". *Phys. Rev.* 113, 2 1959, pp. 383–387. DOI: 10.1103/PhysRev.113.383. URL: https://link.aps.org/doi/10.1103/PhysRev.113.383.

45. M. J. Hogan. "Electron and Positron Beam–Driven Plasma Acceleration". *Reviews of Accelerator Science and Technology* 09, 2016, pp. 63–83. DOI: 10.1142/S1793626816300036. URL: https://doi.org/10.1142/S1793626816300036.

46. B. Allen, V. Yakimenko, M. Babzien, M. Fedurin, K. Kusche, and P. Muggli. "Experimental Study of Current Filamentation Instability". *Phys. Rev. Lett.* 109, 18 2012, p. 185007. DOI: 10.1103/PhysRevLett.109.185007. URL: https://link.aps.org/doi/10.1103/PhysRevLett.109.185007.

47. K. V. Lotov. "Fine wakefield structure in the blowout regime of plasma wakefield accelerators". *Phys. Rev. ST Accel. Beams* 6, 6 2003, p. 061301. DOI: 10.1103/PhysRevSTAB.6.061301. URL: https://link.aps.org/doi/10.1103/PhysRevSTAB.6.061301.

48. F. Braunmüller, T. Nechaeva, et al. “Proton Bunch Self-Modulation in Plasma with Density Gradient”. *Phys. Rev. Lett.* 125, 26 2020, p. 264801. DOI: 10.1103/PhysRevLett.125.264801. URL: https://link.aps.org/doi/10.1103/PhysRevLett.125.264801.

49. P. I. Morales Guzmán, P. Muggli, R. Agnello, C. C. Ahdida, M. Aladi, M. C. Amoedo Goncalves, Y. Andrebe, O. Apsimon, R. Apsimon, A.-M. Bachmann, M. A. Baistrukov, F. Batsch, M. Bergamaschi, P. Blanchard, F. Braunmüller, P. N. Burrows, B. Buttenschön, A. Caldwell, J. Chappell, E. Chevallay, M. Chung, D. A. Cooke, H. Damerau, C. Davut, G. Demeter, A. Dexter, S. Doebert, J. Farmer, A. Fasoli, V. N. Fedosseev, R. Fiorito, R. A. Fonseca, I. Furno, S. Gessner, A. A. Gorn, E. Granados, M. Granetzny, T. Graubner, O. Grulke, E. Gschwendtner, E. D. Guran, V. Hafych, J. R. Henderson, M. Hüther, M. Á. Kedves, V. Khudyakov, S.-Y. Kim, F. Kraus, M. Krupa, T. Lefevre, L. Liang, N. Lopes, K. V. Lotov, M. Martyanov, S. Mazzoni, D. Medina Godoy, J. T. Moody, K. Moon, M. Moreira, T. Nechaeva, E. Nowak, C. Pakuza, H. Panuganti, A. Pardons, A. Perera, J. Pucek, A. Pukhov, B. Ráczkevi, R. L. Ramjiawan, S. Rey, O. Schmitz, E. Senes, L. O. Silva, C. Stollberg, A. Sublet, A. Topaloudis, N. Torrado, P. V. Tuev, M. Turner, F. Velotti, L. Verra, J. Vieira, H. Vincke, C. P. Welsch, M. Wendt, M. Wing, J. Wolfenden, B. Woolley, G. Xia, M. Zepp, and G. Zevi Della Porta. “Simulation and experimental study of proton bunch self-modulation in plasma with linear density gradients”. *Phys. Rev. Accel. Beams* 24, 10 2021, p. 101301. DOI: 10.1103/PhysRevAccelBeams.24.101301. URL: https://link.aps.org/doi/10.1103/PhysRevAccelBeams.24.101301.

50. A.-M. Bachmann. “Self-Modulation Development of a Proton Bunch in Plasma”. PhD thesis. Technische Universität München, 2021.

51. D. F. Gordon, B. Hafizi, P. Sprangle, R. F. Hubbard, J. R. Peñano, and W. B. Mori. “Seeding of the forward Raman instability by ionization fronts and Raman backscatter”. *Phys. Rev. E* 64, 4 2001, p. 046404. DOI: 10.1103/PhysRevE.64.046404. URL: https://link.aps.org/doi/10.1103/PhysRevE.64.046404.

52. A. Helm, J. Vieira, R. Fonseca, L. Silva, and P. Muggli. “Full-scale modeling of ionization seeding in the AWAKE experiment at CERN”. In: *APS Division of Plasma Physics Meeting Abstracts*. Vol. 2020. 2020, VO03–012.

53. L. Verra, G. Zevi Della Porta, J. Pucek, T. Nechaeva, S. Wyler, M. Bergamaschi, E. Senes, E. Guran, J. T. Moody, M. Á. Kedves, E. Gschwendtner, P. Muggli, R. Agnello, C. C. Ahdida, M. C. A. Goncalves, Y. Andrebe, O. Apsimon, R. Apsimon, J. M. Arnesano, A.-M. Bachmann, D. Barrientos, F. Batsch, V. Bencini, P. Blanchard, P. N. Burrows, B. Buttenschön, A. Caldwell, J. Chappell, E. Chevallay, M. Chung, D. A. Cooke, C. Davut, G. Demeter,

A. C. Dexter, S. Doebert, F. A. Elverson, J. Farmer, A. Fasoli, V. Fedosseev, R. Fonseca, I. Furno, A. Gorn, E. Granados, M. Granetzny, T. Graubner, O. Grulke, V. Hafych, J. Henderson, M. Hüther, V. Khudiakov, S.-Y. Kim, F. Kraus, M. Krupa, T. Lefevre, L. Liang, S. Liu, N. Lopes, K. Lotov, M. Martinez Calderon, S. Mazzoni, D. Medina Godoy, K. Moon, P. I. Morales Guzmán, M. Moreira, E. Nowak, C. Pakuza, H. Panuganti, A. Pardons, K. Pepitone, A. Perera, A. Pukhov, R. L. Ramjiawan, S. Rey, O. Schmitz, F. Silva, L. Silva, C. Stollberg, A. Sublet, C. Swain, A. Topaloudis, N. Torrado, P. Tuev, F. Velotti, V. Verzilov, J. Vieira, M. Weidl, C. Welsch, M. Wendt, M. Wing, J. Wolfenden, B. Woolley, G. Xia, V. Yarygova, and M. Zepp. "Controlled Growth of the Self-Modulation of a Relativistic Proton Bunch in Plasma". *Phys. Rev. Lett.* 129, 2 2022, p. 024802. DOI: 10.1103/PhysRevLett.129.024802. URL: https://link.aps.org/doi/10.1103/PhysRevLett.129.024802.

54. A. Caldwell and K. V. Lotov. "Plasma wakefield acceleration with a modulated proton bunch". *Physics of Plasmas* 18:10, 2011, p. 103101. DOI: 10.1063/1.3641973. URL: https://doi.org/10.1063/1.3641973.

55. S. Romeo, M. Ferrario, and A. R. Rossi. "Beam loading assisted matching scheme for high quality plasma acceleration in linear regime". *Phys. Rev. Accel. Beams* 23, 7 2020, p. 071301. DOI: 10.1103/PhysRevAccelBeams.23.071301. URL: https://link.aps.org/doi/10.1103/PhysRevAccelBeams.23.071301.

56. F. Batsch, P. Muggli, et al. "Transition between Instability and Seeded Self-Modulation of a Relativistic Particle Bunch in Plasma". *Phys. Rev. Lett.* 126, 16 2021, p. 164802. DOI: 10.1103/PhysRevLett.126.164802. URL: https://link.aps.org/doi/10.1103/PhysRevLett.126.164802.

57. E. Adli, A. Ahuja, O. Apsimon, R. Apsimon, A.-M. Bachmann, D. Barrientos, F. Batsch, J. Bauche, V. Berglyd Olsen, M. Bernardini, et al. "Acceleration of electrons in the plasma wakefield of a proton bunch". *Nature* 561:7723, 2018, pp. 363–367.

58. E. Gschwendtner et al. "The AWAKE Run 2 Programme and Beyond". *Symmetry* 14:8, 2022. ISSN: 2073-8994. DOI: 10.3390/sym14081680. URL: https://www.mdpi.com/2073-8994/14/8/1680.

59. E. Lopienska. *CERN Accelerator Complex*. [Online; accessed April 16, 2023]. 2022. URL: https://cds.cern.ch/images/CERN-GRAPHICS-2022-001-1.

60. G. Plyushchev, R. Kersevan, A. Petrenko, and P. Muggli. "A rubidium vapor source for a plasma source for AWAKE". *Journal of Physics D: Applied Physics* 51:2, 2017, p. 025203. DOI: 10.1088/1361-6463/aa9dd7.

61. G. D. Danilatos. "Direct simulation Monte Carlo study of orifice flow". *AIP Conference Proceedings* 585:1, 2001, pp. 924–932. DOI: 10.1063/1.1407658. eprint: https://aip.scitation.org/doi/pdf/10.1063/1.1407658. URL: https://aip.scitation.org/doi/abs/10.1063/1.1407658.

62. A. Boné, N. Lemos, G. Figueira, and J. M. Dias. "Quantitative shadowgraphy for laser–plasma interactions". *Journal of Physics D: Applied Physics* 49:15, 2016, p. 155204. DOI: 10.1088/0022-3727/49/15/155204. URL: https://doi.org/10.1088/0022-3727/49/15/155204.

63. AWAKE Collaboration. "Experimental Observation of Proton Bunch Modulation in a Plasma at Varying Plasma Densities". *Phys. Rev. Lett.* 122, 5 2019, p. 054802. DOI: 10.1103/PhysRevLett.122.054802. URL: https://link.aps.org/doi/10.1103/PhysRevLett.122.054802.

64. E. Öz, F. Batsch, and P. Muggli. "An accurate Rb density measurement method for a plasma wakefield accelerator experiment using a novel Rb reservoir". *Nuclear Instruments and Methods in Physics Research Section A: Accelerators, Spectrometers, Detectors and Associated Equipment* 829, 2016. 2nd European Advanced Accelerator Concepts Workshop - EAAC 2015, pp. 321–325. ISSN: 0168-9002. DOI: https://doi.org/10.1016/j.nima.2016.02.005. URL: https://www.sciencedirect.com/science/article/pii/S0168900216001558.

65. E. Öz and P. Muggli. "A novel Rb vapor plasma source for plasma wakefield accelerators". *Nuclear Instruments and Methods in Physics Research Section A: Accelerators, Spectrometers, Detectors and Associated Equipment* 740, 2014. Proceedings of the first European Advanced Accelerator Concepts Workshop 2013, pp. 197–202. ISSN: 0168-9002. DOI: https://doi.org/10.1016/j.nima.2013.10.093. URL: http://www.sciencedirect.com/science/article/pii/S0168900213015003.

66. V. Fedosseev, P. Muggli, E. Chevallay, A. Masi, J. Hansen, C. Heßler, K. Szczurek, E. Gschwendtner, N. Chritin, M. Martyanov, et al. *Integration of a Terawatt Laser at the CERN SPS Beam for the AWAKE Experiment on Proton-Driven Plasma Wake Acceleration*. Technical report. 2016.

67. P. Muggli et al. "AWAKE readiness for the study of the seeded self-modulation of a 400 GeV proton bunch". *Plasma Physics and Controlled Fusion* 60:1, 2017, p. 014046. DOI: 10.1088/1361-6587/aa941c. URL: https://dx.doi.org/10.1088/1361-6587/aa941c.

68. K. Rieger, A. Caldwell, O. Reimann, R. Tarkeshian, and P. Muggli. "GHz modulation detection using a streak camera: Suitability of streak cameras in the AWAKE experiment". *Review of Scientific Instruments* 88:2, 2017, p. 025110. DOI: 10.1063/1.4975380. URL: https://doi.org/10.1063/1.4975380.

69. P. Muggli and for the AWAKE Collaboration. "Physics to plan AWAKE Run 2". *Journal of Physics: Conference Series* 1596:1, 2020, p. 012008. DOI: 10.1088/1742-6596/1596/1/012008. URL: https://dx.doi.org/10.1088/1742-6596/1596/1/012008.

70. J. M. Ordan. *AWAKE helicon plasma cell R&D lab*. [Online; accessed April 16, 2023]. 2019. URL: https://cds.cern.ch/images/CERN-PHOTO-201910-349-1.

71. N. Torrado et al. *Double pulse generator for unipolar discharges in long plasma tubes for the AWAKE experiment*. 2022. URL: https://indico.lip.pt/event/1245/contributions/4343/contribution.pdf.

72. B. Buttenschön, N. Fahrenkamp, and O. Grulke. "A high power, high density helicon discharge for the plasma wakefield accelerator experiment AWAKE". *Plasma Physics and Controlled Fusion* 60:7, 2018, p. 075005. DOI: 10.1088/1361-6587/aac13a. URL: https://dx.doi.org/10.1088/1361-6587/aac13a.

73. K. V. Lotov and P. V. Tuev. "Plasma wakefield acceleration beyond the dephasing limit with 400 GeV proton driver". *Plasma Physics and Controlled Fusion* 63:12, 2021, p. 125027. DOI: 10.1088/1361-6587/ac349a. URL: https://dx.doi.org/10.1088/1361-6587/ac349a.

74. S. Lund, D. Winklehener, D. Bruhwiler, R. Lehe, and J.-L. Vay. *USPAS 2018: Simulation of Beam and Plasma Systems*. 2018. URL: https://people.nscl.msu.edu/~lund/uspas/sbp_2018/ (visited on 2023).

75. J. P. Boris et al. "Relativistic plasma simulation-optimization of a hybrid code". In: *Proc. Fourth Conf. Num. Sim. Plasmas*. 1970, pp. 3–67.

76. R. A. Fonseca, L. O. Silva, F. S. Tsung, V. K. Decyk, W. Lu, C. Ren, W. B. Mori, S. Deng, S. Lee, T. Katsouleas, and J. C. Adam. "OSIRIS: A Three-Dimensional, Fully Relativistic Particle in Cell Code for Modeling Plasma Based Accelerators". In: *Computational Science — ICCS 2002*. Ed. by P. M. A. Sloot, A. G. Hoekstra, C. J. K. Tan, and J. J. Dongarra. Springer Berlin Heidelberg, Berlin, Heidelberg, 2002, pp. 342–351.

77. R. Courant, K. Friedrichs, and H. Lewy. "ber die partiellen Differenzengleichungen der mathematischen Physik". *Mathematische Annalen* 100:1, 1928, pp. 32–74. ISSN: 1432-1807. DOI: 10.1007/BF01448839. URL: https://link.springer.com/article/10.1007/BF01448839#citeas.

78. S. Diederichs, C. Benedetti, A. Huebl, R. Lehe, A. Myers, A. Sinn, J.-L. Vay, W. Zhang, and M. Thévenet. "HiPACE++: A portable, 3D quasi-static particle-in-cell code". *Computer Physics Communications* 278, 2022, p. 108421. ISSN: 0010-4655. DOI: https://doi.org/10.1016/j.cpc.2022.108421. URL: https://www.sciencedirect.com/science/article/pii/S0010465522001400.

79. P. Sprangle, E. Esarey, and A. Ting. "Nonlinear interaction of intense laser pulses in plasmas". *Phys. Rev. A* 41, 8 1990, pp. 4463–4469. DOI: 10.1103/PhysRevA.41.4463. URL: https://link.aps.org/doi/10.1103/PhysRevA.41.4463.

80. K. Lotov. "AWAKE-related benchmarking tests for simulation codes". *Nuclear Instruments and Methods in Physics Research Section A: Accelerators, Spectrometers, Detectors and Associated Equipment* 909, 2018. 3rd European Advanced Accelerator Concepts workshop (EAAC2017), pp. 446–449. ISSN: 0168-9002. DOI: https://doi.org/10.1016/j.nima.2017.12.051. URL: https://www.sciencedirect.com/science/article/pii/S0168900217314572.

81. A. Caldwell, K. Lotov, A. Pukhov, and G. Xia. "Plasma wakefield excitation with a 24 GeV proton beam". *Plasma Physics and Controlled Fusion* 53:1, 2010, p. 014003. DOI: 10.1088/0741-3335/53/1/014003. URL: https://dx.doi.org/10.1088/0741-3335/53/1/014003.

82. R. Keinigs and M. E. Jones. "Two-dimensional dynamics of the plasma wakefield accelerator". *The Physics of Fluids* 30:1, 1987, pp. 252–263. DOI: 10.1063/1.866183. eprint: https://aip.scitation.org/doi/pdf/10.1063/1.866183. URL: https://aip.scitation.org/doi/abs/10.1063/1.866183.

83. A. A. Gorn and K. V. Lotov. *Trajectory crossing in low density plasmas due to interaction with a long ultrarelativistic beam of charged particles*. 2021. DOI: 10.48550/ARXIV.2108.07530. URL: https://arxiv.org/abs/2108.07530.

84. F. Batsch, M. Martyanov, E. Oez, J. Moody, E. Gschwendtner, A. Caldwell, and P. Muggli. "Interferometer-based high-accuracy white light measurement of neutral rubidium density and gradient at AWAKE". *Nuclear Instruments and Methods in Physics Research Section A: Accelerators, Spectrometers, Detectors and Associated Equipment* 909, 2018. 3rd European Advanced Accelerator Concepts workshop (EAAC2017), pp. 359–363. ISSN: 0168-9002. DOI: https://doi.org/10.1016/j.nima.2018.02.067. URL: http://www.sciencedirect.com/science/article/pii/S0168900218302213.

85. J. M. Dawson. "Nonlinear Electron Oscillations in a Cold Plasma". *Phys. Rev.* 113, 2 1959, pp. 383–387. DOI: 10.1103/PhysRev.113.383. URL: https://link.aps.org/doi/10.1103/PhysRev.113.383.

86. K. V. Lotov and V. A. Minakov. "Proton beam self-modulation seeded by electron bunch in plasma with density ramp". *Plasma Physics and Controlled Fusion* 62:11, 2020, p. 115025. DOI: 10.1088/1361-6587/abba42. URL: https://dx.doi.org/10.1088/1361-6587/abba42.

87. A. Gorn, M. Turner, et al. "Proton beam defocusing in AWAKE: comparison of simulations and measurements". *Plasma Physics and Controlled Fusion* 62:12, 2020, p. 125023.

88. E. Gschwendtner, E. Adli, L. Amorim, R. Apsimon, R. Assmann, A.-M. Bachmann, F. Batsch, J. Bauche, V. B. Olsen, M. Bernardini, et al. "AWAKE, the advanced proton driven plasma wakefield acceleration experiment at CERN". *Nuclear Instruments and Methods in Physics Research Section A: Accelerators, Spectrometers, Detectors and Associated Equipment* 829, 2016, pp. 76–82.

89. F. Batsch. "Setup and Characteristics of a Timing Reference Signal with sub-ps Accuracy for AWAKE". *Journal of Physics: Conference Series* 1596, 2020, p. 012006. DOI: 10.1088/1742-6596/1596/1/012006. URL: https://doi.org/10.1088/1742-6596/1596/1/012006.

90. C. B. Schroeder, C. Benedetti, E. Esarey, F. J. Grüner, and W. P. Leemans. "Coupled beam hose and self-modulation instabilities in overdense plasma". *Phys. Rev. E* 86, 2 2012, p. 026402. DOI: 10.1103/PhysRevE.86.026402. URL: https://link.aps.org/doi/10.1103/PhysRevE.86.026402.

91. P. Morales Guzmán and P. Muggli. "PIC Simulations of the Seeded Self-Modulation of a Long Proton Bunch in Plasma Density Gradients". *EPS Plasma 2021*.

92. J. Chappell et al. "Experimental study of extended timescale dynamics of a plasma wakefield driven by a self-modulated proton bunch". *Phys. Rev. Accel. Beams* 24, 1 2021, p. 011301. DOI: 10.1103/PhysRevAccelBeams.24.011301. URL: https://link.aps.org/doi/10.1103/PhysRevAccelBeams.24.011301.

93. P. I. Morales Guzmán and P. Muggli. "PIC Simulations of the Interaction between Self-Modulation in the Front and Rear of a relativistic Proton Bunch in Plasma". *EPS Plasma 2022*.

94. J. Pucek. "Working Thesis Title". PhD thesis. TUM, 2023. unpublished thesis.

95. J. B. Rosenzweig, B. Breizman, T. Katsouleas, and J. J. Su. "Acceleration and focusing of electrons in two-dimensional nonlinear plasma wake fields". *Phys. Rev. A* 44, 10 1991, R6189–R6192. DOI: 10.1103/PhysRevA.44.R6189. URL: https://link.aps.org/doi/10.1103/PhysRevA.44.R6189.

96. P. Chen, K. Oide, A. M. Sessler, and S. S. Yu. "Plasma-based adiabatic focuser". *Phys. Rev. Lett.* 64, 11 1990, pp. 1231–1234. DOI: 10.1103/PhysRevLett.64.1231. URL: https://link.aps.org/doi/10.1103/PhysRevLett.64.1231.

97. M. J. Hogan, C. E. Clayton, C. Huang, P. Muggli, S. Wang, B. E. Blue, D. Walz, K. A. Marsh, C. L. O'Connell, S. Lee, R. Iverson, F.-J. Decker, P. Raimondi, W. B. Mori, T. C. Katsouleas, C. Joshi, and R. H. Siemann. "Ultrarelativistic-Positron-Beam Transport through Meter-Scale Plasmas". *Phys. Rev. Lett.* 90, 20 2003, p. 205002. DOI: 10.1103/PhysRevLett.90.205002. URL: https://link.aps.org/doi/10.1103/PhysRevLett.90.205002.

98. A. A. Gorn, P. V. Tuev, A. V. Petrenko, A. P. Sosedkin, and K. V. Lotov. "Response of narrow cylindrical plasmas to dense charged particle beams". *Physics of Plasmas* 25:6, 2018, p. 063108. DOI: 10.1063/1.5039803. eprint: https://doi.org/10.1063/1.5039803. URL: https://doi.org/10.1063/1.5039803.

99. S. Corde, E. Adli, J. Allen, W. An, C. Clarke, C. Clayton, J. Delahaye, J. Frederico, S. Gessner, S. Green, et al. "Multi-gigaelectronvolt acceleration of positrons in a self-loaded plasma wakefield". *Nature* 524:7566, 2015, pp. 442–445.

100. R. Ariniello, C. E. Doss, K. Hunt-Stone, J. R. Cary, and M. D. Litos. "Transverse beam dynamics in a plasma density ramp". *Phys. Rev. Accel. Beams* 22, 4 2019, p. 041304. DOI: 10.1103/PhysRevAccelBeams.22.041304. URL: https://link.aps.org/doi/10.1103/PhysRevAccelBeams.22.041304.

101. K. Floettmann. "Adiabatic matching section for plasma accelerated beams". *Phys. Rev. ST Accel. Beams* 17, 5 2014, p. 054402. DOI: 10.1103/PhysRevSTAB.17.054402. URL: https://link.aps.org/doi/10.1103/PhysRevSTAB.17.054402.

102. X. L. Xu, J. F. Hua, Y. P. Wu, C. J. Zhang, F. Li, Y. Wan, C.-H. Pai, W. Lu, W. An, P. Yu, M. J. Hogan, C. Joshi, and W. B. Mori. "Physics of Phase Space Matching for Staging Plasma and Traditional Accelerator Components Using Longitudinally Tailored Plasma Profiles". *Phys. Rev. Lett.* 116, 12 2016, p. 124801. DOI: 10.1103/PhysRevLett.116.124801. URL: https://link.aps.org/doi/10.1103/PhysRevLett.116.124801.

103. A. Caldwell, E. Gschwendtner, K. Lotov, P. Muggli, and M. Wing. *AWAKE design report: a proton-driven plasma wakefield acceleration experiment at CERN*. Technical report. 2013.

104. M. Vladimir. private communication. 2022.

105. P. Muggli, P. I. M. Guzman, A.-M. Bachmann, M. Hüther, M. Moreira, M. Turner, and J. Vieira. "Seeding self-modulation of a long proton bunch with a short electron bunch". *Journal of Physics: Conference Series* 1596:1, 2020, p. 012066. DOI: 10.1088/1742-6596/1596/1/012066. URL: https://dx.doi.org/10.1088/1742-6596/1596/1/012066.

106. P. Muggli. private communication. 2023.

107. R. Ramjiawan, V. Bencini, P. Burrows, and F. Velotti. "Design of the proton and electron transfer lines for AWAKE Run 2c". *Nuclear Instruments and Methods in Physics Research Section A: Accelerators, Spectrometers, Detectors and Associated Equipment* 1049, 2023, p. 168094. ISSN: 0168-9002. DOI: https://doi.org/10.1016/j.nima.2023.168094. URL: https://www.sciencedirect.com/science/article/pii/S0168900223000840.

108. J. P. Farmer, L. Liang, R. Ramjiawan, F. M. Velotti, M. Weidl, E. Gschwendtner, and P. Muggli. "Injection tolerances and self-matching in a quasilinear wakefield accelerator". *arXiv preprint arXiv:2203.11622*, 2022.